NAGOYA INSTITUTE OF TECHNOLOGY

Growth of Transition Metal Dichalcogenides Layers by Chemical Vapor Deposition (CVD) and Investigation of their Photoresponse Properties

化学気相合成(CVD)法による遷移金属ダイカルコゲナイド層の成長とその光応答特性の評価

by

Rakesh D. Mahyavanshi

A thesis submitted to the Department of Physical Science and Engineering of
Nagoya Institute of Technology
in partial fulfillment of the Requirements for the Degree of
Doctor of Philosophy (Ph.D.)

March 2019

Declaration of Authorship

I, Rakesh D. Mahyavanshi, declare that this thesis titled, ’Growth of Transition Metal Dichalcogenides Layers by Chemical Vapor Deposition (CVD) and Investigation of their Photoresponse Properties’ and the work presented in it is my own.

I confirm that:

- This work was done wholly or mainly while in candidature for a research degree at this University.
- Where any part of this thesis has previously been submitted for a degree or any other qualifications at this University or any other institution, this has been clearly stated.
- Where I have consulted the published work of others, this is always clearly attributed.
- Where I have quoted from the work of others, the source is always given. With the exception of such quotations, this thesis is entirely my own work.
- I have acknowledged all main sources of help.
- Where the thesis is based on work done by myself jointly with others, I have made clear exactly what was done by others and what I have contributed myself.

Signed:

Date:

ACKNOWLEDGEMENT

My deep gratitude goes first to my supervisor **Associate Professor Golap Kalita** for accepting me as his student. I highly appreciate the opportunity provided to study under his valuable guidance. He offered me so much advice, patiently supervising me, and always guiding me in the right direction. I've learned a lot from him, without his guidance, I could not have completed my dissertation. It was an honor to be his student. I will always be indebted to him.

I would also like to express my sincere appreciation to **Professor Masaki Tanemura** for insightful comments and encouragement. Thank you so much for guiding me in all the time of research and writing this thesis. I also appreciate the advice of the committee members and **Professor Shingo Ono**, for his critical comments, which enabled me to notice the weaknesses of my dissertation and thereby make the necessary improvements according to their comments.

I would also like to express my sincere gratitude to **Professor Toshio Kawahara** for insightful comments which helped me improve the thesis significantly.

I acknowledge my indebtedness to **NGK** for providing me with the scholarship during my Ph. D. research. Without this support, it would not have possible for me to complete this research.

I am so thankful to my senior **Dr. Sachin Shinde** who introduced me to this laboratory, for cheering me up to do research and providing valuable guidance throughout my Ph.D., without whom I would not be at this point. Also, I would like to thank **Mr. Pradeep Desai**, **Dr. Amutha Thangaraja, Dr. Remi Papon** and **Dr. Riteshkumar Vishwakarma** for their support and guidance during my research and writing of my thesis. I am especially, thankful to all masters and bachelor students of my lab for their help naming some **Mr. Ogura, Mr. Zuck, Mr. Ajinkya** they were always present whenever I needed them to help me.
I want to thank my dear sister **Mrs. Mohini Kamble** and my brother in-law **Mr. Bindu Kamble**. Thank you so much for providing support throughout my life and making me who I am today. I owe this success to you and will always be indebted to both of you.I would like to thank my family **Aai, Pappa, Raja Bhai, Taraben, Chandrakant Jiju, Rupali, and Abhay** for supporting throughout my career.

Abstract

The transition metal dichalcogenides (TMDCs) layered materials have attracted significant interest for application in nanoelectronics and optoelectronics. Bulk TMDCs are normally indirect bandgap, whereas, monolayer TMDCs are direct bandgap semiconductors, which has lot of significance for device application. In this thesis, synthesis of monolayer TMDCs such as molybdenum disulfide and tungsten disulfide by chemical vapor deposition (CVD), their environmental stability and fabrication of heterojunction optoelectronic devices were investigated.

Chapter 1 describes the background of TMDCs materials and their unique properties. Then different synthesis methods of TMDCs layer, the characterizations of synthesized materials, identifying the layered structure, stability issues and current trend of device applications are discussed. The challenges in synthesis of monolayer TMDCs and their device fabrication process are addressed, in the motivation and objective part.

Chapter 2 deals with synthesis of TMDCs layer using a developed atmospheric pressure CVD (APCVD) technique particularly for this research work. The growth of ribbons, triangular crystals and continuous film of MoS_2 and WS_2 layers was achieved by the CVD method with specific parameters. The MoS_2 ribbon structure with high edge density can be significant for catalytic applications. However, ribbon shows poor photoluminescence (PL) than that of triangular crystals, hence further studies were performed for only triangular crystals and films. During the growth of the MoS_2 and WS_2 layers by the CVD method, some degradation was observed due to environmental exposure as explained in the next chapter.

Chapter 3 analyzes the detailed degradation process of MoS_2 and WS_2 layers and subsequent encapsulation, which is an important aspect for practical device application of the TMDCs layers. Detailed analysis of degraded area showed that the degradation patterns appear due to oxidation and significant loss of sulfur from defective sites and edges. To prevent the dilapidation, dry encapsulation of TMDCs layer at room temperature with hydrophobic Teflon and carbonaceous layer was explored. The encapsulated dichalcogenide samples remained intact after heating at 200°C with stable photoconductivity. As in the encapsulation studies showed a foreign material can be

directly deposited to reduce environmental degradation, heterostructure devices were designed by depositing a foreign semiconductor on top of the MoS_2 layer.

Chapter 4 discusses the possibility of fabricating of unique Ge/MoS_2 heterostructure device as both materials possess layered structures. Ge with a low bandgap (0.66 eV) than that of Si (1.1 eV) has been widely used for infrared (IR) photodiode. The Ge film was directly deposited by low pressure thermal evaporation on CVD synthesized MoS_2 layer. A thin interface was formed in-between the thermally evaporated Ge and chemical vapor deposited MoS_2 layers, considering the atomically smooth surface of MoS_2. It is realized that the demonstrated ultrathin heterojunction of Ge and MoS_2 layers can be significant for developing self-powered broadband photodetectors beyond Si device wavelength.

Chapter 5 focuses on fabrication of a wide bandgap semiconductor and MoS_2 layer heterojunction. In this case, copper iodide (CuI) was chosen considering the p-type conductivity, where the counterpart MoS_2 layer is n-type. The CuI layer was deposited by two different methods, solid phase iodization and direct thermal evaporation. Significant quenching of PL peak for the MoS_2 layer in CuI/MoS_2 heterostructure was observed attributing a spontaneous charge separation. A CuI/MoS_2 heterojunction device was fabricated on sapphire substrate, which showed promising photoresponsivity with light illumination. This suggests that a p-type halide can be very effective on MoS_2 layer for developing heterojunction device.

Chapter 6 summarizes the whole thesis and future prospects.

Table of Contents

List of Figures viii
List of Tables xiv
1. Introduction 1
  1.1 Background on Layered Transition Metal dichalcogenides 1
  1.2 Structure 2
  1.3 Electronic band structure and optical properties 3
  1.4 Catalytic Properties 5
  1.5 Synthesis of MoS_2 and WS_2 5
  1.6 Characterization 7
    1.6.1 Optical Microscopy 7
    1.6.2 Field emission scanning electron microscopy (FE-SEM) 8
    1.6.3 Raman spectroscopy 9
    1.6.4 Atomic force microscopy (AFM) 10
    1.6.5 Photoluminescence spectroscopy (PL) 11
    1.6.6 X-ray photoelectron spectroscopy (XPS) 12
  1.7 Atmospheric Stability 13
  1.8 Encapsulation of TMDCs 14
  1.9 Applications of WS_2 and MoS_2 14
  1.10 Motivation and objectives of current work 16
  1.11 Organization of the dissertation 17
  1.12 References 18
2. Synthesis of MoS_2 Crystals and Continuous film by CVD in sulfur enriched environment 24
  2.1 Introduction 24
  2.2 Experimental details 25
  2.3 Results and discussion 26
    2.3.1 Optical microscopy 27
    2.3.2 Raman spectroscopy 28
    2.3.3 Field-emission scanning electron microscopy (FE-SEM) 29
    2.3.4 Atomic force microscopy (AFM) 32

2.3.5 Photoluminescence (PL) spectroscopy 33
2.3.6 X-ray photoelectron spectroscopy (XPS) 34
2.4 Conclusions 35
2.5 References 35
3. Degradation and Encapsulation Study of 2D-TMDCs 40
3.1 Atmospheric degradation in WS_2 crystals 40
3.1.1 Introduction 40
3.1.2 Materials and method 41
3.1.3 Results and Discussion 42
3.2 Encapsulation of TMDCs 50
3.2.1 Hydrophobic Teflon coating by low pressure thermal deposition 51
3.2.2 Encapsulation of TMDC crystals with room temperature plasma deposited carbonaceous film 53
3.3 Conclusion 64
3.4 References 65
4. Photovoltaic action with broadband photoresponsivity in germanium-MoS_2 ultrathin heterojunction 67
4.1 Introduction 67
4.2 Experimental 68
4.3 Characterization 69
4.4 Results and Discussion 69
4.5 Conclusion 79
4.6 References 80
5. Observing charge transfer interaction in CuI and MoS_2 heterojunction for photoresponsive device application 84
5.1 Introduction 84
5.2 Experimental details 85
5.2.1 CVD Synthesis of MoS_2 layer 85
5.2.2 CuI deposition on MoS_2 layers 86
5.2.3 Device fabrication process 87
5.2.4 Characterization of materials and devices 88

5.3 Results and discussion 88
5.3.1 SEM 88
5.3.2 AFM 89
5.3.3 Raman spectroscopy 89
5.3.4 UV-Vis absorption spectroscopy 90
5.3.5 XRD 91
5.3.6 XPS 92
5.3.7 PL spectroscopy 93
5.3.8 Fabrication and characterization of photoresponsive device 94
5.4 Conclusions 96
5.5 References 97
6. Conclusions and future prospects 99
6.1 Conclusions 99
6.2 Future prospects 100
6.3 List of research achievements 102

LIST OF FIGURES

Figure 1-1 Atomic arrangement in 2H phase and 1T phase layered TMDCs 2
Figure 1-2 Top and cross-sectional view of layered TMDCs in 2H and top view of 1T phase 3
Figure 1-3 Electronic band gap structure of bulk and monolayer MoS_2 (Reprinted with permission from Wang *et al*., 2012) 4
Figure 1-4 Electronic band gap structure of bulk and monolayer WS_2 (Reprinted with permission from Wang *et al*., Nature Nanotechnology, 2012) 4
Figure 1-5 Optical images of CVD synthesized (a) MoS_2 layer formed by merging of crystals (b)MoS_2 crystals (c) WS_2 crystals and (d) MoS_2 ribbons. 8
Figure 1-6 SEM images of WS_2 crystals in (a) triangular (b) Dendritic and (c) Hexagonal shape MoS_2 layer (d) and crystals (e). 9
Figure 1-7 Raman Spectra for 2D (a) MoS_2 and (b) WS_2 10

Figure 1-8 AFM images of monolayer (a) WS_2 and (b) MoS_2 crystals synthesized by APCVD.. 11

Figure 1-9 PL spectra for monolayer (a) MoS_2 and (b) WS_2 12

Figure 1-10 XPS spectra for (a) MoS_2-Mo 3d transition (b) MoS_2-S 2p transition (c) WS_2-W 4f transition and (d) WS_2-S 2p transition.. 13

Figure 2-1(a) Schematic diagram of the CVD process for synthesis of MoS_2 ribbons and their branched structures (b) Growth scheme of MoS_2 ribbon and other crystals on SiO_2/Si substrate. Substrate was placed in face down manner to the center of the boat leaving small gap between head and tail of boat for passage of gas with sulfur vapor. 26

Figure 2-2 Optical microscopic images of (a) MoS_2 ribbon structures on SiO_2/Si substrate. (b) Presenting the various branching structures of the ribbon (blue ribbon structures). (c) Multi-branching pattern of the MoS_2 ribbons. (d) and (e) Bidirectional ribbon structure forming V-shape with an angle of 120° and 60°. (f) Formation of equilateral triangles at different position of the substrate. 28

Figure 2-3 (a) Raman vibration modes E^1_{2g} (383.2 cm^{-1}) and A_{1g} (404.7 cm^{-1}). (b) Raman mapping image for the A_{1g} peak.. 28

Figure 2-4 FE-SEM images of (a) of the synthesized MoS_2 ribbons presenting the individual and various branched structures. (b) Tri-directional MoS_2 ribbon with Y-shape. (c) Higher resolution image at the center of the Y-shape ribbon structure, where the growth of the three arm with 120°. (d) MoS_2 crystals and (e) their merged structure to form large-area film at center zone of substrate. (f) Continuous growth and merging of the crystals to millimeter scale. 30

Figure 2-5 FE-SEM images of (a) bidirectional MoS_2 ribbon presenting uneven edge structure, (b) and (c) edge structures of the MoS_2 ribbon creating 60° and 120° angles. (d) Schematic view of the possible edge termination with molybdenum (M) or sulfur (S) atoms to form 60° and 120° edges... 31

Figure 2-6(a) AFM image of the as-synthesized MoS_2 ribbon on SiO_2/Si substrate marked by red arrow.. 32

Figure 2-7(a) PL spectra and (b) mapping image for an equilateral triangular shaped MoS_2 crystal obtained along with the ribbons as discussed in OM and SEM image. (c) PL spectra and (d) mapping image of the MoS_2 ribbon.. 33

Figure 2-8 (a) Deconvoluted XPS core-level spectra of Mo 4f peak, confirming the chemical state doublet Mo $4f_{7/2}$ (230.1 eV) and Mo $4f_{5/2}$ (233.3 eV) peaks. (b) Deconvoluted XPS S $2p_{3/2}$ (~162.4 eV) and S$2p_{1/2}$ (~163.5 eV) peaks. 34

Figure 3-1 Schematic of the seed-assisted growth process for triangular, hexagonal and other shaped WS_2 crystals. 41

Figure 3-2 FE-SEM images of as-synthesized (a) equilateral triangular, (b) truncated triangular and (c) hexagonal shaped WS_2 crystal. Structural transformation feature of (d) truncated WS_2 crystal, (e) hexagonal shaped WS_2 crystal and (f) high resolution image of degradation pattern inside the hexagonal crystal. 43

Figure 3-3 FE-SEM images of (a) oppositely orientated two triangular WS_2 crystals immediately after synthesis and (b) after exposing to ambient conditions for 12 months, formation of small equilateral triangles in the triangular crystals is observed as presented in the inset of the figure (c) high resolution image of oppositely orientated equilateral triangles formation inside the triangular WS_2 crystal. (d) Schematic of the tungsten (W) and sulfur (S) terminated WS_2 triangular crystals with possible edge termination of the oppositely orientated small triangles in the individual crystal 44

Figure 3-4 XPS spectra of (a) W 4f peak for fresh and long duration exposure in atmospheric conditions WS_2 samples. (b) De-convoluted W 4f peak for WS_2 crystals with long duration exposure in atmospheric conditions. (c) SEM image of a triangular WS_2 crystal, where selective AES analysis is performed. (d) AES spectra at three different position (1, 2 and 3) presenting the peaks for sulfur, tungsten, carbon and oxygen. Individual (e) oxygen and (f) sulfur peaks analysis at position 1, 2 and 3. 46

Figure 3-5(a) Optical microscopy image of a triangular WS_2 crystal immediately after synthesis. (b) PL mapping and (c) intensity profile analysis of the WS_2 crystal. (d) Optical microscope image of a highly degraded triangle after 15 months of exposure to atmosphere. (e) PL mapping and (f) intensity profile of the degraded WS_2 crystal....... 47

Figure 3-6 FE-SEM images of (a) individual and (b) interconnected triangular WS_2 crystals after 15 months of atmospheric exposure with enlarged triangular degraded areas. (c) Deconvoluted Raman spectra at non-degraded area (position 1) and (d) inside degraded triangle of the same WS_2 crystal (position 2). (e) AFM image of the triangular crystal presenting the degraded edges and formation of degraded triangle inside. (f) Line profile at degraded edge (position 1) and center (position 2) presenting the thickness difference within the WS_2 crystal. 49

Figure 3-7 (a) Schematic of hydrophobic Teflon (fluorocarbon) as encapsulating layer on the WS_2 monolayer to prevent atmospheric degradation. (b) Optical microscope images of Teflon coated WS_2 crystal on the SiO_2/Si substrate. (c) PL spectra for fresh WS_2 crystal before and after accelerated heating test. (d) PL spectra for Teflon coated WS_2 crystal before and after accelerated heating test.. 52

Figure 3-8 transparency of the Teflon thin film deposited on glass substrate along the coating of WS_2/SiO_2/Si sample. 53

Figure 3-9(a) optical microscope images of as-synthesized MoS_2 crystal on the SiO_2/Si substrate. (b) AFM image of MoS_2 crystal and line profile presenting the thickness. Optical microscope images of carbonaceous coated (c) MoS_2 crystals and (d) higher resolution view of a triangular MoS_2 crystal. 54

Figure 3-10 (a) IR (b) Raman (c) Transmittance and absorbance spectra of the carbonaceous film on SiO_2/Si and glass substrates, deposited along with the coating of TMDCs crystals samples. Raman spectra of the (d) MoS_2 crystal on SiO_2/Si substrate (e) A_{1g} and E_{2g} peaks with and without encapsulation film. 55

Figure 3-11 FE-SEM image of (a) as-synthesized and (b) carbonaceous film coated MoS_2 crystal. (c) Photoluminescence (PL) spectra of the uncoated and coated MoS_2 crystal. (d) Schematic of induced compressive strain on the MoS_2 crystal in presence of Encapsulation film. 57

Figure 3-12 Opitcal miscroscope image of (a) CVD synthsized triangular WS_2 crystals on SiO_2/Si substrate, (b) and (c) MW-SWP deposited carbonaceous film on the CVD synthesized WS_2 crystals with different thickness. (d) Raman spectra of the WS_2 crystal before and after encapsulation. 58

Figure 3-13 Deconvoluted XPS core-level spectra of (a) Mo3d, (b) S2p, (c) C1s for the encapsulated MoS_2 sample and (d)W4f, (e) S2p, (f) C1s for the encapsulated WS_2 sample. 59

Figure 3-14 FE-SEM images of triangular WS_2 crystals (a) with and (b) without coating a carbonaceous film after heating in atmosphere at 200 °C for 1 hours. PL spectra for (c) before and (d) after heating of the WS_2 crystals with different thickness of encapsulation layers in comparison with uncoated sample. (d) Optical microscope images of the (e) encapsulated WS_2 sample after heating in atmosphere at 250 °C and (f) cracks formation in a WS_2 crystals after the heating. 61

Figure 3-15 (a) Schematic diagram and (b) optical microscope image of Au/MoS_2/Au device with encapsulating carbonaceous layer. Current-voltage (*J*-*V*) characteristics of (c) as-fabricated and (d) after annealing at 200°C for 1hr. Au/MoS_2/Au device under dark and light illumination. 63

Figure 4-1**:** Optical microscope images of (a) triangular MoS_2 crystals, (b) continuous layer and (c) Optical microscope image of continuous Ge-MoS_2 heterostructure 70

Figure 4-2 (a) SEM images of as-synthesized uniform MoS_2 layer and (b) SEM image of the Ge-MoS_2 interface on SiO_2/Si substrate 70

Figure 4-3 (a) AFM image for the MoS_2 layer, (b) Line profile showing a thickness of MoS_2 layer on SiO_2/Si substrate, (c) AFM image of Ge-MoS_2 interface and (d) Line profile showing a thickness of Ge film as 10.3 nm 71

Figure 4-4 (a) Raman spectra with characteristic in-plane Mo-S vibrational mode E^1_{2g} (383.5 cm^{-1}) and out of plan vibration mode A_{1g} (404.5) of S atoms and (b) PL spectra with the peak position at 684 nm, corresponding to 1.81 eV 72

Figure 4-5 XPS (a) Survey spectra (b) Mo3d ($3d_{5/2}$ ~230 eV and $3d_{3/2}$ ~233 eV) (c) S2p ($2p_{3/2}$~162 eV $2p_{1/2}$~164 eV) for as-synthesized MoS_2 and Ge-MoS_2 heterostructure (d) Ge3d peak for Ge-MoS_2 heterostructure (Ge peak-center ~30 eV). 73

Figure 4-6 (a) Raman Spectra for Ge-MoS_2 heterostructure with peaks for Ge, MoS_2, and SiO_2/Si respectively (b) Normalized Raman spectra for Ge film with and without MoS_2 layer (c) Raman spectra of as-synthesized and Ge deposited MoS_2 layer...................... 74

Figure 4-7 (a) Schematics of the fabricated Ge-MoS_2 heterostructure device (b) *J*-*V* characteristics without light illumination (inset shows log plot of *J*-*V*) (c) *J*-*V* characteristics without (blue) and with (red) light illumination showing a photovoltaic action (d) QE spectra for the heterostructure device. Energy band-diagram (e) with work function of active and electrode layers (f) equilibrium for the Ge-MoS_2 heterojunction. 75

Figure 4-8 Transient photoresponse at (a) 0 bias voltage and (b) at -0.5 and -1 bias voltage under illumination of 360 nm light. (c) Transient photoresponse at 0 bias voltage and (d) at -0.5 and -1 bias voltage under illumination of 550 nm light. (e) Transient photoresponse at 0 bias voltage and (f) at -0.5 and -1 bias voltage under illumination of 1000 nm light. 78

Figure 5-1 Solid phase reaction chamber for Cu film with I vapor on MoS_2 layer ($Cu/MoS_2/SiO_2/Si$). Vapor from I beads in the sealed box react with metallic Cu film at room temperature and pressure to form CuI. 87

Figure 5-2(a) SEM image of triangular MoS_2 crystals, merging to form a continuous film.(b) SEM image at the intersection of MoS_2 layer and CuI film.(c)SEM image of the thermally evaporated CuI film on MoS_2. 88

Figure 5-3 AFM image and thickness profile for the synthesized MoS_2 layers on SiO_2/Si substrate. 89

Figure 5-4(a) Raman spectra with frequencies for layered MoS_2 layers at 385.6 cm^{-1} for E_{2g} and 406.6 cm^{-1} for A_{1g} respectively (b) Raman spectra of the MoS_2 layers before and after the deposition of CuI film. 90

Figure 5-5 (a) UV-Vis absorption spectra for CuI on the glass substrate. (b) Touc plot confirming an optical band gap of 3.0 eV (c) UV-Vis absorption spectra for CuI on the glass substrate. (d) Tauc plot confirming an optical band gap of 2.98eV. 91

Figure 5-6 XPS spectra for (a) Cu($2p^{3/2}$~932.2 eV and $2p^{1/2}$~952 eV)(b) I($3d^{5/2}$~619.5 eV and 631 eV for $3d^{3/2}$) of the CuI film obtained by solid phase iodization process on glass and MoS_2 layers. XPS spectra for (c) Mo (Mo $3d^{5/2}$~229.6 eV and $3d^{3/2}$~323.7 eV) and (d) S ($2p^{3/2}$~162.4 eV and $2p^{1/2}$~163.7 eV) of the MoS_2 layer. 92

Figure 5-7 (a) X-Ray Diffraction (XRD) spectra of CuI film. (b) XRD diffraction pattern of thermally evaporated CuI film on glass substrate. 92

Figure 5-8 PL spectra of MoS_2 layers after the deposition of the CuI layer by the two different approaches (a) the solid phase iodization and (b) thermal evaporation. (c) PL peak for as synthesized MoS_2 layer. 93

Figure 5-9 (a) schematic diagram for fabricated heterojunction device with a device structure of Au/γ-CuI/MoS_2/Al.(b) *J-V* characteristics under dark condition, (c) *J-V* characteristics under dark and white light illumination, presenting significant photoresponsivity. (d) Probable energy band diagram for the γ-CuI/MoS_2 heterojunction photovoltaic device. (e) Cross-section stick-and-ball crystal structures of cubic γ-CuI along (111) plane on MoS_2 layers, γ-CuI (111) enables formation of effective heterojunction interface for exciton dissociation and separation. 95

LIST OF TABLES

Table 4-1**:** Photoresponse values of the Ge-MoS_2 heterojunction device at different applied voltage for UV, visible and near-IR lights.. 79
Table 5-1 Experimental parameters of MoS_2 layers synthesis on the target substrates.. 86
Table 5-2 Experimental parameters of Cu and CuI deposition on MoS_2 layers............. 87

CHAPTER 1

1. Introduction

1.1 Background on Layered Transition Metal dichalcogenides

Transition Metal Dichalcogenides (TMDCs) are classes of materials with Transition metals such as Tungsten (W) and Molybdenum (Mo) atoms in honeycomb structure with Chalcogen (S, Se or Te) atoms in MX_2 type. In this configuration, metal atom is covalently bonded with two Chalcogen atoms and the layers are held together by Van der Waals force. This class includes semiconductors such as MoS_2 (Molybdenum disulfide) and WS_2 (Tungsten disulfide), semimetals e.g. WTe_2, $TiSe_2$, metals such as TiS_2, VSe_2, superconductors (e.g. TaS_2, $NbSe_2$) as well as insulators (e.g. HfS_2) [1]–[11]. These materials show exceptional optical and catalytic properties with semiconducting nature. This has been demonstrated in first two dimensional (2D) TMDCs, transistor [9] as well as strong photoluminescence (PL) [12], [13]. The emergence of graphene as strongest, lightest, thinnest material with best heat and electrical conductivity opened Pandora’s Box in 2D materials related research. Although, much attention has been given to graphene since 2004 and subsequent Physics Nobel Prize in 2010 to Sir Andre Geim and Sir Kostya Novoselov, it has its limitations due to zero bandgap [14], [15]. In this line, to find the alternative to the limitations of graphene, focus has also been shifted to other 2D materials with semiconducting properties. The strong photoluminescence, semiconducting nature, and catalytic activity has made 2D-TMDCs attractive candidates for applications in electronic, optoelectronic, sensing and catalysis [16]–[21].

Since the first structural determination by Linus Pauling in 1923, subsequent discovery of more than 40 layered structures of TMDCs has been reported by late 1960s. Robert Frindt reported first adhesive tape method for MoS_2 thin layer synthesis in 1963 and subsequently in 1986 monolayer MoS_2 suspension was reported. Early part of 1990 saw significant development in carbon nanotubes and inorganic fullerenes followed by WS_2

and MoS_2 nanotubes and nested particles. Finally, after discovery of stable monolayer graphene and related research paved the way for significant development in ultrathin film and monolayer TMDCs applications.

1.2 Structure

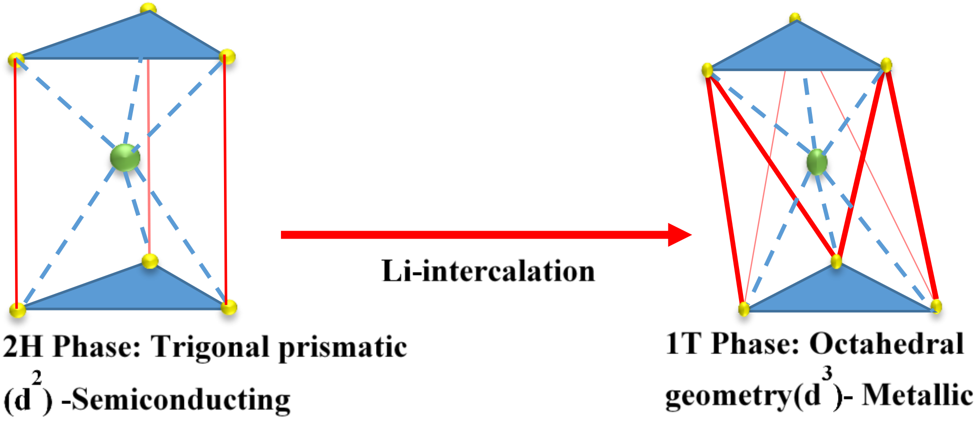

Figure 1-1 Atomic arrangement in 2H phase and 1T phase layered TMDCs

Layered TMDCs are metal and chalcogen atoms arranged in various coordination phases with different structural arrangements. Most common structural phases are trigonal prismatic and octahedral. The Trigonal prismatic i.e. 2H phase is most stable form of coordination sphere around the metal atom which has ABA stacking of atoms where chalcogen atoms occupy same position in different planes. The octahedral (1T) phase can be obtained by lithium intercalation of 2H phase (Figure 1-1). The resulting 1T metastable phase shows metallic characteristics which is unstable from than that of semiconducting 2H phase. Stacking order in octahedral phase show ABC stacking of corresponding atoms. The thermodynamic stability of these structures mainly depends on the combination of transition metals i.e. (group IV, V, VI, VII, IX or X) and chalcogen atoms (S, Se or Te). Also, honeycomb arrangements of the atoms give different edge structures depending on atomic arrangements in case of chemical vapor deposition (CVD) synthesized TMDCs. The variation in edge termination depends on supply of precursors with stoichiometric availability of metal or the chalcogen atoms. The concentration gradient along the surface of the substrate as well as the distance between two precursors also has significant effect on synthesized crystals [22]. Two major edge terminations being chalcogen termination and metal termination. The study of edge structure of these materials is significant for the applications in catalysis and electrochemistry.

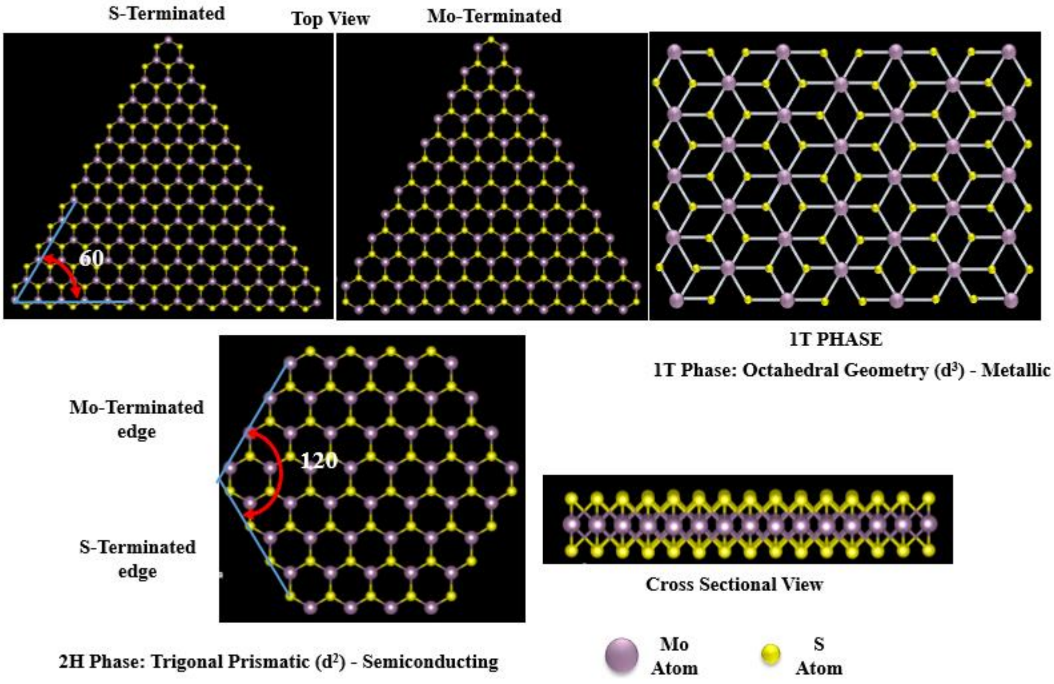

Figure 1-2 Top and cross-sectional view of layered TMDCs in 2H and top view of 1T phase

1.3 Electronic band structure and optical properties

The Transition from bulk to monolayer for the TMDCs show interesting change in bandgap from indirect to direct bandgap respectively. Here we have focused mainly on group VI transition metals Mo and W in combination with sulfur atoms i.e. WS_2 and MoS_2. These structure shows semiconducting 2H stable phase which has been utilized for the fabrication of single layer field effect transistor (FET) [23]. The evolution of density function theory for 2H-MoS_2 (1st principle calculations) to study the transition from bulk to monolayer has been represented in Figure 1-1c [12], [23]. Interestingly, the conduction band and valance band positions change from bulk to few layers to monolayer due to change in electronic band structure because of electron confinement in 2D lattice as shown in Figure 1.3 and Figure 1.4 eventually, showing remarkable transformation from

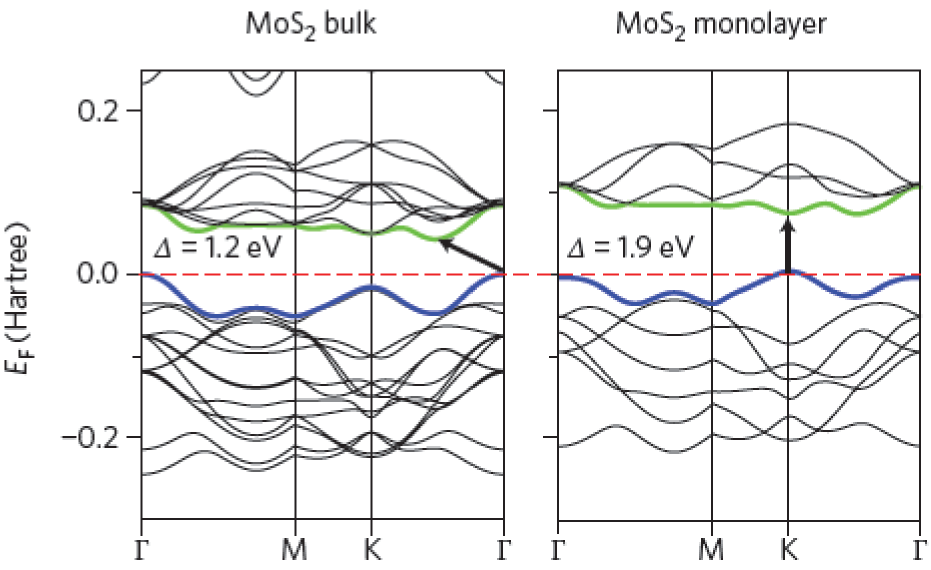

Figure 1-3 Electronic band gap structure of bulk and monolayer MoS_2 (Reprinted with permission from Wang *et al*., 2012)

bulk indirect bandgap to monolayer direct bandgap. The values for indirect and direct bandgap are 1.2 and 1.9 eV respectively for 2H-MoS_2 [17], [24]–[26] (Figure 1-3). Similarly, for WS_2 the indirect bandgap of 1.3 eV changes to direct bandgap of 2.1 eV form bulk to monolayer [17], [27], [28] (Figure 1-4).

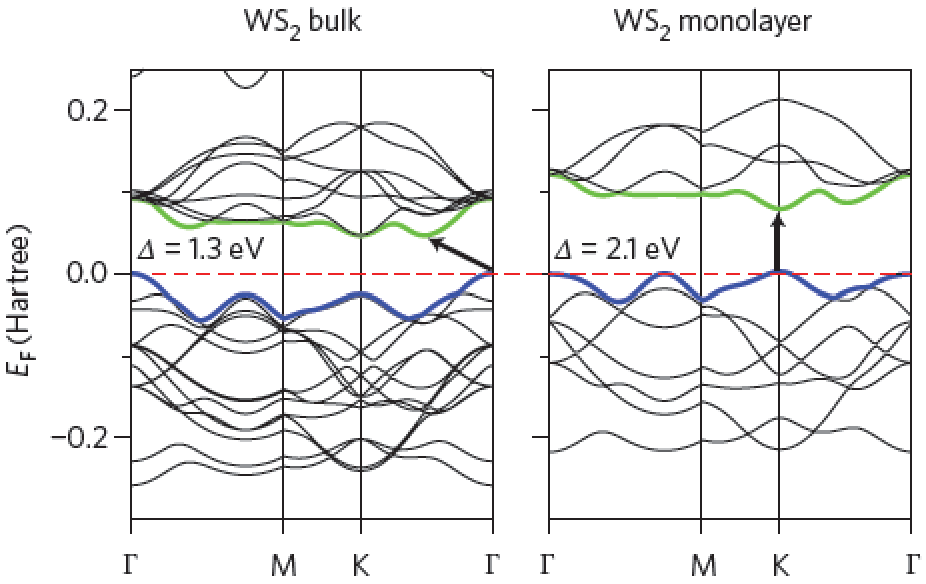

Figure 1-4 Electronic band gap structure of bulk and monolayer WS_2 (Reprinted with permission from Wang *et al*., Nature Nanotechnology, 2012)

The of top valance band and bottom of conduction bands in the monolayer TMDCs are at the same K point of the wave vector axis, which is why they show strong photoluminescence in visible range of electromagnetic spectrum. Thus, these TMDCs are widely used as absorbing materials in solar cells as well as photovoltaics and applications in various nano and optoelectronics. In practice these materials are used as channel materials for FET, in both top and back gated configuration with intrinsic mobility of $50cm^2/V.s$ and on/off ratio of more than 10^{10}.

1.4 Catalytic Properties

In monolayer MoS_2 and WS_2 the basal plans of the layers are catalytically in active due to 2H structure where both sides are sulfur layer sandwiching the Mo or W layers, whereas the edges are active site which are utilized in catalysis. Particularly, MoS_2 has been utilized for electrochemical hydrogen evolution reaction (HER) with high activity and stability. Further, the photo catalytic properties have been utilized owing to strong PL. The improvement in the HER has been reported by Ye *et al.* by oxygen plasma etching of MoS_2 crystals [29]. The strong PL in WS_2 monolayers has been utilized for many photo-catalysis as well as electrolysis applications [21], [30], [31].

1.5 Synthesis of MoS_2 and WS_2

Robert Frindt reported first adhesive tape method for MoS_2 thin layer synthesis in 1963 and subsequently in 1986 monolayer MoS_2 suspension was reported.[32], [33] Early part of 1990 saw significant development in carbon nanotubes and inorganic fullerenes followed by WS_2 and MoS_2 nanotubes and nested particles [34]–[38].

Layered 2D TMDC nano-sheets are synthesized from either top-down route like mechanical exfoliation or bottom-up processes like CVD. To, study the 2D characteristics of these materials, it is imperative that synthesized structure has to be few- and single-layer sheets, and uniform sample size is also highly desirable. To get proper sample size and uniform layer thickness CVD method is most suitable process for the synthesis of TMDCs. First CVD growth of TMDCs was demonstrated by Hofmann demonstrated MOCVD growth of MoS_2 and WS_2 on various substrates in 1988 [39]. The precursors of Mo and W hexacarbonyls of the corresponding transition metals precursors were used with vaporized sulfur or hydrogen sulfide gas. However, the films are normally thick. For the synthesis of two-dimensional atomic layers or single layers, several techniques in CVD have been developed. Liu *et al*. reported a two-step thermolysis process [40], The ammonium thiomolybdates [$(NH_4)_2MoS_4$] precursor was used onto the substrates by dip-coating, and annealed in Ar/H_2 environment at 500° C which was further converted to MoS_2 by annealing at sulfurization at 1000° C using sulfur vapor along with Ar gas. Three-layer MoS_2 was synthesized which was confirmed by high-resolution transmission electron microscopy (TEM) analysis which was transferred easily on another arbitrary substrate. The crystallinity of the crystals was significantly improved using sulfur vapors. Zhan *et al*. also reported CVD synthesis of MoS_2 by direct sulfurization of Mo metal film to get large area, few layer film [41]. Electron beam deposited Mo on SiO_2 surface was used for CVD synthesis. The subsequent sulfurization using sulfur vapor gives MoS_2 with thickness depending on deposited metal and area inside CVD furnace. Transition metal oxide precursor based methods were reported by Lee *et al*. wherein, few-layer MoS_2 was synthesized using CVD [42]. In this work, MoS_2 was synthesized by sulfurization of MoO_3. Synthesis of monolayer MoS_2 on graphene surface was reported by McCreary *et al*. [43]. $MoCl_5$ precursor as used for the as Mo source in the study. By changing the amount of precursor mono, bi and tri layer MoS_2 films were synthesized. The synthesis of TMDCs single crystal in CVD process is still a challenge till date, smaller domains of TMDCs are obtained compared to graphene crystals. However, some single crystal TMDCs were successfully synthesized in relatively large domain. The main challenge in synthesis of single crystal is reduction in nucleation density to reduce grain boundaries. Zhang *et al*. reported growth of single crystal monolayer WS_2 on single crystal sapphire substrate with WO_3 and sulfur precursors by CVD growth [44]. In this study, crystal size of upto 50 µm monolayer WS_2 was obtained. Also, monolayer WS_2 single crystal domains with size upto 370 µm was reported by Rong *et al*. in CVD growth [27]. This was achieved by controlling the supply of sulfur amount and time during the CVD process.

In this thesis, I report synthesis of the unique ribbon shaped 2D-MoS_2 structure in modified CVD method. We also successfully synthesized millimeter scale monolayer MoS_2 as well as crystals with the size of upto 100 µm. These MoS_2 and WS_2 crystals were characterized by Optical, field effect scanning electron microscopy (FE-SEM), atomic force microscopy (AFM), Raman, PL and X-Ray photoelectron spectroscopy (XPS) analysis. These CVD synthesized MoS_2 and WS_2 were further used for device fabrication in conjunction with other layered materials for optoelectronic applications.

1.6 Characterization

Multiple analysis technique has been utilized for characterization of synthesized WS_2 and MoS_2 layered materials. Qualitative confirmation for the TMDCs is mainly done by Raman study. Raman peak positions and mapping images are widely used for determining the quality of synthesized TMDCs. Other techniques such as Optical and FE-SEM were used to confirm the size and the crystals structure on SiO_2/Si substrate, which provide excellent contrast between the two. The layer nature of the TMDCs are confirmed by AFM analysis by thickness measurement. One of the exciting properties of layered TMDCs is improved PL from bulk to monolayer due to transformation to direct bandgap. Thus, PL signal intensity and full width half maximum (FWHM) provides further confirms the optical quality of MoS_2 and WS_2 layers. XPS also called as electron spectroscopy for chemical analysis (ESCA) spectra determines the chemical nature of these materials with peak area analysis confirming the relative composition of metal and chalcogen.

1.6.1 Optical Microscopy

Optical microscopy analysis was performed with the digital optical microscope VHX-500 in reflectance mode with a Moticam 2000 2.0 M pixel camera. Domain size and shapes of synthesized materials with size more than 10 µm can be clearly seen, with lesser size crystals SEM analysis was performed. The synthesis of these materials was mainly conducted on SiO_2/Si substrate which also provides excellent contrast between the two. Figure 1-5 shows optical images of CVD synthesized MoS_2 and WS_2 layers on SiO_2/Si substrate. The merging of MoS_2 crystals to form the layer is represented in Figure 1-5a. Figure 1-5b and Figure 1-5c represents synthesized MoS_2 and WS_2 crystals whereas Figure 1-5d shows ribbon structures.

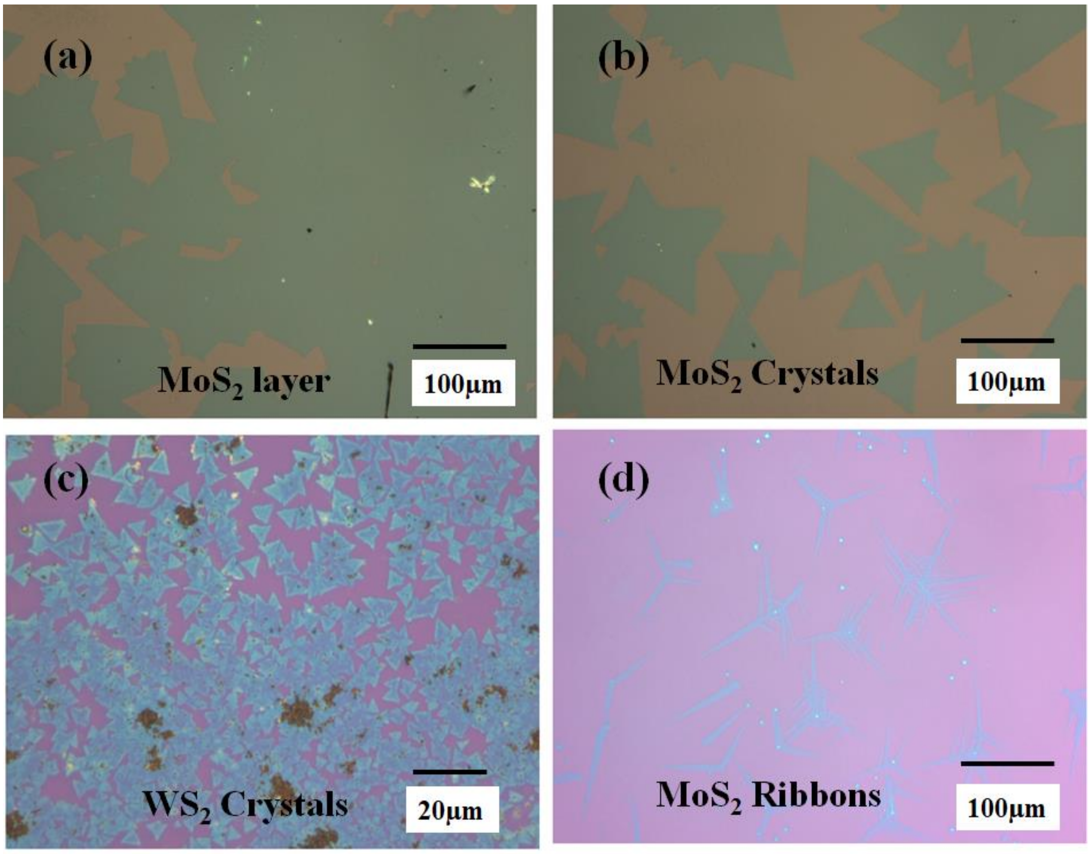

Figure 1-5 Optical images of CVD synthesized (a) MoS_2 layer formed by merging of crystals (b)MoS_2 crystals (c) WS_2 crystals and (d) MoS_2 ribbons.

1.6.2 Field emission scanning electron microscopy (FE-SEM)

FE-SEM studies were performed with JEOL JSM-7800F using lower electron detector (LED) with an accelerating voltage of 5 kV. Electron beam interaction with the sample produce secondary electrons which are converted to signal and subsequently used to construct the image. High resolution images are possible up to few micrometers. The emitted secondary electrons are from close to specimen surface which gives very sharp images.

FE-SEM analysis gives better resolution of smaller crystals as well as provides information on uniformity of the crystal or layer structure. Figure 1-6a to Figure 1-6c represents the triangular, dendritic and hexagonal shapes of WS_2 crystals respectively and Figure 1-6d shows the uniform layer of MoS_2 on SiO_2/Si substrate. The MoS_2 crystals are represented in Figure 1-6e. It should be noted that, the formation of uniform layer is achieved by merging of crystals.

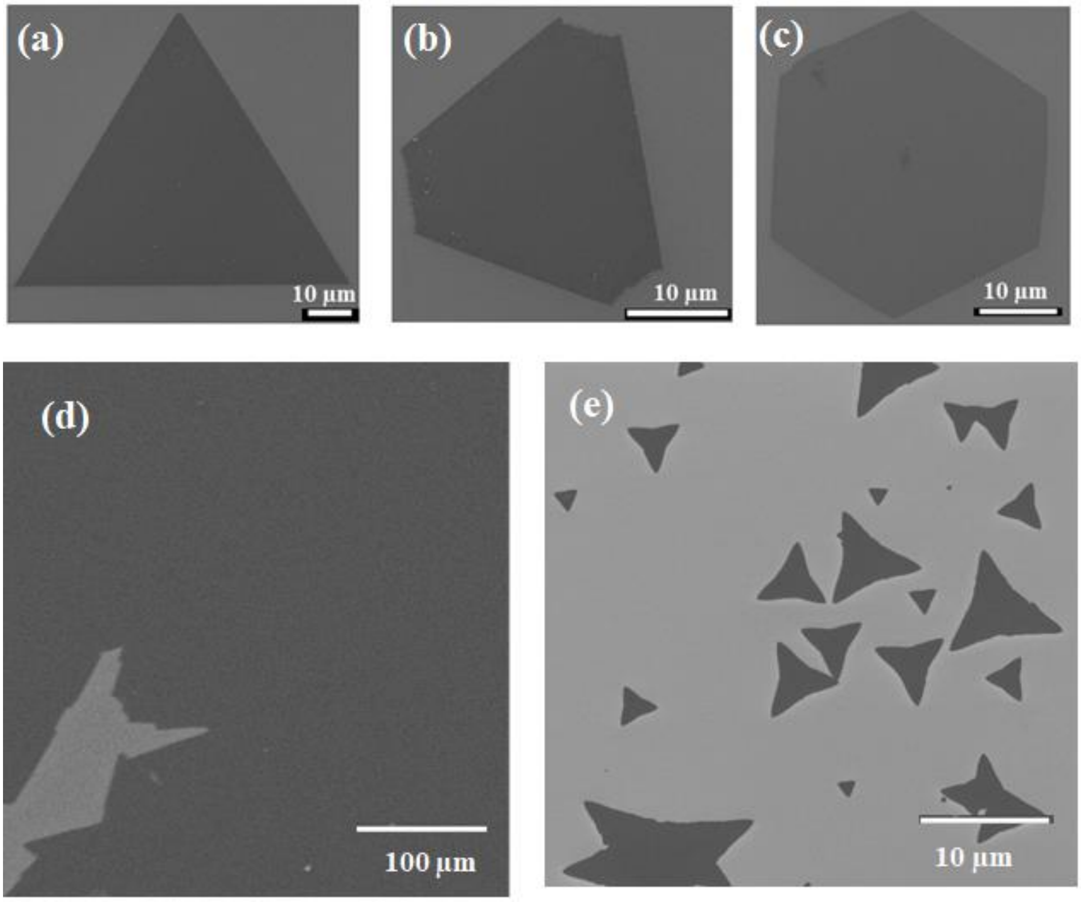

Figure 1-6 SEM images of WS_2 crystals in (a) triangular (b) Dendritic and (c) Hexagonal shape MoS_2 layer (d) and crystals (e).

1.6.3 Raman spectroscopy

Raman spectroscopy is extensively used for identification on many 2D materials as it gives finger print scattering for every material. It has historically been used for identification of graphitic materials as well as for characterization of layer numbers. Raman spectroscopy is a relatively easy, non-destructive, non-contacting, and quick measurement method to probe the inelastic scattering of light from a sample surface at room temperature at ambient pressure. The wavelength of the bands is affected by the energy of the laser, and the following wavelengths are given for a laser excitation energy of 532.08 nm, in which an NRS-3300 laser Raman spectrometer was used to take the

Raman spectra. Typical Raman spectra for MoS_2 and WS_2 shows two signature peaks at specific wavenumbers corresponding to in-plan vibration of metal and chalcogen atoms (E_{2g}) and out of plan vibration of sulfur atoms (A_{1g}).

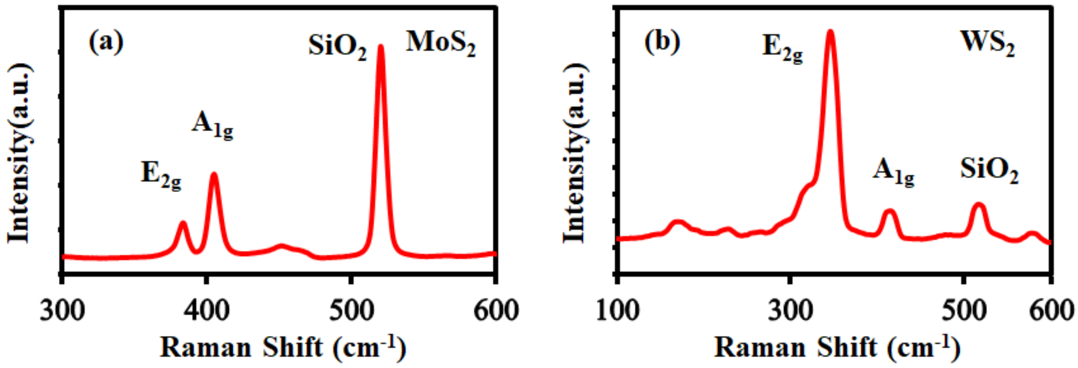

Figure 1-7 Raman Spectra for 2D (a) MoS_2 and (b) WS_2

Figure 1-7a represents typical Raman spectra for layered MoS_2. Characteristic Raman intensities corresponding to in plane Raman mode vibrations of Mo and S atoms E_{2g}-484 cm^{-1} and A_{1g}-405 cm^{-1} can be observed from the spectra. The difference between the Raman frequencies of E_{2g} and A_{1g} was found to be Δk- 21 cm^{-1} which is characteristic for 2D MoS_2. Similarly, Figure 1-7b shows Raman spectra for CVD synthesized WS_2 on SiO_2/Si substrate with Raman mode vibrations at E_{2g}- 347 cm^{-1} and A_{1g}-417 cm^{-1}. The intensity ratio of I_{A1g}/I_{E2g} was found to be 0.17 which corresponds to 2D WS_2 [42], [45].

1.6.4 Atomic force microscopy (AFM)

High resolution topographical analysis is performed with the scanning probe with resolution up to fractions of nano-meters. The AFM study in this thesis was mainly focused on analyzing the thickness of the synthesized WS_2 and MoS_2 crystals as well as the uniformity of the layers. AFM study was carried out with a JSPM-5200 scanning probe microscope. The atomic arrangement in 2D structure for these crystals shows theoretical values of 0.64 and 0.69 nm for single layer MoS_2 and WS_2 respectively.

Figure 1.8a shows AFM image of CVD synthesized WS_2 crystal on SiO_2/Si substrate with the thickness of 0.9 nm also Figure 1.8b shows MoS_2 crystal with thickness of 0.8 nm which are in close agreement with the theoretical values [46]. Further, smooth layer surface was observed with clean crystals without any visible defects.

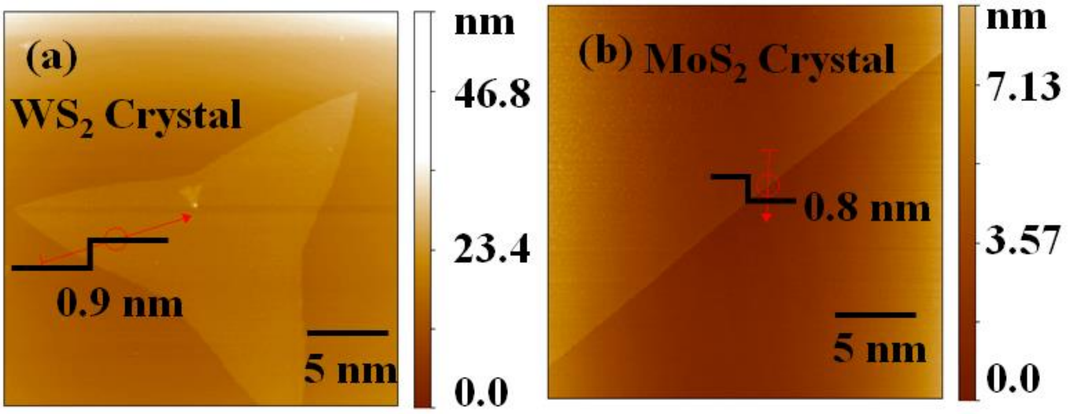

Figure 1-8 AFM images of monolayer (a) WS$_2$ and (b) MoS$_2$ crystals synthesized by APCVD

1.6.5 Photoluminescence spectroscopy (PL)

In the direct bandgap semiconductors such as WS$_2$ and MoS$_2$, the energy gap between the valance and conduction band is such that the absorption of light in visible region is observed. Electronic excitation by absorption of photon and subsequent relaxation to lower energy state occurs by emission of radiation, which is known as PL. The bulk to monolayer transforms the indirect bandgap of these TMDCs to direct bandgap semiconductors. In monolayer, MoS$_2$ and WS$_2$ gives strong PL signals at 684 nm and 650 nm respectively. The optical quality and bandgap can be confirmed by the PL study.

In this thesis, PL measurements were performed with a confocal laser scanning microscope (NX-3DFLIM-N03, Tokyo Instruments, and Japan) equipped with an Nd: YVO$_4$ diode laser.

Figure 1-9a shows PL signal for MoS$_2$ at excitation wavelength of 532.2nm. Sharp peak with full width half maximum (FWHM) of around 40 cm^{-1} shows synthesis of good optical quality MoS$_2$ layer. Similarly, for WS$_2$ strong PL signal at 650 nm was observed for CVD synthesized layer (b). FWHM was calculated to be around 35 cm^{-1} with the bandgap of 1.91 eV. The bandgap of MoS$_2$ was calculated to be 1.81 eV [28], [47].

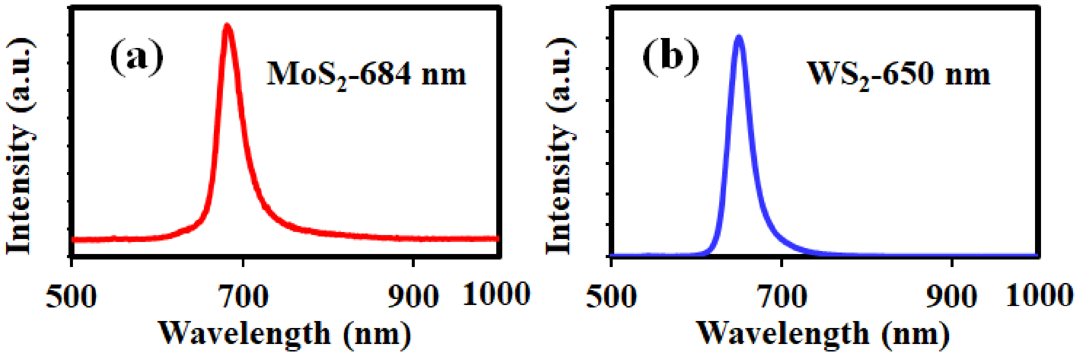

Figure 1-9 PL spectra for monolayer (a) MoS_2 and (b) WS_2

1.6.6 X-ray photoelectron spectroscopy (XPS)

X-ray Photoelectron Spectroscopy (XPS) is a surface analysis with a typical depth of 5-10 nm, used to determine the quantitative atomic composition, chemical and electronic states of elements in the sample. The process works by irradiating a sample with monochromatic X-rays, typically mono-energetic Al Kα X-rays, resulting in the emission of photoelectrons from the surface of the sample. An electron energy analyzer is used to measure the kinetic energy of the emitted photoelectrons over a range of electron kinetic energies. The emitted atoms cause peaks to appear in the spectrum from characteristic energies of electrons. From the binding energy and intensity of a photoelectron peak, the elemental identity, chemical state, and quantity of a detected element can be determined. XPS analysis was performed by VersaProbe using monochromated Al Kα excitation source (1486.6 eV).

Typical XPS spectra for CVD synthesized MoS_2 and WS_2 is represented in Figure 1-7. Figure 1-10a and Figure 1-10b represents the XPS core-level spectra with chemical state doublet Mo 3d peaks ($Mo3d_{5/2}$ and $Mo3d_{3/2}$) at 230 and 233 eV and S 2p peaks ($S2p_{3/2}$ and $S2p_{1/2}$) at 162 and 164 eV respectively. The chemical state doublet for W 4f peaks ($W4f_{7/2}$ and $W4f_{5/2}$) and S 2p peaks ($S2p_{3/2}$ and $S2p_{1/2}$) peaks are represented in Figure 1-10c and Figure 1-10d respectively [48], [49].

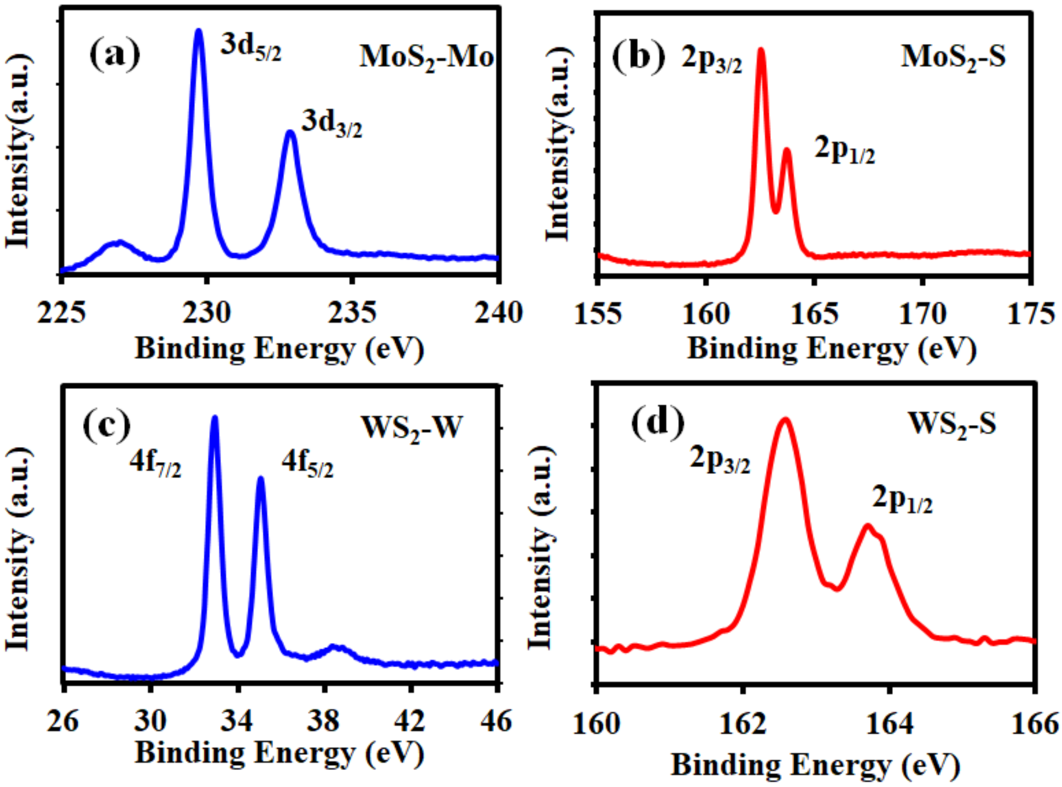

Figure 1-10 XPS spectra for (a) MoS_2-Mo 3d transition (b) MoS_2-S 2p transition (c) WS_2-W 4f transition and (d) WS_2-S 2p transition.

1.7 Atmospheric Stability

Although, the layered structure of these TMDCs shows inert character at the basal plan in 2D state, recent studies show significant degradation over long term exposure to ambient environment. These materials show poor stability on long term exposure to ambient environment. The stability study performed over the period of 10 months to a year, shows formation of regular degradation patterns along the grain boundaries with ageing effect with morphological changes, cracking as well as severe quenching of PL. The stability study of these WS_2 and MoS_2 layered materials is quite important in order to use them for various applications [50]. Due to exposed edges as well as defects during the synthesis process increase the rate of degradation. The effect of humidity, temperature, chemical environment as well as the uniformity in the crystal lattice of the layers are the factors to be considered, which significantly affects the stability of the layers [51], [52]. In this thesis, we report systematic study of the degradation behavior of WS_2 crystals over the period of 10 to 12 months. Further we explored the possibility of dry encapsulation at room temperature with carbonaceous layer using plasma deposition.

1.8 Encapsulation of TMDCs

In order to utilize the TMDCs for practical application for device fabrication, one has to find effective protective method to prevent environmental degradation from long term exposure. Previous methods include, coating of poly(methyl methacrylate) (PMMA) and Parylene C on MoS_2 and WS_2 layers to protect from ageing by Gao *et al*. [53]. Also, protective layer of PMMA/h-BN has been used for protection of WSe_2 layer from degradation, reported by Ahn *et al*. [54]. Further, Woodhead *et al*. reported the Optical solution for degradation protection [55]. The encapsulation layer usually affects the TMDCs by exerting compressive or other lattice strains among the other factors. The growth of TMDCs on graphene showed improved shelf life of these layered materials by electronic interaction. In this thesis we described rapid and dry method for effective encapsulation of MoS_2 using Microwave assisted Surface wave plasma (MW-SWP) deposition of carbonaceous layer. The heat stability upto 200 °C for more than 1 hr. was observed with stable photoconductivity without any damage to MoS_2. This method can be extended to other TMDCs for effective encapsulation.

1.9 Applications of WS_2 and MoS_2

Layered TMDCs have attracted significant attention for electronic and optoelectronic applications [53], [54]. Field effect transistor (FET) fabricated with monolayer MoS_2 showed good room temperature mobility, and significant switching characteristics with on/off current ratio $\sim 10^{10}$ [56], [57]. Thus, utilization of these properties of MoS_2 has been explored in many studies. Integration of the MoS_2 layers with three-dimensional (3D) bulk semiconductor (such as silicon, germanium, gallium nitride, etc.) has been also for fabrication of 2D/3D active heterojunction devices [58]–[63]. The 2D TMDCs can be readily integrated to fabricate a heterostructure without constrains of lattice matching due to the dangling bond free lattice and strong Van der Waals interaction.

MoS_2 and WS_2 are direct bandgap semiconductors with high optical absorption in visible range and large exciton binding energy. These TMDCs have attracted significant interest in nanoelectronics, high-performance photodetectors and solar cell applications [55], [64]–[66]. Besides the TMDC materials mentioned above, heterostructures based on TMDC materials are attracting great interest. Bernardi *et al*. have theoretically demonstrated that bilayer solar cells of MoS_2/graphene of 1 nm thickness could achieve over 1% power conversion efficiency [67]. These theoretical works predicted that bilayers of TMDC/TMDC or TMDC/graphene could be promising in various fields of applications. There are several other experimental works on TMDC based heterostructures. Another important application of TMDCs materials is for fabrication of photodiode, due to presence of a direct bandgap fast responsive (high speed) with excellent photosensitivity than that of Si device can be developed.

The typical performance of silicon-based p-n junction photoresponsive devices that are commercially available shows efficiency in the range of 0.1 A/W in the wavelength range of 500 to 900 nm. These devices show significant decrease in performance in the short wavelength range (<500nm) due to surface recombination. Again, Si device limited to visible and near-infrared (IR), due to which low bandgap materials (i.e. Ge) and their hetero structure has been investigated for IR photodiode. Stebel *et al*. reported significant decrease in photoresponse beyond 1000 nm for boron doped silicon p-n junction heterostructure [68].

In this prospect, I have explored the possibility of effective heterojunction fabrication of 2D MoS_2 with the narrow bandgap germanium (Ge) and wide bandgap semiconductor CuI. The effective self-powered photoresponsive device was successfully fabricated with the Ge-MoS_2 heterostructure. Again, the p-type CuI and n-type MoS_2 layers showed formation of excellent heterojunction with spontaneous charge separation at the interface. CuI was fabricated by two methods in order to analyze the interface quality and better device performance. First being solid phase iodination of Cu (thin layer deposited by thermal evaporation at low pressure) and subsequent iodization using iodine beads at atmospheric pressure to form CuI and second method was direct deposition of CuI at low pressure thermal deposition. The fabrication of heterojunction with the CVD synthesized MoS_2 layers, their interfaces and device characteristics were analyzed in detail and included in this thesis.

1.10 Motivation and objectives of current work

TMDCs are emerging new generation materials with interesting properties for various catalytic, electronic and optical applications. The conductive properties of these TMDCs varies from insulating to superconducting. Contrary to graphene, they also show semiconducting nature with direct bandgap. Thus, they are widely explored for electronic applications which compensate the limitations faced by graphene. As, the bandgap of TMDCs such as MoS_2 and WS_2 is highly suitable for fabrication of field-effect transistors (FETs) they show great prospect for future electronic. Among the TMDCs, monolayer MoS_2 and WS_2 are particularly interesting for optoelectronic devices due to their direct bandgap (1.7-1.8 eV) in the visible wavelength range. Presently, synthesis of high quality TMDCs layers and understanding their growth mechanism is of particular interest. Again, the atmospheric degradation of TMDCs layer is a hurdle for integration in device fabrication. Considering these facts, I have explored high quality TMDCs layer growth by CVD technique.

The objective of this thesis is to synthesize better quality and unique shape of TMDCs using CVD technique, studying the stability of the synthesized material for photoresponsive device application. The CVD synthesis process has significant advantage with better optical quality, large area uniform layer synthesis of MoS_2 or WS_2. Thus, I have used the CVD method to synthesize MoS_2 and WS_2 crystals and investigated about their various shapes with respect to growth parameters. In CVD growth the reaction process of Mo and W precursors (in this experiments MoO_3 and WO_3) with sulfur is very critical to achieve high quality layer growth. After synthesis, the atmospheric stability of the CVD synthesized TMDCs layers is crucial factor for practical device applications. Thus, the atmospheric stability of the WS_2 crystals has been studied. The degradation mechanism upon long term environmental exposure to ambient condition was studied in detail. After which, effective degradation prevention technique by encapsulation with foreigner material without damaging the TMDCs was developed. Effective dry encapsulation for stable performance even at high temperature upto 200 °C for 1 hr. was achieved and compiled in the thesis. Learning from the synthesis and degradation process of TMDCs layer, optoelectronic device fabrication in conjunction with other semiconducting materials was investigated. Fabrication of heterostructures with a low bandgap semiconductor (Ge) and wide bandgap semiconductor (CuI) for photoresponsive devices was explored. These, the research findings on synthesis, stability study with effective encapsulation and optoelectronic applications of MoS_2 and WS_2 layers were compiled systematically in this thesis.

1.11 Organization of the dissertation

This thesis contributes to the synthesis, degradation study, encapsulation and application of CVD synthesized MoS_2 and WS_2 crystals and layer structures. Effective approach for synthesis with detailed investigation of degradation process as well as encapsulation for long term stability is compiled. Detailed characterization with fabrication of heterostructure with other layered materials was explored and reported.

Chapter 1 describes the general introduction of 2D TMDCs materials including graphene about their properties, applications and physical and chemical synthesis methods.

Chapter 2 describes CVD synthesis of unique 2D ribbon structure with uni, bi and tri-directional growth. Detailed description of diffusion-controlled growth with analysis of edge terminations are included in this chapter along with synthesis of crystals and layers of MoS_2 and WS_2 which are used for further study.

Chapter 3 deals with the stability study with long term environmental exposure of TMDCs. Degradation of the crystals has been studied and protective encapsulation as well as dry coating without any damage to MoS_2 crystals is explained. This paved the way for deposition of other semiconducting materials on MoS_2 for optoelectronic application as well as coating material against the degradation.

Chapter 4 explains the application of MoS_2 by formation of heterostructure with another layered semiconductor Ge. The Ge/MoS_2 heterostructure has significant prospect for developing broadband photoresponsivity device beyond the Si device wavelength. High optical quality MoS_2 synthesized using APCVD on SiO_2 substrate was used for thermal deposition of Ge. Broadband, self-powered photo detecting device was fabricated with ultrathin heterojunction for various optoelectronic applications.

Chapter 5 describes the formation of γ-CuI (solid phase iodination as well as direct thermal deposition) MoS_2 heterojunction on sapphire substrate. In this case, p-type CuI with a band gap of 3.0 eV is studied in conjunction with MoS_2 for photoresponsive device application. PL analysis showed significant quenching attributing to exciton recombination. Thus, the heterostructure showed potential for application in photoresponsive devices.

Chapter 6 summarizes the whole thesis and future prospects.

1.12 References

[1] Z. Zeng, C. Tan, X. Huang, S. Bao, and H. Zhang, "Growth of noble metal nanoparticles on single-layer TiS_2 and TaS_2 nanosheets for hydrogen evolution reaction," *Energy Environ. Sci.*, vol. 7, no. 2, pp. 797–803, Jan. 2014.

[2] F. Li, K. Tu, and Z. Chen, "Versatile Electronic Properties of VSe_2 Bulk, Few-Layers, Monolayer, Nanoribbons, and Nanotubes: A Computational Exploration," *J. Phys. Chem. C*, vol. 118, no. 36, pp. 21264–21274, Sep. 2014.

[3] L. Ma *et al.*, "A metallic mosaic phase and the origin of Mott-insulating state in 1T-TaS_2," *Nat. Commun.*, vol. 7, no. 1, p. 10956, Dec. 2016.

[4] X. Xi *et al.*, "Strongly enhanced charge-density-wave order in monolayer $NbSe_2$," *Nat. Nanotechnol.*, vol. 10, no. 9, pp. 765–769, Sep. 2015.

[5] M. M. Ugeda *et al.*, "Characterization of collective ground states in single-layer NbSe2," Jun. 2015.

[6] T. R. Chang *et al.*, "Prediction of an arc-tunable Weyl Fermion metallic state in $Mo_xW_{1-x}Te_2$," *Nat. Commun.*, vol. 7, no. 1, p. 10639, Dec. 2016.

[7] K. Sugawara *et al.*, "Unconventional Charge-Density-Wave Transition in Monolayer 1T -$TiSe_2$," *ACS Nano*, vol. 10, no. 1, pp. 1341–1345, Jan. 2016.

[8] Y. I. Joe *et al.*, "Emergence of charge density wave domain walls above the superconducting dome in 1T-$TiSe_2$," *Nat. Phys.*, vol. 10, no. 6, pp. 421–425, Jun. 2014.

[9] B. Radisavljevic, A. Radenovic, J. Brivio, V. Giacometti, and A. Kis, "Single-layer MoS_2 transistors," *Nat. Nanotechnol.*, vol. 6, no. 3, pp. 147–150, Mar. 2011.

[10] W. Yang *et al.*, "Electrically Tunable Valley-Light Emitting Diode (vLED) Based on CVD-Grown Monolayer WS_2," *Nano Lett.*, vol. 16, no. 3, pp. 1560–1567, Mar.

2016.

[11] A. Thangaraja, S. M. Shinde, G. Kalita, and M. Tanemura, “An effective approach to synthesize monolayer tungsten disulphide crystals using tungsten halide precursor,” *Appl. Phys. Lett.*, vol. 108, no. 5, p. 053104, Feb. 2016.

[12] A. Splendiani *et al.*, “Emerging photoluminescence in monolayer MoS2,” *Nano Lett.*, vol. 10, no. 4, pp. 1271–1275, Apr. 2010.

[13] K. F. Mak, C. Lee, J. Hone, J. Shan, and T. F. Heinz, “Atomically Thin MoS_2 : A New Direct-Gap Semiconductor.”

[14] A. K. Geim and I. V. Grigorieva, “Van der Waals heterostructures,” *Nature*, vol. 499, no. 7459, pp. 419–425, 2013.

[15] A. H. Castro Neto, F. Guinea, N. M. R. Peres, K. S. Novoselov, and A. K. Geim, “The electronic properties of graphene,” *Rev. Mod. Phys.*, vol. 81, no. 1, pp. 109–162, Jan. 2009.

[16] K. F. Mak, K. He, J. Shan, and T. F. Heinz, “Control of valley polarization in monolayer MoS_2 by optical helicity.”

[17] Q. H. Wang, K. Kalantar-Zadeh, A. Kis, J. N. Coleman, and M. S. Strano, “Electronics and optoelectronics of two-dimensional transition metal dichalcogenides,” *Nat. Nanotechnol.*, vol. 7, no. 11, pp. 699–712, Nov. 2012.

[18] O. Lopez-Sanchez, D. Lembke, M. Kayci, A. Radenovic, and A. Kis, “Ultrasensitive photodetectors based on monolayer MoS_2,” *Nat. Nanotechnol.*, vol. 8, no. 7, pp. 497–501, 2013.

[19] A. Pospischil, M. M. Furchi, and T. Mueller, “Solar-energy conversion and light emission in an atomic monolayer p-n diode,” *Nat. Nanotechnol.*, vol. 9, no. 4, pp. 257–261, 2014.

[20] J. Kibsgaard, Z. Chen, B. N. Reinecke, and T. F. Jaramillo, “Engineering the surface structure of MoS_2 to Â preferentially expose active edge sites for Â electrocatalysis,” *Nat. Mater.*, vol. 11, no. 11, pp. 963–969, 2012.

[21] D. Voiry *et al.*, “Enhanced catalytic activity in strained chemically exfoliated WS_2 nanosheets for hydrogen evolution,” *Nat. Mater.*, vol. 12, no. 9, pp. 850–855, Sep. 2013.

[22] S. Wang *et al.*, “Shape Evolution of Monolayer MoS_2 Crystals Grown by Chemical Vapor Deposition,” *Chem. Mater.*, vol. 26, pp. 6371–6379, 2014.

[23] B. Radisavljevic, A. Radenovic, J. Brivio, V. Giacometti, and A. Kis, “Single-layer MoS_2 transistors,” *Nat. Nanotechnol.*, vol. 6, no. 3, pp. 147–150, 2011.

[24] Z. Yin *et al.*, “Single-layer MoS2phototransistors,” *ACS Nano*, vol. 6, no. 1, pp. 74–80, 2012.

[25] S. M. Shinde, G. Kalita, and M. Tanemura, “Fabrication of poly(methyl methacrylate)-MoS_2/graphene heterostructure for memory device application,” *J. Appl. Phys.*, vol. 116, no. 21, 2014.

[26] Y. Huang, J. Guo, Y. Kang, Y. Ai, and C. M. Li, “Two dimensional atomically thin MoS_2 nanosheets and their sensing applications,” *Nanoscale*, vol. 7, no. 46, pp. 19358–19376, 2015.

[27] Y. Rong *et al.*, “Controlling sulphur precursor addition for large single crystal domains of WS_2,” *Nanoscale*, vol. 6, no. 20, pp. 12096–12103, 2014.

[28] I. Bilgin *et al.*, “Chemical Vapor Deposition Synthesized Atomically Thin Molybdenum Disulfide with Optoelectronic-Grade Crystalline Quality,” *ACS Nano*, vol. 9, no. 9, pp. 8822–8832, Sep. 2015.

[29] G. Ye *et al.*, “Defects Engineered Monolayer MoS_2 for Improved Hydrogen Evolution Reaction,” *Nano Lett.*, vol. 16, no. 2, pp. 1097–1103, 2016.

[30] H. Wang *et al.*, “Integrated Circuits Based on Bilayer MoS_2 Transistors,” *Nano Lett.*, vol. 12, no. 9, pp. 4674–4680, Sep. 2012.

[31] D. Kong, J. J. Cha, H. Wang, H. R. Lee, and Y. Cui, “First-row transition metal dichalcogenide catalysts for hydrogen evolution reaction,” *Energy Environ. Sci.*, vol. 6, no. 12, p. 3553, Nov. 2013.

[32] R. F. Frindt and A. D. Yoffe, “Physical Properties of Layer Structures: Optical Properties and Photoconductivity of Thin Crystals of Molybdenum Disulphide,” *Proc. R. Soc. A Math. Phys. Eng. Sci.*, vol. 273, no. 1352, pp. 69–83, Apr. 1963.

[33] M. A. Gee, R. F. Frindt, P. Joensen, and S. R. Morrison, “Inclusion compounds of MoS_2,” *Mater. Res. Bull.*, vol. 21, no. 5, pp. 543–549, May 1986.

[34] T. W. Ebbesen and P. M. Ajayan, “Large-scale synthesis of carbon nanotubes,” *Nature*, vol. 358, no. 6383, pp. 220–222, Jul. 1992.

[35] S. Iijima and T. Ichihashi, “Single-shell carbon nanotubes of 1-nm diameter,” *Nature*, vol. 363, no. 6430, pp. 603–605, Jun. 1993.

[36] M. S. Dresselhaus, G. Dresselhaus, and R. Saito, “Physics of carbon nanotubes,” *Carbon N. Y.*, vol. 33, no. 7, pp. 883–891, Jan. 1995.

[37] Y. Feldman, E. Wasserman, D. J. Srolovitz, and R. Tenne, “High-Rate, Gas-Phase Growth of MoS_2 Nested Inorganic Fullerenes and Nanotubes,” *Science (80).*, vol. 267, no. 5195, pp. 222–225, Jan. 1995.

[38] I. Silaghi-Dumitrescu, I. Haiduc, and D. B. Sowerby, “Fully inorganic (carbon-free) fullerenes? The boron-nitrogen case,” *Inorg. Chem.*, vol. 32, no. 17, pp. 3755–3758, Aug. 1993.

[39] W. K. Hofmann, “Thin films of molybdenum and tungsten disulphides by metal

organic chemical vapour deposition," *J. Mater. Sci.*, vol. 23, no. 11, pp. 3981–3986, Nov. 1988.

[40] K. K. Liu *et al.*, "Growth of large-area and highly crystalline MoS_2 thin layers on insulating substrates," *Nano Lett.*, vol. 12, no. 3, pp. 1538–1544, 2012.

[41] Y. Zhan, Z. Liu, S. Najmaei, P. M. Ajayan, and J. Lou, "Large-area vapor-phase growth and characterization of MoS_2 atomic layers on a SiO_2 substrate," *Small*, vol. 8, no. 7, pp. 966–971, 2012.

[42] Y.-H. Lee *et al.*, "Synthesis of Large-Area MoS_2 Atomic Layers with Chemical Vapor Deposition," *Adv. Mater.*, vol. 24, no. 17, pp. 2320–2325, 2012.

[43] K. M. McCreary *et al.*, "Large-area synthesis of continuous and uniform MoS_2 monolayer films on graphene," *Adv. Funct. Mater.*, vol. 24, no. 41, pp. 6449–6454, 2014.

[44] Y. Zhang *et al.*, "Controlled Growth of High-Quality Monolayer WS_2 Layers on Sapphire and Imaging Its Grain Boundary," *ACS Nano*, vol. 7, no. 10, pp. 8963–8971, 2013.

[45] Y. Gao *et al.*, "Large-area synthesis of high-quality and uniform monolayer WS2on reusable Au foils," *Nat. Commun.*, vol. 6, p. 8569, 2015.

[46] D. J. Trainer *et al.*, "Inter-Layer Coupling Induced Valence Band Edge Shift in Mono- to Few-Layer MoS_2," *Sci. Rep.*, vol. 7, no. 1, p. 40559, Dec. 2017.

[47] S. M. Shinde *et al.*, "Stacking-controllable interlayer coupling and symmetric configuration of multilayered MoS_2," *NPG Asia Mater.*, vol. 10, no. 2, p. e468, Feb. 2018.

[48] S. McDonnell, R. Addou, C. Buie, R. M. Wallace, and C. L. Hinkle, "Defect-Dominated Doping And Contact Resistance in MoS_2," *ACS Nano*, vol. 8, no. 3, pp. 2880–2888, 2014.

[49] J. Gao, B. Li, J. Tan, P. Chow, T. M. Lu, and N. Koratkar, "Aging of Transition Metal Dichalcogenide Monolayers," *ACS Nano*, vol. 10, no. 2, pp. 2628–2635, 2016.

[50] Y. Rong, K. He, M. Pacios, A. W. Robertson, H. Bhaskaran, and J. H. Warner, "Controlled preferential oxidation of grain boundaries in monolayer tungsten disulfide for direct optical imaging," *ACS Nano*, vol. 9, no. 4, pp. 3695–3703, 2015.

[51] Y. Liu *et al.*, "Thermal Oxidation of WSe_2 Nanosheets Adhered on SiO_2/Si Substrates," *Nano Lett.*, vol. 15, no. 8, pp. 4979–4984, Aug. 2015.

[52] C. S. Woodhead *et al.*, "Increasing the light extraction and longevity of TMDC monolayers using liquid formed micro-lenses," *2D Mater.*, vol. 4, no. 1, p. 015032, Dec. 2016.

[53] K. F. Mak, K. He, J. Shan, and T. F. Heinz, “Control of valley polarization in monolayer MoS_2 by optical helicity,” *Nat. Nanotechnol.*, vol. 7, no. 8, pp. 494–498, 2012.

[54] J. K. Ellis, M. J. Lucero, and G. E. Scuseria, “The indirect to direct band gap transition in multilayered MoS_2 as predicted by screened hybrid density functional theory,” *Appl. Phys. Lett.*, vol. 99, no. 26, p. 261908, Dec. 2011.

[55] R. Cheng *et al.*, “Electroluminescence and photocurrent generation from atomically sharp WSe_2/MoS_2 heterojunction p-n diodes,” *Nano Lett.*, vol. 14, no. 10, pp. 5590–5597, 2014.

[56] Y. Yoon, K. Ganapathi, and S. Salahuddin, “How Good Can Monolayer MoS_2 Transistors Be?,” *Nano Lett.*, vol. 11, no. 9, pp. 3768–3773, Sep. 2011.

[57] R. Ganatra and Q. Zhang, “Few-layer MoS_2: A promising layered semiconductor,” *ACS Nano*, vol. 8, no. 5, pp. 4074–4099, May 2014.

[58] S. Qiao *et al.*, “A vertically layered MoS_2/Si heterojunction for an ultrahigh and ultrafast photoresponse photodetector,” *J. Mater. Chem. C*, vol. 6, no. 13, pp. 3233–3239, Mar. 2018.

[59] L. Wang *et al.*, “MoS_2/Si Heterojunction with Vertically Standing Layered Structure for Ultrafast, High-Detectivity, Self-Driven Visible-Near Infrared Photodetectors,” *Adv. Funct. Mater.*, vol. 25, no. 19, pp. 2910–2919, May 2015.

[60] S. Krishnamoorthy *et al.*, “High current density 2D/3D MoS_2/GaN Esaki tunnel diodes,” *Appl. Phys. Lett.*, vol. 109, no. 18, p. 183505, Oct. 2016.

[61] K. Zhang *et al.*, “Large scale 2D/3D hybrids based on gallium nitride and transition metal dichalcogenides,” *Nanoscale*, vol. 10, no. 1, pp. 336–341, Dec. 2018.

[62] D. Ruzmetov *et al.*, “Van der Waals interfaces in epitaxial vertical metal/2D/3D semiconductor heterojunctions of monolayer MoS_2 and GaN,” *2D Mater.*, vol. 5, no. 4, p. 045016, Aug. 2018.

[63] Y. Zhang *et al.*, “In Situ Fabrication of Vertical Multilayered MoS_2/Si Homotype Heterojunction for High-Speed Visible-Near-Infrared Photodetectors,” *Small*, vol. 12, no. 8, pp. 1062–1071, Feb. 2016.

[64] O. Lopez-Sanchez, D. Lembke, M. Kayci, A. Radenovic, and A. Kis, “Ultrasensitive photodetectors based on monolayer MoS_2,” *Nat. Nanotechnol.*, vol. 8, no. 7, pp. 497–501, Jul. 2013.

[65] X. Hong *et al.*, “Ultrafast charge transfer in atomically thin MoS_2/WS_2 heterostructures,” *Nat. Nanotechnol.*, vol. 9, no. 9, pp. 682–686, Sep. 2014.

[66] M. L. Tsai *et al.*, “Monolayer MoS_2 heterojunction solar cells,” *ACS Nano*, vol. 8, no. 8, pp. 8317–8322, 2014.

[67] D. Mahalu, M. Peisach, W. Jaegermann, A. Wold, and R. Tenne, “Controlled photocorrosion of tungsten diselenide: influence of molecular oxygen,” *J. Phys. Chem.*, vol. 94, no. 21, pp. 8012–8013, Oct. 1990.

[68] L. Stebel *et al.*, “A Modular Prototype Detector for Scintimammography Imaging,” in *IEEE Nuclear Science Symposium Conference Record, 2005*, vol. 5, pp. 3027–3031.

CHAPTER 2

2. Synthesis of MoS_2 Crystals and Continuous film by CVD in sulfur enriched environment

2.1 Introduction

In this chapter, CVD synthesis of MoS_2 ribbons along with other crystal structures and continuous layers has been described in detail. The focus of this chapter is on growth of unique crystal shapes depending on the CVD conditions. As discussed in chapter 1 the monolayer TMDCs are widely used in nanoelectronic, optoelectronic and catalytic applications [1]–[7]. Unique properties of these materials have triggered various developments in 2D materials research [8]–[13]. Particularly, MoS_2 has been significantly explored for FET, heterojunction photovoltaic, HER and various other applications [12]–[20]. Also, fabrication of in-plane and vertical heterostructures with other semiconductors are also of significant interest for novel electronics device applications [21]–[25].The other fascinating aspects of MoS_2 layers are catalytic and sensing abilities in presence of particular sharp edge structures with possible molybdenum and sulfur edge terminations [7], [13], [15], [26]. Developing high quality dichalcogenides layered materials with particular structures is of great importance considering the various prospective applications. The MoS_2 layered materials have been derived by physical or chemical exfoliation, hydrothermal synthesis, physical vapor deposition and CVD technique [20], [27]–[36] on desirable substrates. The CVD technique has been explored to synthesize uniform and high quality MoS_2 and other TMDCs layers with large domain size and continuous film [28], [33]–[37]. Various domain shapes and size of TMDCs crystals have been obtained using CVD technique viz., triangular, hexagonal, truncated triangular, three point and six point star shaped etc. [38]. It has been demonstrated that the crystals shapes and size can be controlled with the thermodynamic and kinetic growth factors [39]. Unidirectional dichalcogenides monolayer ribbons are also of significant interest owing to its unique properties, however the growth of ribbon is quite challenging than the other form of TMDCs crystals [40]–[42]. In contrast to previous findings, I have demonstrated an approach to synthesize unidirectional and bi (V-shape with 60° and 120°) or tri-directional (Y-shape with 120°) MoS_2 ribbons and their other branched structures with particular edge terminations along with crystals and continuous film by the CVD method. It is shown that, the MoS_2 ribbons can be synthesized on SiO_2/Si substrate by the CVD method in sulfur enriched condition. The growth method of MoS_2 ribbons and their branched structures with respect to position of the substrate and precursor along with other experimental parameters is explained in this chapter.

Considering the high edge density and low photoluminescence of these ribbon structures, the use is limited to catalysis and electrochemical applications. Instead, in this thesis high optical quality triangular crystals are studied for their atmospheric stability and the 2D-layers are utilized for photo responsive device fabrication.

2.2 Experimental details

The MoS_2 ribbons were grown by a thermal CVD method on SiO_2/Si substrates with optimized experimental parameters. The synthesis was executed in two individually controlled quartz tube furnaces using argon and hydrogen (3%) gas mixture at atmospheric pressure. The substrates were cleaned by sonication using acetone and subsequently with isopropyl alcohol (IPA) for 15 minutes. The substrate was dried using pure argon gas to avoid atmospheric contamination. The size of SiO_2/Si substrate was 6 cm * 2.5 cm. The MoO_3 powder (10 mg) in a ceramic boat covered with the cleaned SiO_2/Si substrates (face down) heated at 750 °C in the high-temperature furnace (HTF) as shown in Figure 2-1a. The substrate was placed in center of the boat leaving small gap between head and tail of boat for passage of gas as shown in Figure 2-1b.

The sulfur boat and MoO_3 boat were placed at either end of the smaller quartz tube (inner diameter 3.5 cm and length 20 cm), and this tube was inserted into big quartz tube. Sulfur powder (1g) in ceramic boat was loaded into the quartz tube of length 90 cm and diameter of 4.5 cm. It was placed in a low temperature furnace (LTF) heated to 180 °C. The distance between center of MoO_3 boat and sulfur boat was 15 cm. 100 sccm of mixture gas was used during entire experiment (3% hydrogen and 97% argon). The mixture gas was purged through the quartz tube for 5 minutes before starting the experiment and then both the furnaces were started at the same time. After HTF reached to 750 °C, the growth was carried out for 30 min. After completion of growth, sulfur zone was switched off and cooled down to prevent any sulfur accumulation on grown MoS_2 after that HTF was normally cooled to room temperature.

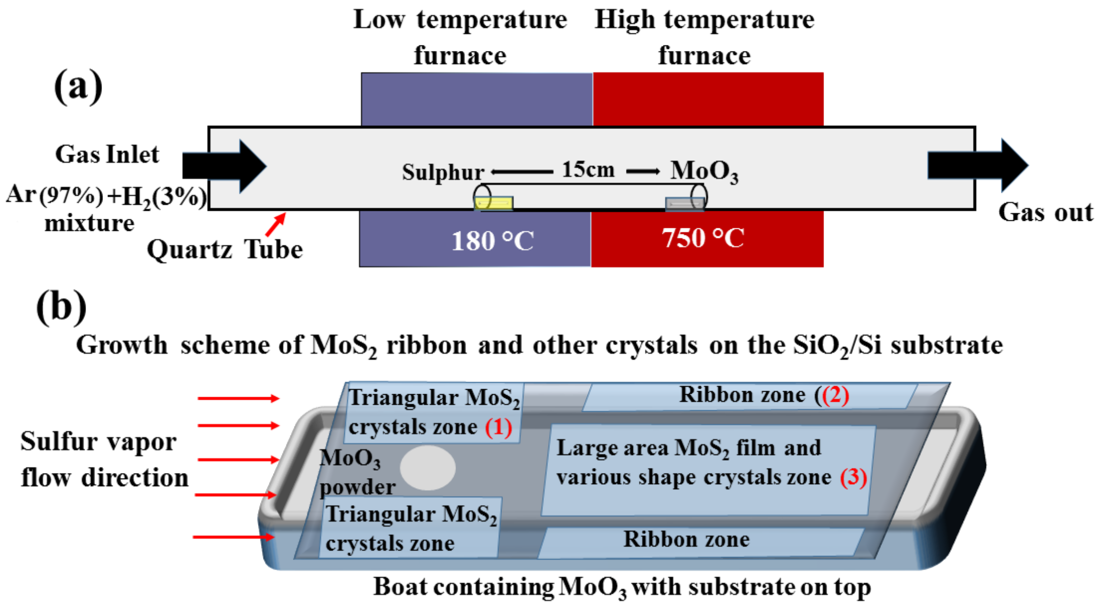

Figure 2-1(a) Schematic diagram of the CVD process for synthesis of MoS_2 ribbons and their branched structures (b) Growth scheme of MoS_2 ribbon and other crystals on SiO_2/Si substrate. Substrate was placed in face down manner to the center of the boat leaving small gap between head and tail of boat for passage of gas with sulfur vapor.

2.3 Results and discussion

The synthesis of monolayer ribbon structure was achieved by two individually controlled furnace CVD system as shown in Figure 1-1a. The sulfur and MoO_3 precursor were placed in a small quartz tube to provide proper channeling of sulfur vapor to react with evaporated MoO_3.The sulfur zone as well as MoO_3 zone was started at same time because, the heat dissipation to sulfur at low temperature zone is slow as compared to high temperature zone and the growth had to be carried out in sulfur rich atmosphere. Noticed the difference in morphology of MoS_2 crystals depending on the position of the substrate over the MoO_3 powder place on the substrate holder boat. The growth scheme of the MoS_2 ribbons and other crystals on the face down SiO_2/Si substrate in represented in Figure 2-1b. The MoS_2 ribbon growth was obtained at the out site of SiO_2/Si substrate, which was extended from the substrate holder boat. The diffusion of evaporated MoO_3 is relatively less to the outside of the boat, which creates a sulfur rich environment in the outside edges of the extended substrate.

2.3.1 Optical microscopy

The morphology of as synthesized material was characterized by optical microscopy. Figure 2-2a~ f presents optical microscope images of as synthesized MoS_2 ribbon structures on SiO_2/Si substrate. Figure 2-2a~b shows an overall view of the synthesized individual and various branched structure of the MoS_2 ribbons. The width and length of the synthesized ribbons are around 5-10 and 50-100 µm, respectively, where the width reduces from the nucleation point toward the end of the ribbons. Unidirectional and bi or tri-directional growth of ribbons from the nucleation point with an angle of 60°and 120° is obtained attributing to crystallographic growth orientation of MoS_2 crystals. I have also observed parallel secondary branching form the ribbons of a Y-shaped tri-directional ribbon. Figure 2-2c shows a much better image of multi-branching pattern of the MoS_2 ribbons. The parallel multi-branches from individual ribbon merged at some points (Figure 2.2b and Figure 2.2c), while abundant exposed edges can be observed in such MoS_2 multi-branched pattern. Figure 2-2d~e shows bidirectional ribbon structure forming V-shape with an angle of 120° and 60°. Figure 2-2f shows optical microscope image of triangular domains obtained at the zone 1 (Figure 2-1b). The formation of ribbons and other shapes of MoS_2 crystals depending on the sulfur and MoO_3 vapor exposure on the substrate. Very recently, Nie *et al*. has reported on first principles kinetic Monte Carlo studies revealing the influence of flux and the precursor stoichiometry, in which the triangular, fractal and dendritic WSe_2 monolayer domains can be obtained [43]. Thus, the precursor stoichiometry in the CVD process significantly influences on the growth of the MoS_2 ribbons.

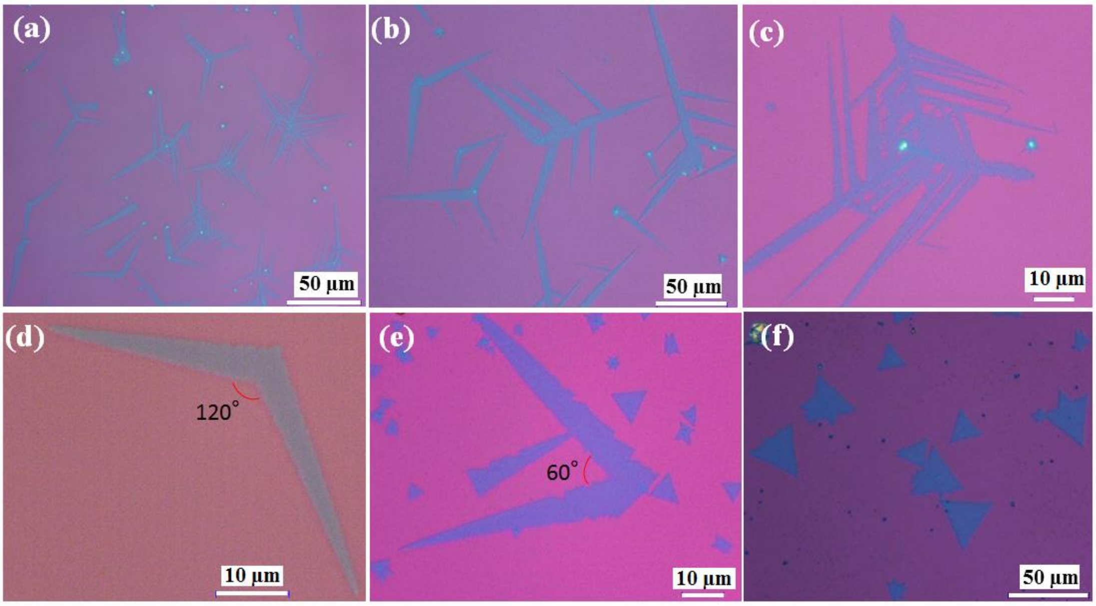

Figure 2-2 Optical microscopic images of (a) MoS_2 ribbon structures on SiO_2/Si substrate. (b) Presenting the various branching structures of the ribbon (blue ribbon structures). (c) Multi-branching pattern of the MoS_2 ribbons. (d) and (e) Bidirectional ribbon structure forming V-shape with an angle of 120° and 60°. (f) Formation of equilateral triangles at different position of the substrate.

2.3.2 Raman spectroscopy

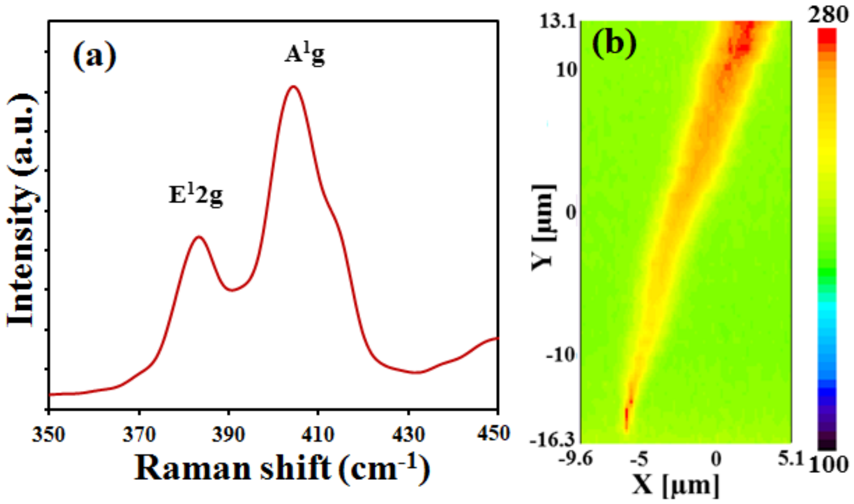

Figure 2-3 (a) Raman vibration modes E^1_{2g} (383.2 cm^{-1}) and A_{1g} (404.7 cm^{-1}). (b) Raman mapping image for the A_{1g} peak.

As explained in chapter 1, Raman spectroscopy is a versatile tool to identify and characterize the chemical and physical properties of synthesized materials. Figure 2-3a shows the characteristic Raman vibration modes E^1_{2g} and A_{1g} at 383.2 and 404.7 cm^{-1}, corresponding to in-plane vibration of molybdenum and sulfur atoms and out-of-plane vibration of sulfur atoms, respectively. The frequency difference of the two modes (383.2 and 404.7 cm^{-1}) is found to be 21 cm^{-1}. Raman mapping analysis was performed at the pointed end side of the MoS_2 ribbon as shown in Figure 2-3b. Almost, uniform thickness can be confirmed by spatial variation of magnitude of the A_{1g} and E_{2g} peaks. The structure of synthesized MoS_2 ribbons can be attributed to the semiconducting trigonal prismatic phase (2H phase MoS_2).

2.3.3 Field-emission scanning electron microscopy (FE-SEM)

FE-SEM images of the MoS_2 ribbons, branches and edge structures are shown in Figure 2-4a shows a low resolution FE-SEM image of the synthesized MoS_2 ribbons presenting the individual and various branched structures. Figure 2-4b shows FE-SEM image of the tri-directional MoS_2 ribbon with Y-shape with sharp end structure. Figure 2-4c shows a higher resolution FE-SEM image at the center of the Y-shape ribbon structure, where the growth of the three arm with 120° can be confirmed. The directional growth of the MoS_2 ribbons from the nucleation point is highly anisotropic. It has been reported that strong anisotropic, dendritic growth can be achieved with low concentration of precursors. In the CVD process, the directional growth of the MoS_2 ribbon is achieved in presence of very low concentration of molybdenum precursor at the outside of extended SiO_2/Si substrate. The crystal growth condition also can be related to diffusion-limited process, where the rate of crystal growth is dominated by the diffusion rate of the reactants [43], [44]. Figure 2-4d shows FE-SEM images of the synthesized MoS_2 crystals and merging of crystals to form large-area film at center zone of substrate (Figure 2-2b). Growth of triangular, six-lobed stars and other crystal shapes on the SiO_2/Si substrate at zone 3 (as shown in Figure 2.1b) was observed. As discussed earlier the growth of ribbon and triangular crystals significantly differ on the substrate surface depending on the exposer of MoO_3 and sulfur vapor. Figure 2-4e shows continuous growth and merging of the crystals to sub-millimeter scale. Similarly, Figure 2-4f shows millimeter scale continuous layer formation at the center zone of the substrate. However, as the location moves away from and outside the line of the MoO_3 powder, the ribbon structures are formed covering the large area between and outside the gap of silicon and the boat. These results clearly show the influence of the concentration gradient effect of evaporated MoO_3 over the substrate area.

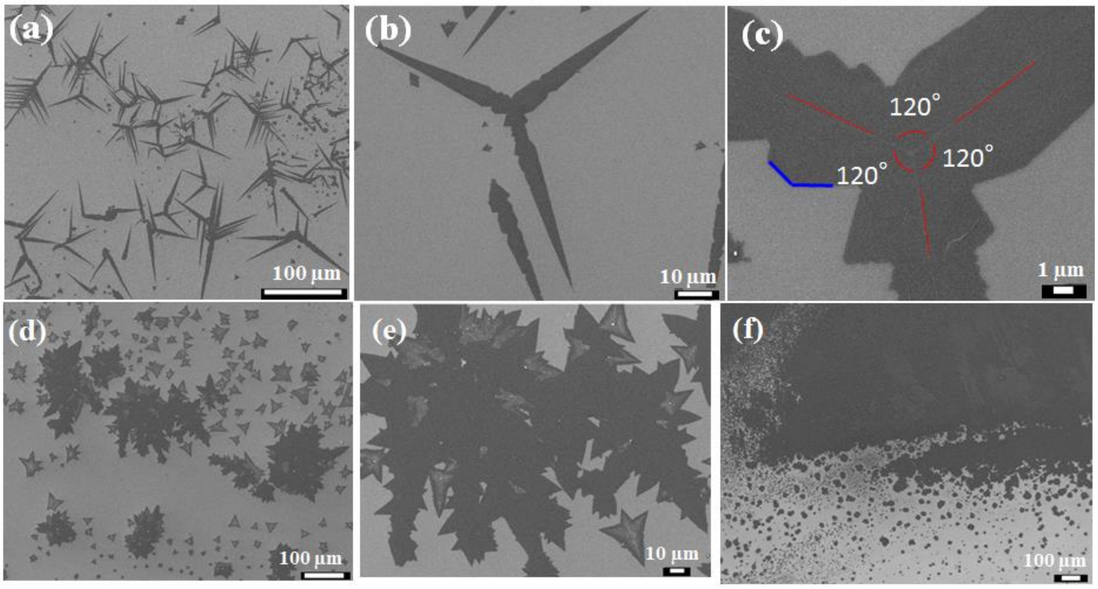

Figure 2-4 FE-SEM images of (a) of the synthesized MoS_2 ribbons presenting the individual and various branched structures. (b) Tri-directional MoS_2 ribbon with Y-shape. (c) Higher resolution image at the center of the Y-shape ribbon structure, where the growth of the three arm with 120°. (d) MoS_2 crystals and (e) their merged structure to form large-area film at center zone of substrate. (f) Continuous growth and merging of the crystals to millimeter scale.

The highly anisotropic growth of MoS_2 ribbons and their particular branched structures can be achieved with exposer of low concentration of precursors, which strongly relates to the surface diffusion limited process. Figure 2-5a shows FE-SEM image of a bidirectional MoS_2 ribbon presenting uneven edge structure. Similarly, most of the obtained individual and branched ribbons possess uneven abundant edge structures, where the edges are formed with angles of 60° and 120°, indicating variation in molybdenum and sulfur edge terminations.

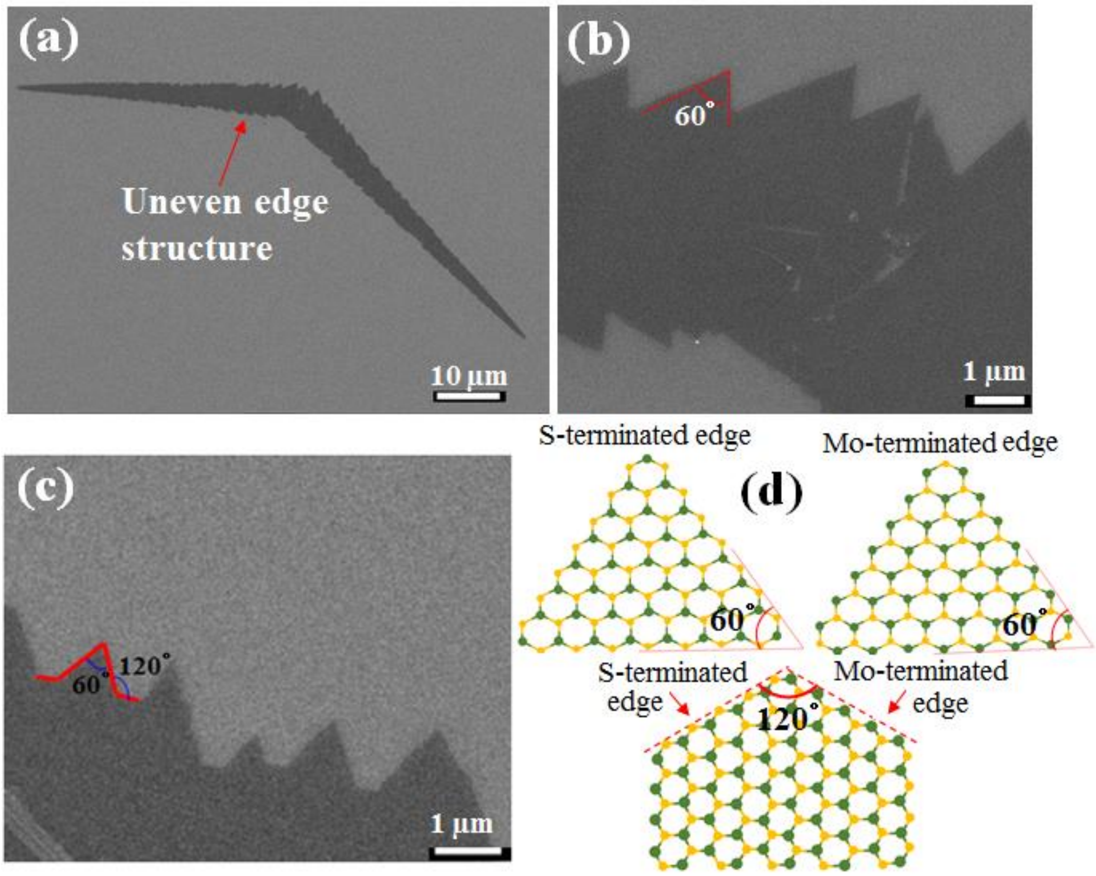

Figure 2-5 FE-SEM images of (a) bidirectional MoS$_2$ ribbon presenting uneven edge structure, (b) and (c) edge structures of the MoS$_2$ ribbon creating 60° and 120° angles. (d) Schematic view of the possible edge termination with molybdenum (M) or sulfur (S) atoms to form 60° and 120° edges.

Figure 2-5b shows that the both side of MoS$_2$ ribbons consisting with sharp uneven edge structure, where the edges are pointed at an angle of 60°. The edges with an angle of 60° should be molybdenum or sulfur terminated edges as presented in the schematic Figure 2-5d. However, it is not the case for all the ribbon edges as can be observed from Figure 2-5c. The edge with 120° angles are not sharply pointed attributing to the variation in edge terminations. Figure 2-5c shows an interesting prospect of the molybdenum and sulfur edge terminations. The sharp tip at the edge forms 60° angle, while at the base of the tip it is 120° angle, indicating presence of both molybdenum and sulfur terminated zigzag edges (schematic view in Figure 2-5d). Simultaneous addition of molybdenum and sulfur atoms at the edge of the MoS_2 ribbon enable formation of such defined edge structures. This also confirms presence of both molybdenum and sulfur exposed edge terminations. Recently, plasma etching and hydrogen annealing of monolayer triangular crystals have been reported to obtain large amount of edges for catalytic application [26]. In our demonstrated process, branched MoS_2 ribbon structures can be synthesized with abundant of active edges without any post processing. Furthermore, controlling the edges of such MoS_2 ribbon structure can be critical to observe novel electronic properties. Thus, I have demonstrated a method for directional growth of MoS_2 ribbons forming various branched shapes (V and Y shapes) with particular edge terminations (S and Mo) in sulfur enriched conditions.

2.3.4 Atomic force microscopy (AFM)

Figure 2-6a shows an AFM of the as-synthesized MoS_2 ribbon on SiO_2/Si substrate. Line profile at the edge presents an approximate thickness of around ~0.7 nm, corresponding to a monolayer ribbon.

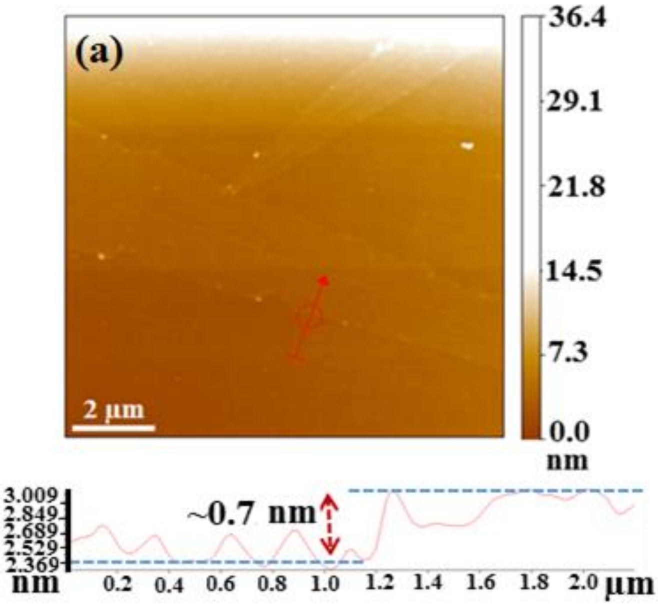

Figure 2-6(a) AFM image of the as-synthesized MoS_2 ribbon on SiO_2/Si substrate marked by red arrow.

2.3.5 Photoluminescence (PL) spectroscopy

I have explored the PL properties of the MoS_2 ribbons comparing with the triangular crystals. PL measurements were carried out with an excitation wavelength of ~532 nm at room temperature. Figure 2-7a-b show the PL spectra and mapping image for the equilateral triangular shaped MoS_2 crystals. A strong PL signal is observed at ~700 nm corresponding to A_1 excitation peak, owing to direct band gap nature of MoS_2 monolayer [16]–[18]. The PL mapping analysis shows almost uniform response from the equilateral triangular crystal.

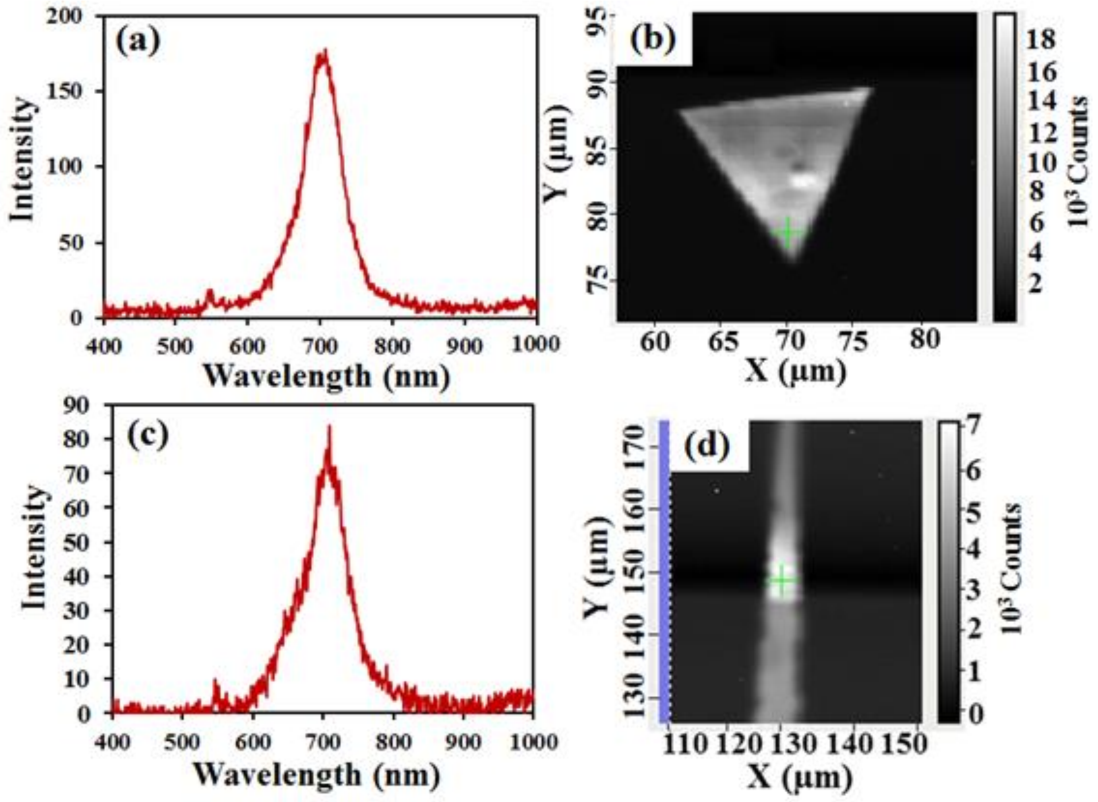

Figure 2-7(a) PL spectra and (b) mapping image for an equilateral triangular shaped MoS_2 crystal obtained along with the ribbons as discussed in OM and SEM image. (c) PL spectra and (d) mapping image of the MoS_2 ribbon.

Similarly, Figure 2-7c and d show PL spectra and mapping image for the MoS_2 ribbon. The PL exaction peak is observed at ~700 nm, like the MoS_2 monolayer triangular crystals. However, The PL spectral intensity of the ribbon structure was significantly less than that of the triangular crystal. This may be due to different edge structure of the triangular crystals and ribbons. The equilateral triangular crystals with smooth edges are either sulfur or molybdenum terminated whereas the ribbon edges are uneven attributing difference in edge termination atoms. Considering the above results, details of the edge structures of the synthesized MoS_2 ribbons are studied.

2.3.6 X-ray photoelectron spectroscopy (XPS)

X-Ray photoelectron spectroscopy is used to study elemental composition of the ribbons. Figure 2-8a shows deconvoluted XPS core-level spectra of Mo 4f peak, confirming the chemical state doublet Mo $4f_{7/2}$ (230.1 eV) and Mo $4f_{5/2}$ (233.3 eV) peaks.

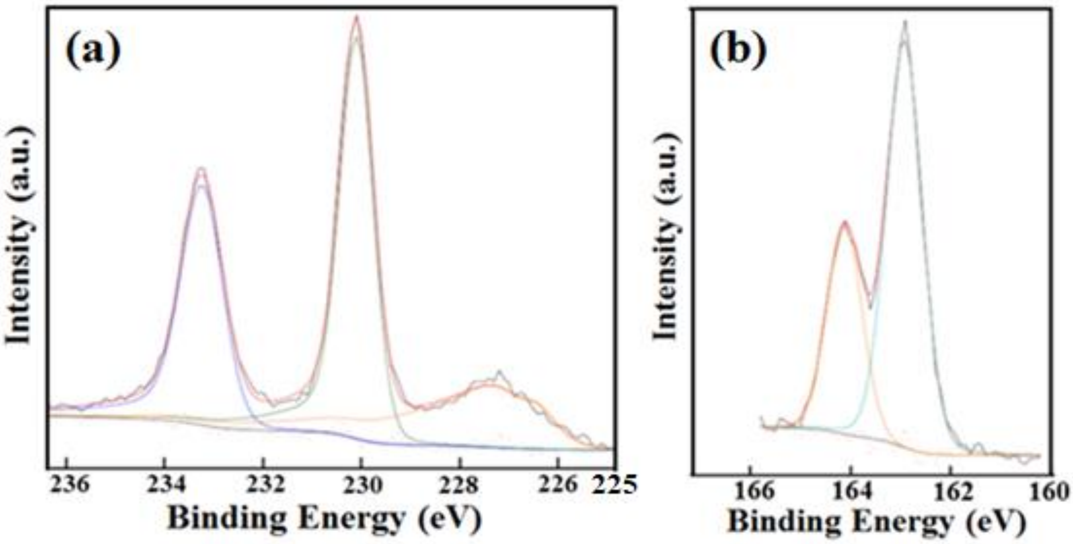

Figure 2-8 (a) Deconvoluted XPS core-level spectra of Mo 4f peak, confirming the chemical state doublet Mo $4f_{7/2}$ (230.1 eV) and Mo $4f_{5/2}$ (233.3 eV) peaks. (b) Deconvoluted XPS S $2p_{3/2}$ (~162.4 eV) and $S2p_{1/2}$ (~163.5 eV) peaks.

Similarly, Figure 2-8b shows deconvoluted XPS spectra of S2p peak for the synthesized WS_2 sheets SiO_2/Si substrate. The S $2p_{3/2}$ and S $2p_{1/2}$ peaks are confirmed at ~162.4 and ~ 163.5 eV, as expected for the WS_2 layers. The XPS analysis confirms that the synthesized MoS_2 ribbons are free from any other impurities and oxide formations.

2.4 Conclusions

In this chapter, the synthesis of monolayer MoS_2 ribbons and their branched structures by the CVD method in sulfur enriched condition and low exposure of evaporated MoO_3 is demonstrated along with triangular crystals and layer structures. The detailed investigation of ribbon structures showed formation of unidirectional and bi (V-shape with 60° and 120°) or tri-directional (Y-shape with 120°) MoS_2 ribbons and their other branched structures in the developed CVD process. The growth of the MoS_2 ribbons, triangular and other crystals significantly depend on the exposure of sulfur and concentration of MoO_3 vapor on the SiO_2/Si substrate surface. The width and length of the synthesized ribbons were around 5-10 and 50-100 µm, respectively, where the width reduces from the nucleation point toward the end of the ribbon. The individual and branched ribbons are formed with uneven edge structures, where the edges were found to be with 60° and 120°, indicating variation in molybdenum and sulfur zigzag edge terminations. The directional growth of MoS_2 ribbons with defined edge structures in particular CVD conditions can open up new possibilities for catalysis and electrochemical applications.

As explained earlier, the MoS_2 ribbons showed uneven edge with both Mo and S terminations, in contrast to the smooth edges of triangular crystals meaning less stability among the other shapes with less edge structures. Since, the ribbon structures possess high edge density and relatively low PL, their use may be limited to catalysis or electrochemical applications. Whereas the triangular and large area films can be utilized for fabrication of optoelectronic devices owing to better PL and atmospheric stability compared to ribbon structures.

In progress of CVD synthesis of MoS_2 and WS_2 layers, some kind of degradation with environmental exposure was observed. Hence, detailed degradation and stability studies were planned and performed as discussed in the following chapter.

2.5 References

[1] B. Radisavljevic, A. Radenovic, J. Brivio, V. Giacometti, and A. Kis, “Single-layer MoS_2 transistors,” *Nat. Nanotechnol.*, vol. 6, no. 3, pp. 147–150, Mar. 2011.

[2] K. F. Mak, K. He, J. Shan, and T. F. Heinz, “Control of valley polarization in

monolayer MoS_2 by optical helicity," *Nat. Nanotechnol.*, vol. 7, no. 8, pp. 494–498, 2012.

[3] Q. H. Wang, K. Kalantar-Zadeh, A. Kis, J. N. Coleman, and M. S. Strano, "Electronics and optoelectronics of two-dimensional transition metal dichalcogenides," *Nat. Nanotechnol.*, vol. 7, no. 11, pp. 699–712, 2012.

[4] A. Pospischil, M. M. Furchi, and T. Mueller, "Solar-energy conversion and light emission in an atomic monolayer p-n diode," *Nat. Nanotechnol.*, vol. 9, no. 4, pp. 257–261, 2014.

[5] J. Kibsgaard, Z. Chen, B. N. Reinecke, and T. F. Jaramillo, "Engineering the surface structure of MoS_2 to Â preferentially expose active edge sites for Â electrocatalysis," *Nat. Mater.*, vol. 11, no. 11, pp. 963–969, 2012.

[6] D. Voiry *et al.*, "Enhanced catalytic activity in strained chemically exfoliated WS_2 nanosheets for hydrogen evolution," *Nat. Mater.*, vol. 12, no. 9, pp. 850–855, Sep. 2013.

[7] D. Voiry *et al.*, "Enhanced catalytic activity in strained chemically exfoliated WS_2 nanosheets for hydrogen evolution," *Nat. Mater.*, vol. 12, no. 9, pp. 850–855, Sep. 2013.

[8] A. Splendiani *et al.*, "Emerging photoluminescence in monolayer MoS_2," *Nano Lett.*, vol. 10, no. 4, pp. 1271–1275, Apr. 2010.

[9] K. F. Mak, C. Lee, J. Hone, J. Shan, and T. F. Heinz, "Atomically thin MoS_2: A new direct-gap semiconductor," *Phys. Rev. Lett.*, vol. 105, no. 13, p. 136805, 2010.

[10] D. Xiao, G. Bin Liu, W. Feng, X. Xu, and W. Yao, "Coupled spin and valley physics in monolayers of MoS_2 and other group-VI dichalcogenides," *Phys. Rev. Lett.*, vol. 108, no. 19, pp. 1–5, 2012.

[11] S. Wu *et al.*, "Electrical tuning of valley magnetic moment through symmetry control in bilayer MoS_2," *Nat. Phys.*, vol. 9, no. 3, pp. 149–153, 2013.

[12] L. Britnell *et al.*, "Strong light-matter interactions in heterostructures of atomically thin films," *Science (80-.).*, vol. 340, no. 6138, pp. 1311–1314, 2013.

[13] H. Li *et al.*, "Fabrication of single- and multilayer MoS_2 film-based field-effect transistors for sensing NO at room temperature," *Small*, vol. 8, no. 1, pp. 63–67, 2012.

[14] M. Fontana *et al.*, "Electron-hole transport and photovoltaic effect in gated MoS2schottky junctions," *Sci. Rep.*, vol. 3, pp. 8–13, 2013.

[15] D. Kong, J. J. Cha, H. Wang, H. R. Lee, and Y. Cui, "First-row transition metal dichalcogenide catalysts for hydrogen evolution reaction," *Energy Environ. Sci.*, vol. 6, no. 12, p. 3553, 2013.

[16] Z. Yin *et al.*, “Single-layer MoS_2 phototransistors,” *ACS Nano*, vol. 6, no. 1, pp. 74–80, 2012.

[17] S. M. Shinde, G. Kalita, and M. Tanemura, “Fabrication of poly(methyl methacrylate)-MoS_2/graphene heterostructure for memory device application,” *J. Appl. Phys.*, vol. 116, no. 21, 2014.

[18] Y. Huang, J. Guo, Y. Kang, Y. Ai, and C. M. Li, “Two dimensional atomically thin MoS_2 nanosheets and their sensing applications,” *Nanoscale*, vol. 7, no. 46, pp. 19358–19376, 2015.

[19] E. Singh, K. S. Kim, G. Y. Yeom, and H. S. Nalwa, “Atomically thin-layered molybdenum disulfide (MoS_2) for bulk-heterojunction solar cells,” *ACS Appl. Mater. Interfaces*, vol. 9, no. 4, pp. 3223–3245, 2017.

[20] G. Eda, H. Yamaguchi, D. Voiry, T. Fujita, M. Chen, and M. Chhowalla, “Photoluminescence from chemically exfoliated MoS_2,” *Nano Lett.*, vol. 11, no. 12, pp. 5111–5116, 2011.

[21] A. K. Geim and I. V. Grigorieva, “Van der Waals heterostructures,” *Nature*, vol. 499, no. 7459, pp. 419–425, 2013.

[22] Y. Gong *et al.*, “Vertical and in-plane heterostructures from WS_2/MoS_2 monolayers,” *Nat. Mater.*, vol. 13, no. 12, pp. 1135–1142, 2014.

[23] M.-Y. Li *et al.*, “Epitaxial growth of a monolayer WSe_2-MoS_2 lateral p-n junction with an atomically sharp interface,” *Science (80).*, vol. 349, no. 6247, pp. 524–528, 2015.

[24] J. M. Woods *et al.*, “One-Step Synthesis of MoS_2/WS_2 Layered Heterostructures and Catalytic Activity of Defective Transition Metal Dichalcogenide Films,” *ACS Nano*, vol. 10, no. 2, pp. 2004–2009, 2016.

[25] K. Roy *et al.*, “Graphene–MoS_2 hybrid structures for multifunctional photoresponsive memory devices,” *Nat. Nanotechnol.*, vol. 8, no. 11, pp. 826–830, Nov. 2013.

[26] G. Ye *et al.*, “Defects Engineered Monolayer MoS_2 for Improved Hydrogen Evolution Reaction,” *Nano Lett.*, vol. 16, no. 2, pp. 1097–1103, 2016.

[27] Z. Zeng *et al.*, “Single-layer semiconducting nanosheets: High-yield preparation and device fabrication,” *Angew. Chemie - Int. Ed.*, vol. 50, no. 47, pp. 11093–11097, 2011.

[28] A. M. Van Der Zande *et al.*, “Grains and grain boundaries in highly crystalline monolayer molybdenum disulphide,” *Nat. Mater.*, vol. 12, no. 6, pp. 554–561, 2013.

[29] K. G. Zhou, N. N. Mao, H. X. Wang, Y. Peng, and H. L. Zhang, “A mixed-solvent

strategy for efficient exfoliation of inorganic graphene analogues," *Angew. Chemie - Int. Ed.*, vol. 50, no. 46, pp. 10839–10842, 2011.

[30] Q. Ji, Y. Zhang, Y. Zhang, and Z. Liu, "Chemical vapour deposition of group-VIB metal dichalcogenide monolayers: engineered substrates from amorphous to single crystalline," *Chem. Soc. Rev.*, vol. 44, no. 9, pp. 2587–2602, 2015.

[31] C. Muratore *et al.*, "Continuous ultra-thin MoS_2 films grown by low-temperature physical vapor deposition," *Appl. Phys. Lett.*, vol. 104, no. 26, p. 261604, Jun. 2014.

[32] S. Wu, C. Huang, G. Aivazian, J. S. Ross, D. H. Cobden, and X. Xu, "Vapor-solid growth of high optical quality MoS_2 monolayers with near-unity valley polarization," *ACS Nano*, vol. 7, no. 3, pp. 2768–2772, 2013.

[33] Y. Gao *et al.*, "Large-area synthesis of high-quality and uniform monolayer WS2on reusable Au foils," *Nat. Commun.*, vol. 6, p. 8569, 2015.

[34] Y.-H. Lee *et al.*, "Synthesis of Large-Area MoS_2 Atomic Layers with Chemical Vapor Deposition," Feb. 2012.

[35] Y. Zhan, Z. Liu, S. Najmaei, P. M. Ajayan, and J. Lou, "Large-area vapor-phase growth and characterization of MoS_2 atomic layers on a SiO_2 substrate," *Small*, vol. 8, no. 7, pp. 966–971, 2012.

[36] Y. Shi *et al.*, "van der Waals Epitaxy of MoS_2 Layers Using Graphene As Growth Templates," *Nano Lett.*, vol. 12, no. 6, pp. 2784–2791, 2012.

[37] S. Wang *et al.*, "Shape Evolution of Monolayer MoS_2 Crystals Grown by Chemical Vapor Deposition," *Chem. Mater.*, vol. 26, pp. 6371–6379, 2014.

[38] S. L. Shang, G. Lindwall, Y. Wang, J. M. Redwing, T. Anderson, and Z. K. Liu, "Lateral Versus Vertical Growth of Two-Dimensional Layered Transition-Metal Dichalcogenides: Thermodynamic Insight into MoS_2," *Nano Lett.*, vol. 16, no. 9, pp. 5742–5750, 2016.

[39] Y. Li, Z. Zhou, S. Zhang, and Z. Chen, "MoS_2 nanoribbons: High stability and unusual electronic and magnetic properties," *J. Am. Chem. Soc.*, vol. 130, no. 49, pp. 16739–16744, 2008.

[40] H. Pan and Y.-W. Zhang, "Edge-dependent structural, electronic and magnetic properties of MoS_2 nanoribbons," *J. Mater. Chem.*, vol. 22, no. 15, p. 7280, 2012.

[41] H. Xu *et al.*, "Controllable Synthesis of 2D and 1D MoS_2 Nanostructures on Au Surface," *Adv. Funct. Mater.*, vol. 27, no. 19, p. 1603887, May 2017.

[42] Y. Nie *et al.*, "First principles kinetic Monte Carlo study on the growth patterns of WSe_2 monolayer," *2D Mater.*, vol. 3, no. 2, p. 025029, 2016.

[43] D. H. Jung, C. Kang, J. E. Nam, H. Jeong, and J. S. Lee, "Surface Diffusion Directed Growth of Anisotropic Graphene Domains on Different Copper Lattices,"

Sci. Rep., vol. 6, no. January, pp. 1–7, 2016.

[44] J. Lee, S. W. Kim, I. Kim, D. Seo, and H. J. Choi, “Growth of Silicon Nanosheets Under Diffusion-Limited Aggregation Environments,” *Nanoscale Res. Lett.*, vol. 10, no. 1, pp. 2–7, 2015.

CHAPTER 3

3. Degradation and Encapsulation Study of 2D-TMDCs

3.1 Atmospheric degradation in WS_2 crystals

3.1.1 Introduction

After CVD synthesis, understanding the structural stability of transition metal dichalcogenides (TMDCs) layers under ambient condition is significant for device engineering. Earlier studies have revealed the degradation of TMDCs layer under extreme conditions, such as temperatures above 250 °C and combined exposure to UV, heat, and moisture [1], [2]. Most importantly, Gao *et al*., has reported degradation of MoS_2 and WS_2 layers under long duration atmospheric exposure at room temperature [3]. He *et al*., has also investigated the oxidation induced degradation of monolayer WS_2 caused by exposure to ambient condition [4]. Similarly, Mirabelli *et al*. has reported on air sensitivity of exfoliated TMDCs layers [5]. In this context, before using these materials for device fabrication, it is imperative to study the dilapidation mechanism as well as protective methods for long term stability. Accordingly, in this chapter detailed investigation of atmospheric degradation and subsequent encapsulation study for long term stability has been compiled. The occurrence of regular degradation patterns in CVD synthesized individual WS_2 crystals on SiO_2/Si substrate with long-term uncontrolled atmospheric exposure has been studied. Remarkable structural transformation features were observed with atmospheric oxidation owing to reaction along particular edge termination of WS_2 crystals. Understanding the degradation and structural transformation process of the CVD synthesized TMDCs layered materials can be a significant aspect for designing a stable and high performance nanoelectronics and optoelectronics devices. This chapter includes details of the transformed features of CVD synthesized WS_2 crystals with exposure to ambient conditions. Also, dry encapsulation process for MoS_2 and WS_2 layers with a fluorocarbon as well as carbonaceous layer by simple thermal evaporation and by microwave assisted surface wave plasma deposition to prevent oxidation is described in detail.

3.1.2 Materials and method

The synthesis of MoS_2 was performed as explained in chapter 2 with slight modification of growth parameters. The synthesis process for WS_2 crystals is explained as follows. WS_2 crystals were synthesized by CVD method on cleaned 100 nm SiO_2 coated Si substrate by a seed-assisted technique as presented in Figure 3-1. Two individually controlled quartz tube furnaces with only Ar flowing at atmospheric pressure. Before the CVD growth, the substrate was dipped into a WO_3 isopropyl alcohol (IPA) solution (concentration: 1 mg WO_3 powder in 30 ml of IPA). The particles deposited on the substrate serve as nuclei seeds to help the crystal growth. Sulphur powder (200 mg) was positioned in the low-temperature furnace sublimating at 110 °C, whereas WO_3 powder (50 mg) was heated at 950 °C in the high-temperature furnace. The seeded substrate was placed face-down above the WO_3 powder.

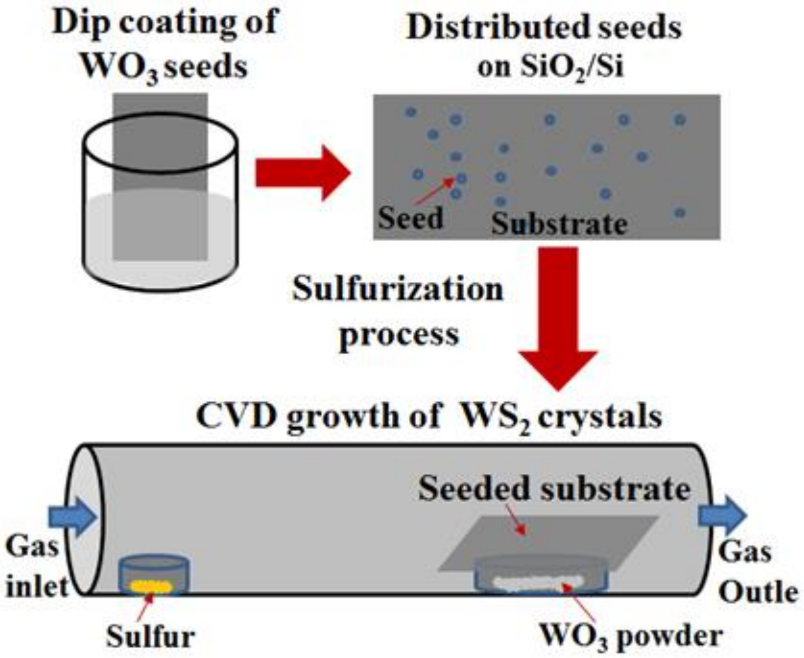

Figure 3-1 Schematic of the seed-assisted growth process for triangular, hexagonal and other shaped WS_2 crystals.

Subsequently, the high temperature furnace was raised to ~950 °C, without starting the low temperature furnace. The growth was carried out for 40 min at 950 °C. Ultra-high purity Ar (99.9999%) gas was introduced in the growth furnace with a flow rate of 100 standard cubic centimeter per minute (sccm) during the complete growth process. After growth, the furnace was normally cooled to room temperature. The synthesized samples were kept in atmospheric pressure, temperature and humidity without controlling any parameters. The samples were characterized; 1) immediately after synthesis and 2) exposing to ambient conditions for different durations (3, 12 and 15 months). Teflon thin film was deposited by thermal evaporation technique using ULVAC VPC-260F.

3.1.3 Results and Discussion

The sample was characterized immediately after synthesis by FE-SEM analysis to investigate the morphology of WS_2 crystals. Figure 3-2a-c shows FE-SEM images of different shapes of WS_2 crystal obtained by the seed-assisted synthesis process. Figure 3-2a shows an equilateral triangular WS_2 crystal with a lateral size around 90 μm. Similarly, truncated triangular and hexagonal WS_2 crystals were obtained in the same growth process as shown in Figure 3-2b-c, respectively. The growth of such hexagonal, equilateral and truncated triangular crystals in a seed-assisted technique has been demonstrated in many of the previous studies [6], [7]. In the synthesis process, we also obtained WS_2 crystals with various other shapes and layered structures as confirmed by FE-SEM analysis.

We observed significant structural transformation of the synthesized WS_2 crystals with exposure to ambient environment for long duration. Previously, He *et al.* has reported that the PL and Raman spectra of WS_2 layer remained unchanged with short-term atmospheric exposure [4]. However, significant structural transformation features of the WS_2 crystals were observed after one year (12 months) of ambient exposure. Figure 3-2d shows FE-SEM image of a truncated WS_2 crystal after 12 months of exposure at ambient conditions. Oxidation of sample occurred in ambient atmosphere forming a triangular shape in the crystal, where other oxidized defects also appeared within the triangle. This may be due to fact that faster oxygen reaction process occurs along the unsaturated growth front of the uneven edges. Further, we analyzed the hexagonal crystals with smooth edges (upto nm scale) to obtain better information of the degradation process. Figure 3-2e shows the degradation pattern inside the hexagonal WS_2 crystal after long duration atmospheric exposure. We observed appearance of many white spots throughout the crystal, which were not observed in the FE-SEM images of fresh samples (Figure 3-2c). These features were further analyzed for better understanding. Figure 3-2f shows high resolution FE-SEM image of a selected area in Figure 3-2e. It is observed that the degradation propagates in different directions forming an angle of 120°, corresponding to oxidation along the crystallographic direction, such patterns are observed at various part of the hexagonal crystal.

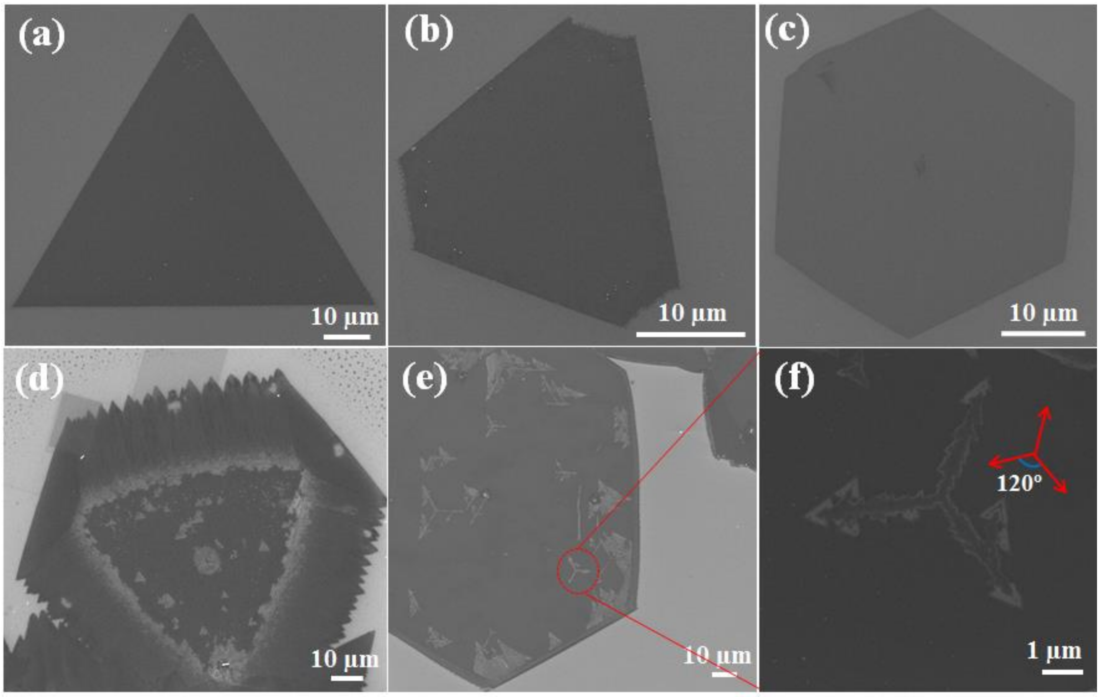

Figure 3-2 FE-SEM images of as-synthesized (a) equilateral triangular, (b) truncated triangular and (c) hexagonal shaped WS_2 crystal. Structural transformation feature of (d) truncated WS_2 crystal, (e) hexagonal shaped WS_2 crystal and (f) high resolution image of degradation pattern inside the hexagonal crystal.

The degradation pattern and structural transformation of the equilateral triangular crystals with exposure to ambient condition is also quite interesting as explained below. Figure 3-3 a shows FE-SEM images of oppositely orientated two triangular WS_2 crystals immediately after synthesis. No significant structural defects or etching features were observed inside the equilateral triangle immediately after synthesis. However, new features appeared inside the individual triangle after exposure to ambient condition for 12 months (Figure 3-3b). Formation of small equilateral triangles in the triangular crystals were observed as presented in the Figure 3-3 b. Interestingly, orientation of all the small triangles is same and opposite of the original WS_2 crystal. Figure 3-3c shows an FE-SEM image with clear view of the oppositely orientated small triangles formed at the center and at the edges, where some of the triangles were overlapped. Such type of regular degradation features of WS_2 crystals with exposure to ambient conditions has not been revealed in the previous studies. It is believed that these features appear due to reaction with oxygen along a particular edge termination of the equilateral triangular WS_2 single crystals as well as basal plane. Figure 3-3d shows schematic of tungsten and sulfur terminated WS_2 triangular crystals with possible edge termination of the oppositely orientated small triangles inside the individual crystal. Previous report suggests that the

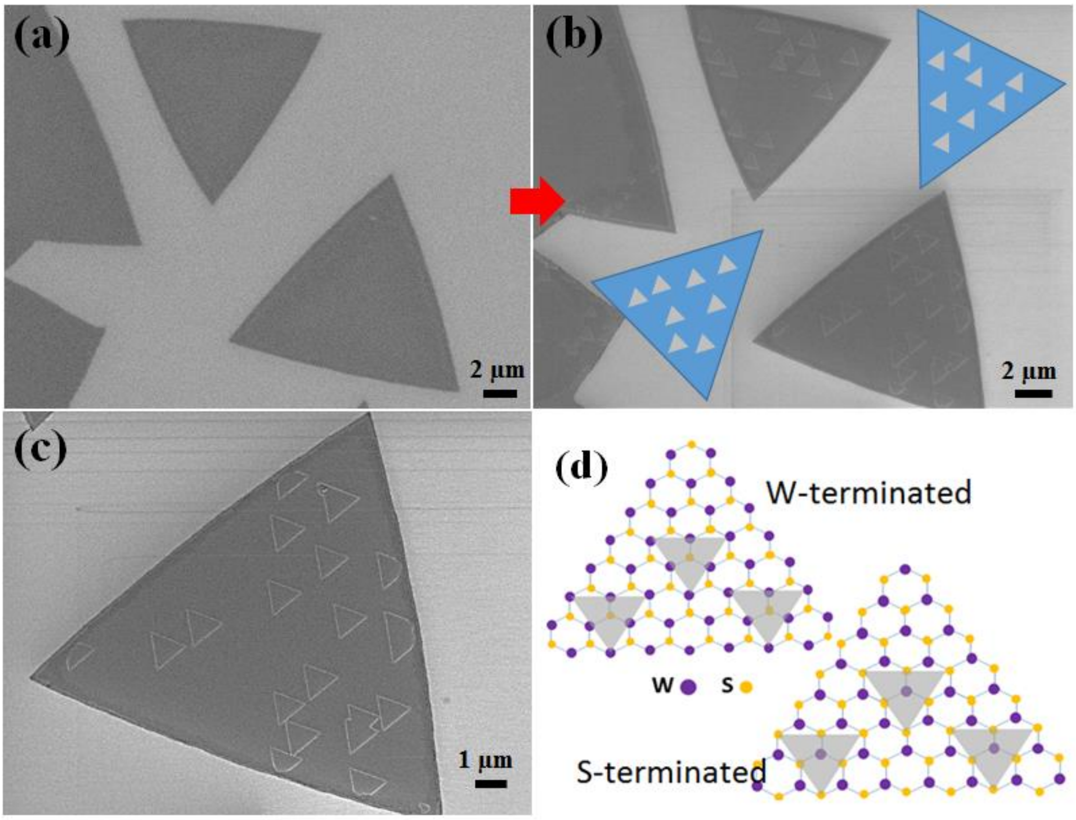

Figure 3-3 FE-SEM images of (a) oppositely orientated two triangular WS_2 crystals immediately after synthesis and (b) after exposing to ambient conditions for 12 months, formation of small equilateral triangles in the triangular crystals is observed as presented in the inset of the figure (c) high resolution image of oppositely orientated equilateral triangles formation inside the triangular WS_2 crystal. (d) Schematic of the tungsten (W) and sulfur (S) terminated WS_2 triangular crystals with possible edge termination of the oppositely orientated small triangles in the individual crystal

molybdenum zigzag (Mo-ZZ) and Sulphur zigzag (S-ZZ) edge terminations are commonly observed in triangular MoS_2 nanocrystals [8]. Considering the possible tungsten or sulfur edge terminations of the synthesized WS_2 crystals, the oppositely orientated small triangle inside the crystal may possess particular edge terminations (metal or S edge depending on crystal structure). Previously, Zhou *et al*. has demonstrated triangular pits formation in MoS_2 layer by heating in atmosphere [9]. The triangular etched pits originated with anisotropic oxidation of the MoS_2 edges and expand due to chemical oxidation of its edges, where the molybdenum and sulfur atoms become MoO_3 and SO_2 gas molecules [9]. It has been also reported that the pit edges should be ZZ since the MoS_2 layer typically exposes along ZZ edges [10]. Now, considering the triangular WS_2 crystals with either sulfur or tungsten terminated edges, the inner degraded triangle may possess either sulfur or tungsten terminated edges depending on the orientation. The appeared small triangles are oppositely orientated to the original WS_2 crystals, in this context the edge termination of the original and degraded patterns should be same.

The structural degradation process is further analyzed by the XPS and AES analysis at room temperature for the sample exposed at ambient conditions. Figure 3-4a shows W 4f peak for fresh and long duration exposed WS_2 samples. A chemical shift of around 0.2 eV of the W 4f peak is observed for the degraded WS_2 sample, corresponding to atmospheric oxidation. Figure 3-4b shows deconvoluted XPS core-level spectra with chemical state doublet W 4f peaks ($W4f_{7/2}$ at and $W4f_{5/2}$). Besides the W-S bonding state additional peak is observed at around 36.8 and 38.3 eV, corresponding to the oxide state (W-O) as discussed in previous report [3]. The oxidized tungsten was estimated to be around 25% from the peak area of the deconvoluted W4f XPS spectra (Figure 3-4b). The XPS analysis shows a W: S ratio of ~1:1.52 (±0.2) for the long duration exposed sample, which implies significant sulfur loss compared to original crystal W:S~ 1:2 (±0.2). The XPS results present chemical state of overall WS_2 crystals on the substrate. AES analysis was performed at selective positions to obtain better information of the degraded patterns in individual crystal. Figure 3-4c shows SEM image of a triangular WS_2 crystal, where selective AES analysis is performed at position 1, 2 and 3. Figure 3-4d shows AES spectra at the three different positions, presenting the peaks for sulfur, tungsten, carbon and oxygen.

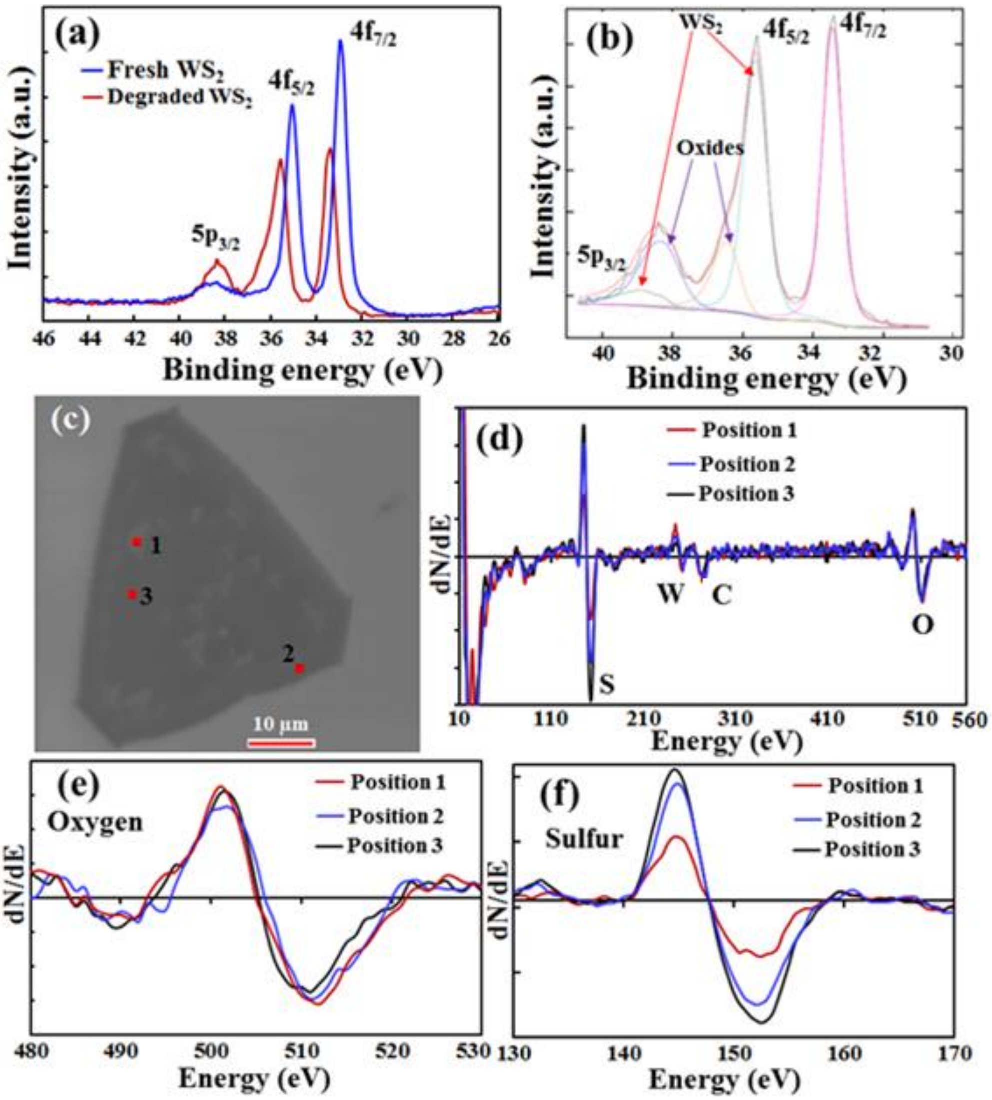

Figure 3-4 XPS spectra of (a) W 4f peak for fresh and long duration exposure in atmospheric conditions WS_2 samples. (b) De-convoluted W 4f peak for WS_2 crystals with long duration exposure in atmospheric conditions. (c) SEM image of a triangular WS_2 crystal, where selective AES analysis is performed. (d) AES spectra at three different position (1, 2 and 3) presenting the peaks for sulfur, tungsten, carbon and oxygen. Individual (e) oxygen and (f) sulfur peaks analysis at position 1, 2 and 3.

Other elements are not detected in the XPS and AES analysis, however there is possibility of additional impurities as reported previously by Addou *et al*. [11] We analyzed the AES oxygen and sulfur peaks individually at different positions within the same WS_2 crystal as shown in Figure 3-4e-f. Small shift in peak positions for the AES oxygen peak at the degraded area (position 1) was observed. We expect that the AES oxygen peak intensity only does not provide clear information of oxidation and degradation of the extremely thin WS_2 layer (~0.62 nm) on SiO_2/Si substrate in presence of other chemi-absorb or oxygen functional groups. Figure 3-4f shows AES spectra for sulfur at positions 1, 2 and 3 of the SEM images. The sulfur peak visibly differs at the three points of the same triangular crystal. The sulfur peak intensity is significantly reduced at the degraded area at position 1 of SEM image (Figure 3-4c). The significant difference in shape and intensity of the sulfur peak indicates change in W-S chemical bonding, which is consistent with the XPS analysis. These studies clearly indicate structural degradation of the hexagonal, equilateral and truncated triangular crystals with long duration atmospheric exposure.

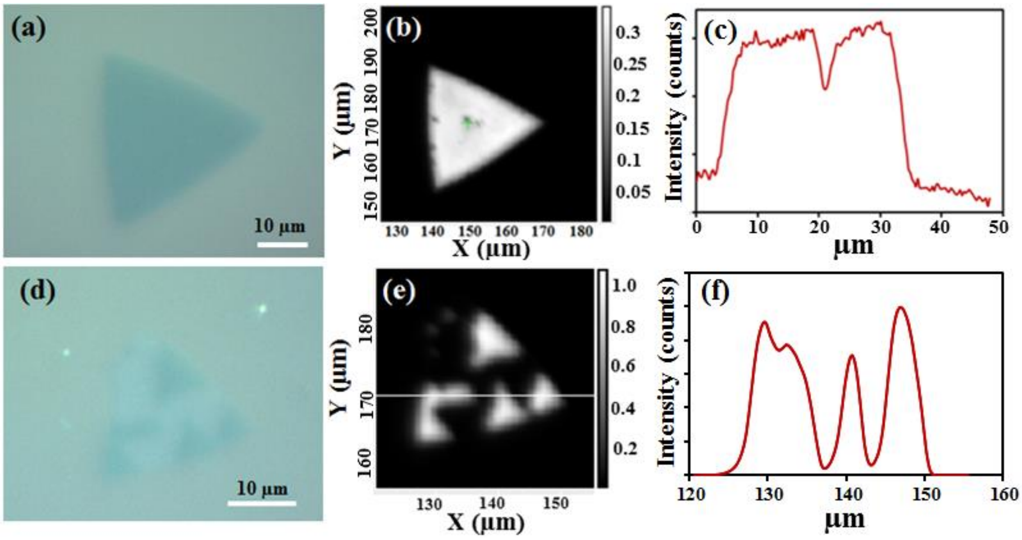

Figure 3-5(a) Optical microscopy image of a triangular WS_2 crystal immediately after synthesis. (b) PL mapping and (c) intensity profile analysis of the WS_2 crystal. (d) Optical microscope image of a highly degraded triangle after 15 months of exposure to atmosphere. (e) PL mapping and (f) intensity profile of the degraded WS_2 crystal.

PL properties of the as-synthesized and degraded WS_2 crystals were compared. Figure 3-5a shows optical microscope image of as-synthesized triangular WS_2 crystal for which PL mapping analysis is performed. PL measurement was carried out with an excitation wavelength of ~532 nm at room temperature. Figure 3-5b shows the PL mapping image as the excitation laser is scanned over the WS_2 crystal. The mapping image shows uniform PL from the crystal confirming single crystalline nature, while a small dark spot is observed at the center. Figure 3-5c shows PL intensity profile across the crystal through the center to investigate the dark spot. Reduction in PL peak intensity was observed at the nucleation point of the triangular WS_2 crystal. The uniform and high PL intensity of the WS_2 crystal indicate good crystalline nature, which is consistent with previous studies [6], [7]. Figure 3-5d shows optical microscope image of a highly degraded triangular WS_2 crystal after 15 months of ambient exposure. PL mapping analysis was performed for the degraded WS_2 crystal at similar conditions as the previous case. Figure 3-5e shows the PL mapping image, significant reduction in PL intensity was observed at the degraded regions. Figure 3-5f shows the intesity profile analysis of the degraded WS_2 crystal. It can be confimred that the PL intesity significantly reduced at the degraded areas and considerably inhomogenous than that of as-synthesized crytals. These results confirm that the PL response is significantly inhomogeneous for the same crystal due to structural defect occurred with oxidation as observed from the FE-SEM analysis.

Figure 3-6a shows FE-SEM image of a curved-edge triangular WS_2 crystals after 15 months of uncontrolled atmospheric exposure with enlarged triangular degraded areas. Similarly, Figure 3-6b shows FE-SEM image of interconnected triangular WS_2 crystals after the long-term atmospheric exposure. In this case also, equilateral degraded triangular areas with opposite orientation to the original crystals are observed. However, the size of the degraded areas is not uniform in all the crystals. As explained above, such triangular degraded areas appeared with atmospheric oxidation along particular edge termination as well as basal plane of the equilateral triangular WS_2 single crystals. Figure 3-6c shows deconvoluted Raman spectra at non-degraded area (position 1) of a triangular WS_2 crystal measured using the green light ($\lambda = 532$ nm). Along with the first order and A_{1g} peaks other overtone and combination peaks arising from the Brillouin zone center and zone edge phonons are also observed.

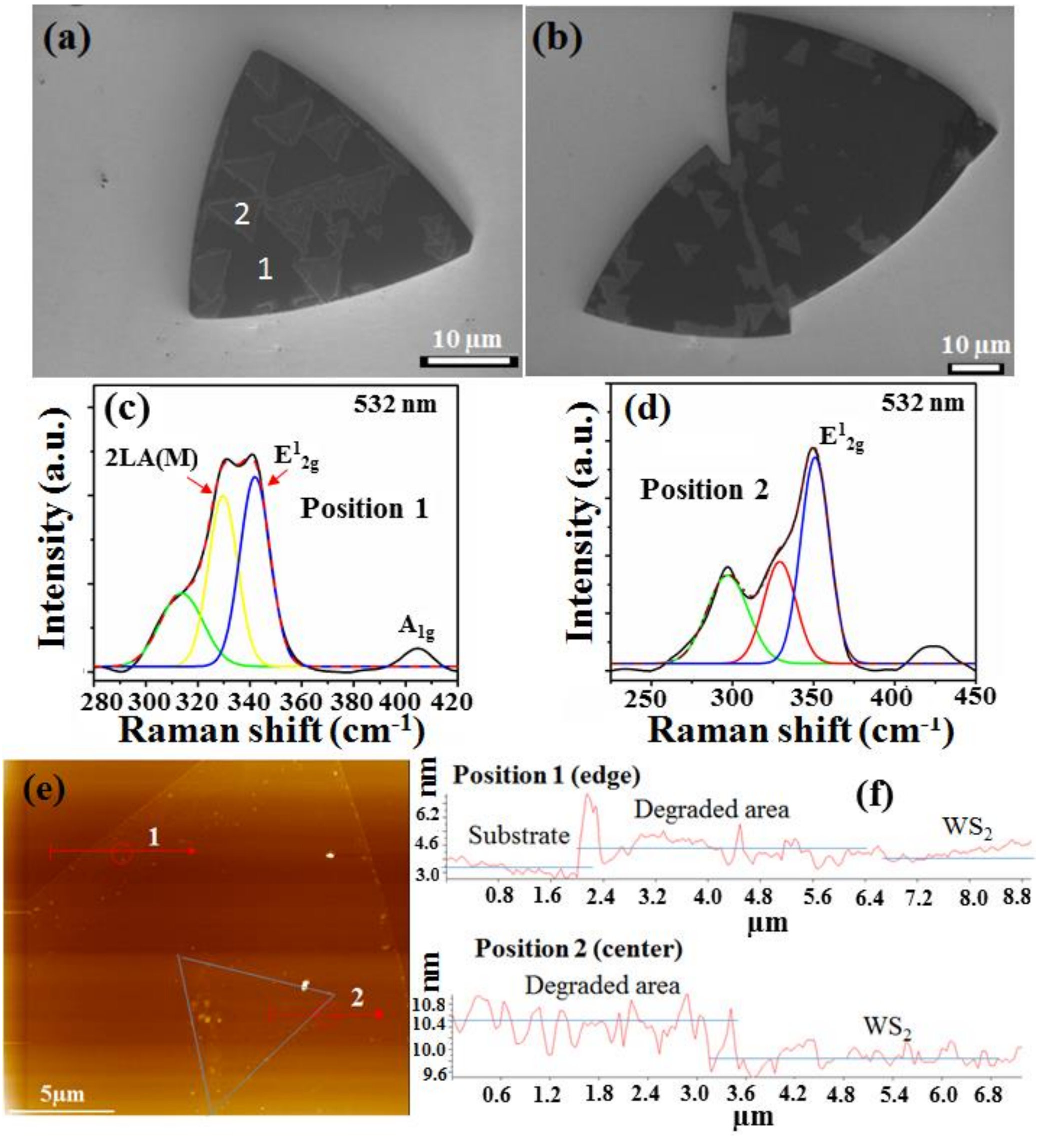

Figure 3-6 FE-SEM images of (a) individual and (b) interconnected triangular WS_2 crystals after 15 months of atmospheric exposure with enlarged triangular degraded areas. (c) Deconvoluted Raman spectra at non-degraded area (position 1) and (d) inside degraded triangle of the same WS_2 crystal (position 2). (e) AFM image of the triangular crystal presenting the degraded edges and formation of degraded triangle inside. (f) Line profile at degraded edge (position 1) and center (position 2) presenting the thickness difference within the WS_2 crystal.

We observed peak splitting near the E^1_{2g} band, which is labelled as 2LA(M), is a second-order Raman mode due to Longitudinal acoustic (LA) phonons at the M point in the Brillouin zone [9]. Further, we explored the degraded triangle inside the original WS_2

triangular crystal by Raman analysis. Figure 3-6d shows deconvoluted Raman spectra at the degraded triangular area with size of more than 5 µm (position 2) inside the WS_2 crystal. Considering the significant structural degradation of S-W-S layered structure and loss of sulfur with oxidation it should affect the photon vibration mode. We observed considerable difference in the first order E^1_{2g}, A_{1g} peaks as well as the other overtone and combination peaks, than that of the intact area of WS_2 layer. Further understanding of such Raman spectral behavior will be significant to understand the degradation mechanism. Figure 3-6e shows an AFM image of the triangular crystal, presenting the degraded edges and formation of degraded triangle inside. Variation in thickness within the same degraded crystal was investigated by the AFM line profile (at position 1 and 2 of Figure 3-6e). Figure 3-6f shows the line profile at degraded edge (position 1) and center (position 2) presenting the thickness difference within the WS_2 crystal. We observed increase in thickness of the degraded area as compared to the intact area, indicating structural deformation and oxidation. The S-W-S layer and crystalline structure was distorted with loss of sulfur atoms and subsequent oxidation that can aid in absorption of various chemical functional groups with the oxidation process. Thus, our study revealed the occurrence of regular degradation patterns in single crystal WS_2 layers under exposure to ambient condition for long duration. It has been reported that the oxidation and degradation of TMDCs layer occurred in presence of defects and vacancies [3]. The degradation can initiate from defects and vacancies of individual WS_2 crystals, where the exposed tungsten and sulfur atoms react with the moisture and atmospheric oxygen. As a result, the tungsten atoms formed oxide and oxidized sulfur molecules evaporated from the surface creating the degraded patterns. From the atomic model of WS_2 crystals as discussed above, it can be considered that the oxidation process propagates along particular edge terminations to create the observed regular degradation patterns.

3.2 Encapsulation of TMDCs

As discussed above the CVD synthesized WS_2 crystals on SiO_2/Si substrate is vulnerable to atmospheric degradation creating certain degraded patterns. In this background developing a solution to prevent atmospheric oxidation and degradation is key challenge for long-term practical device applications of the TMDCs layered materials. Previously, Gao *et al*. has proposed coating of MoS_2 and WS_2 layers by parylene C using a Union carbide parylene coater [3]. Ahn *et al*. has demonstrated transferring process of PMMA/h-BN layer on WSe_2 layer as degradation protective layer [12]. Very recently, Woodhead *et al*. have developed an optical solution for encapsulation of monolayer TMDCs to prevent from physical damage and degradation in air [13]. Studies also shows structural transformation and degradation of MX_2 layered materials under oxygen exposure, UV irradiation, ozone and heating under ambient conditions[1], [3], [14], [15]. Significant structural degradation of MX_2 layers has been also observed with long-term exposure to ambient conditions [3]. The other 2D layered semiconductors, such as black phosphorus are more unstable and degradable under ambient conditions [16]. In many of the device applications a simple dry coating approach of a hydrophobic surface can be more suitable. We demonstrate a two dry encapsulation approaches of the CVD synthesized WS_2 crystals by thermal evaporation of hydrophobic Teflon layer a fluorocarbon polymer and MW-SWP deposited carbonaceous layer to prevent atmospheric oxidation and degradation

3.2.1 Hydrophobic Teflon coating by low pressure thermal deposition

Teflon also known as polytetrafluoroethylene (PTFE) is a synthetic fluoropolymer with high melting point of 326.8 °C. The fluorocarbon layer is highly hydrophobic which prevent wetting and also reduces permeation of moisture and oxygen. The deposition of Teflon layer was carried out in high vacuum thermal evaporator at pressure of $7x10^{-4}$ Pa. 100 mg of dry Teflon powder was used for the room temperature deposition. Schematic for the deposition is represented in Figure 3-7a. Figure 3-7b shows optical microscope image the fluorocarbon coated WS_2 crystals. The Teflon layer was deposited at room temperature to prevent any structural damage on the WS_2 crystals. The accelerated degradation test by heating the samples with and without coating of a Teflon layer at around 200 °C for 90 mins, to confirm the encapsulation of the WS_2 crystals. Figure 3-7c shows PL spectra of the fresh WS_2 crystal without coating the Teflon layer before and after the accelerated heating test. The intensity of the PL peak reduces more than half after the atmospheric heating comparing to the initial PL peak. Similarly, Figure 3-7d shows the PL spectra of the Teflon coated WS_2 crystal before and after the accelerated heating test. We did not observe reduction of the PL peak after the accelerated heating test. Thus, we demonstrate a dry coating of a hydrophobic fluorocarbon layer on the WS_2 crystals to prevent atmospheric oxidation. The deposited fluorocarbon layer shows excellent optical transparency in the wavelength range of 500-700 nm (Figure 3-8). Furthermore, the coating of Teflon layer also enables sputtering deposition of oxide layers such as SiO_2, Al_2O_3 etc. without damaging the TMDCs later to create encapsulation stacking layers.

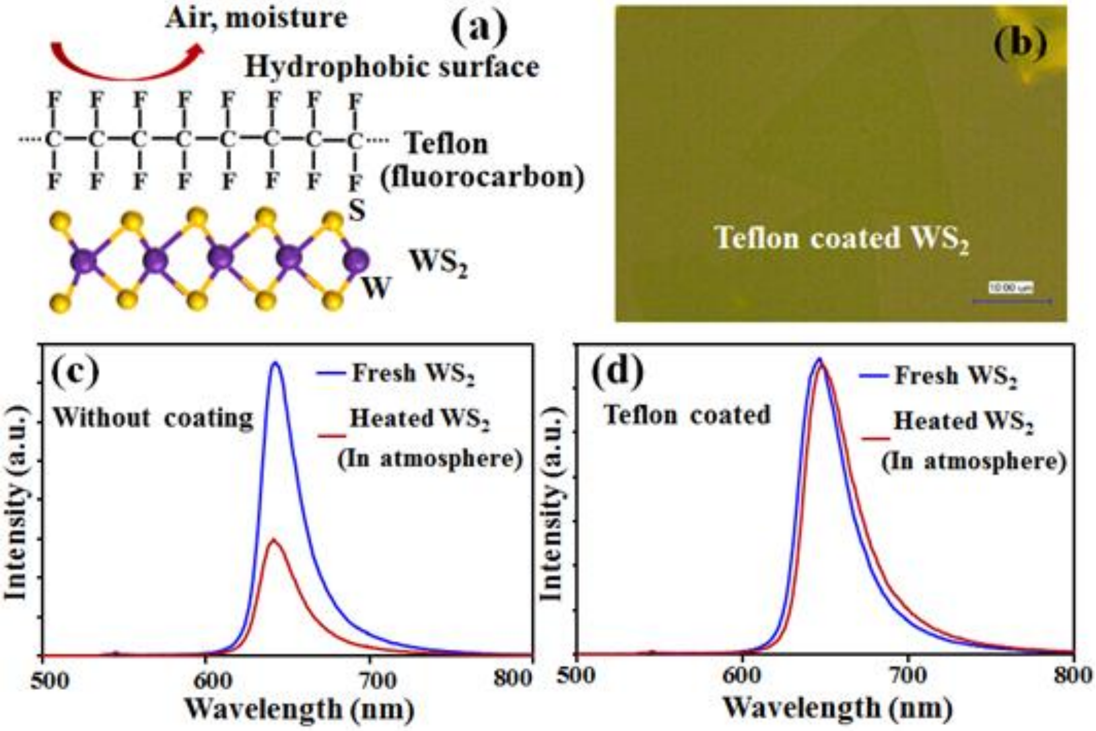

Figure 3-7 (a) Schematic of hydrophobic Teflon (fluorocarbon) as encapsulating layer on the WS_2 monolayer to prevent atmospheric degradation. (b) Optical microscope images of Teflon coated WS_2 crystal on the SiO_2/Si substrate. (c) PL spectra for fresh WS_2 crystal before and after accelerated heating test. (d) PL spectra for Teflon coated WS_2 crystal before and after accelerated heating test.

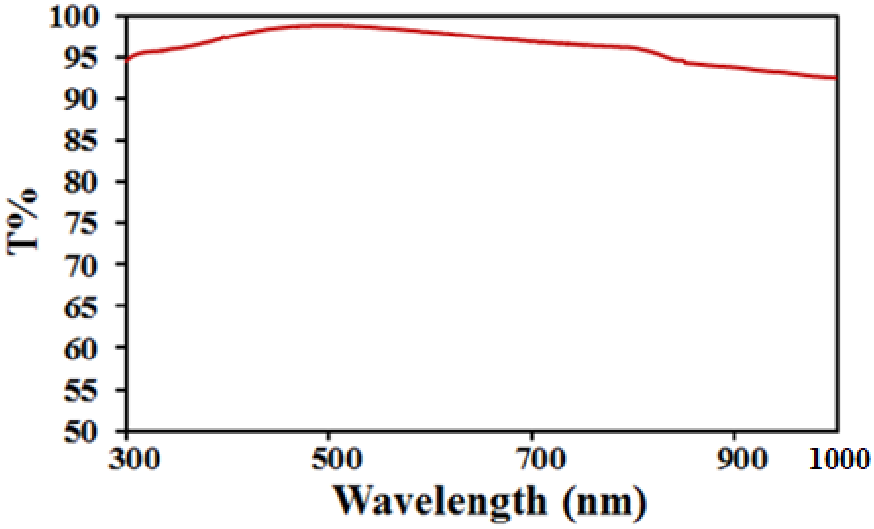

Figure 3-8 transparency of the Teflon thin film deposited on glass substrate along the coating of $WS_2/SiO_2/Si$ sample.

The transparency of the Teflon thin film was measured by JASCO V-670K spectrophotometer. The thin film shows excellent transparency (98%) in the wavelength range of 500~700 nm.

3.2.2 Encapsulation of TMDC crystals with room temperature plasma deposited carbonaceous film

3.2.2.1 Deposition of a carbonaceous film by plasma CVD

The deposition of carbonaceous film was performed by microwave assisted surface wave plasma (MW-SWP) chemical vapor deposition (CVD) technique on the MoS_2 and WS_2 crystals synthesized on SiO_2/Si substrates. The MW-SWP CVD chamber pressure was kept at 5×10^{-4} Pa prior to the deposition. The gas pressure during the deposition was at 10-20 Pa with a flow rate of 100-200 sccm of Ar and 10-50 sccm of CH_4. The microwave power was 800 W with negligible amount of fluctuation (5 W). Room temperature deposition of film was carried out for the period of 60-240 sec.

3.2.2.2 Results and discussion

APCVD synthesis process was used for MoS_2 crystals is discussed in earlier chapter no. 2. Optical microscope image of MoS_2 crystal synthesized on the SiO_2/Si substrate is represented in Figure 3-9a. MoS_2 crystals with Triangular shaped curved edges around 20 µm in size were synthesized in the particular growth condition.

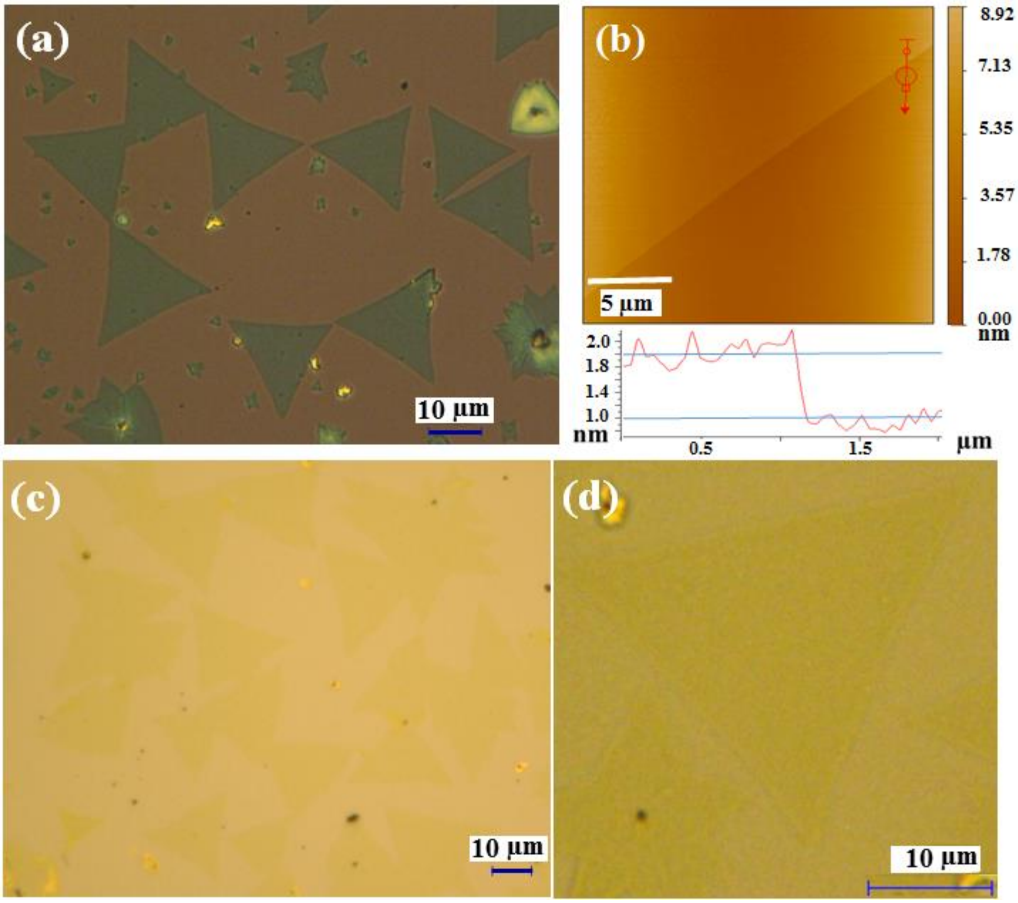

Figure 3-9(a) optical microscope images of as-synthesized MoS_2 crystal on the SiO_2/Si substrate. (b) AFM image of MoS_2 crystal and line profile presenting the thickness. Optical microscope images of carbonaceous coated (c) MoS_2 crystals and (d) higher resolution view of a triangular MoS_2 crystal.

Figure 3-9b shows an AFM image in which thickness of the crystals was measured to be nearly ~0.9 nm. The synthesized samples were directly transferred to MW-SWP CVD chambers for coating. Microwave excited plasma sources have been used for effective deposition of an insulating encapsulation layer for the conventional semiconductors [17], [18]. I explored the possibility of 2D layered materials encapsulation at room temperature by MW-SWP technique. The MW-SWP can produce an over-dense plasma even at a low gas pressure, with a density higher than the cut-off density (7.4×10^{16} m^{-3} for 2.45 GHz). The plasma shower and substrate were kept at significant distance so as to maintain the temperature of the substrate to room temperature. Figure 3-9c shows an optical microscope image of the coated MoS_2 crystals. No visible damage to the crystals was observed after plasma deposition. Figure 3-9d shows a high-resolution optical microscopy image of the MoS_2 triangular crystals, where the morphology is unaffected by deposition of the encapsulation film. Unlike other plasma technique, the MW-SWP is a promising tool for large-area carbonaceous film deposition and useful to avoid plasma induced damages of the substrate surface [19].

The IR absorption spectra for deposited film is represented in Figure 3-10a. Few weak peaks

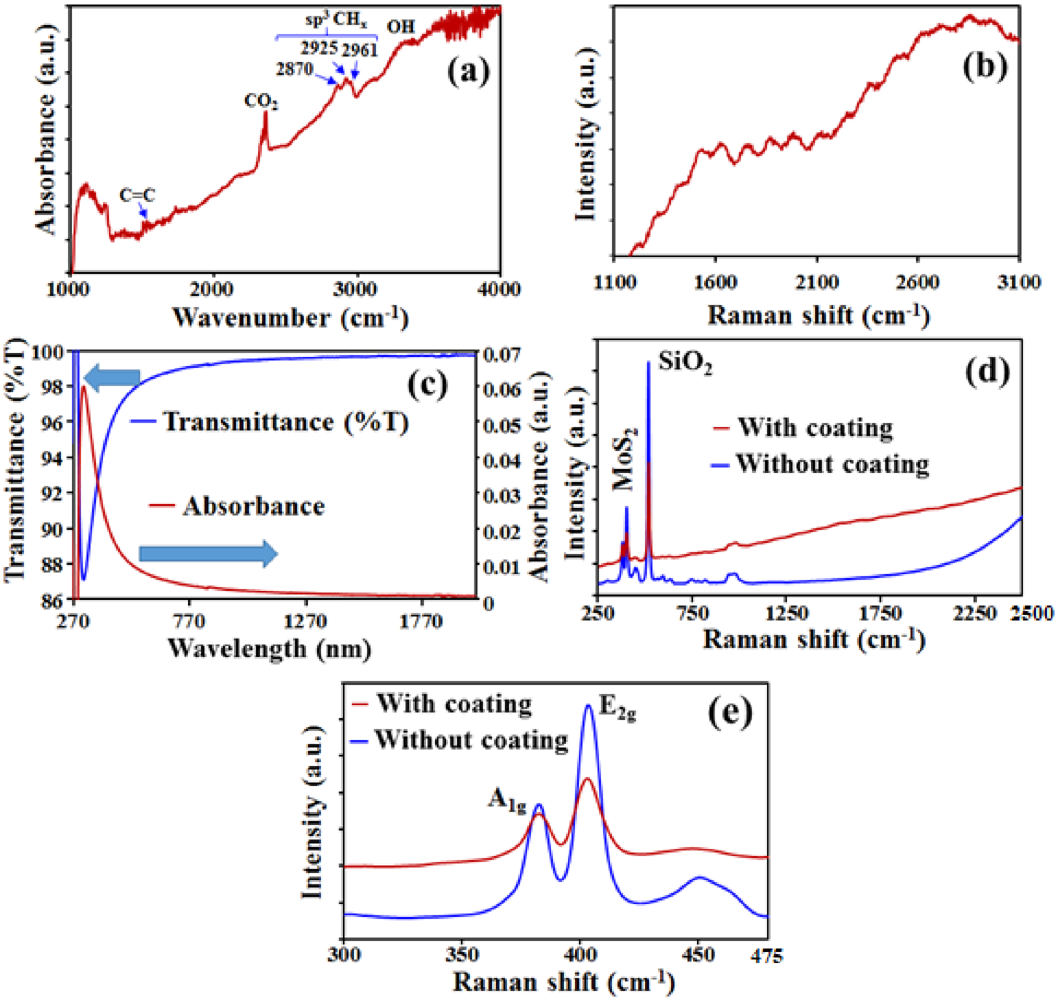

Figure 3-10 (a) IR (b) Raman (c) Transmittance and absorbance spectra of the carbonaceous film on SiO_2/Si and glass substrates, deposited along with the coating of TMDCs crystals samples. Raman spectra of the (d) MoS_2 crystal on SiO_2/Si substrate (e) A_{1g} and E_{2g} peaks with and without encapsulation film.

are observed in the frequency range from 1300 to 1600 cm^{-1}, where the peak centered at ~1530 cm^{-1} can be assigned to C=C stretching vibrations. At a higher frequency range, three sharper peaks at 2870, 2925 and 2961 cm^{-1} were observed corresponding to the C–H vibrations. These absorption peaks can be assigned to sp^3 CH$_x$ symmetric and asymmetric bands. Figure 3-10b shows a typical Raman spectrum of the carbonaceous coating. There were no significant Raman features for the plasma deposited carbonaceous film, other than a broad hump and reduction in intensity of Si Raman peak. The presence of sp^3 CH$_x$ bonds and no clear Raman peaks (D and G bands) signifies formation of insulating hydrogenated carbonaceous film [20], [21]. The absorbance and transmittance of carbonaceous film deposited on glass is shown in Figure 3-10c. The coated film shows excellent transparency in the wavelength range of 0.3-2 μm. More than 95 % transparency is obtained in the visible light region, which can be tuned with appropriate thickness of the deposited film. The absorption of light is <0.02% in the wavelength range of 500~800 nm. Comparative Raman spectra of $MoS_2/SiO_2/Si$ substrate with and without coating of carbonaceous layer is represented in Figure 3-10d and Figure 3-10e. The Raman vibration modes E^1_{2g} and A_{1g} for MoS_2 monolayer are observed at 383.2 and 403.3 cm^{-1}. The peak intensity was quenched for encapsulated sample due to secondary absorption by encapsulation layer; however the wavelength remained the same for both the samples. The compressive strain due to the layer was further analyzed by PL spectroscopy.

Figure 3-11a shows FE-SEM image of the as-synthesized MoS_2 crystals on SiO_2/Si substrate. The triangular shaped MoS_2 crystals can be confirmed by the FE-SEM analysis. Figure 3-11b shows the FE-SEM image of the plasma deposited carbonaceous film on MoS_2 crystals. The surface morphology of the encapsulated MoS_2 sample was observed by FE-SEM analysis using the upper electron detector (UED) and 2kV accelerating voltage. The triangular MoS_2 crystals can be confirmed below the encapsulation layer, although the non-conducting encapsulation film significantly affects the micrograph. The difference in PL property of coated and non-coated sample was investigated. Figure 3-11c shows the PL spectra of coated and non-coated MoS_2 crystal. Quenching and red shift of the PL peak for the encapsulated MoS_2 sample was observed. The PL quenching and shift can be explained pertaining to the compressive strain on the MoS_2 crystal with the encapsulation. Woodhead *et al*. have also reported significant suppression of the PL peak of MoS_2 monolayer by solution coated epoxy due to the compressive strain. Compressive strain can modulate the direct to indirect band gap of MoS_2 crystals, which reduces the emission intensity.

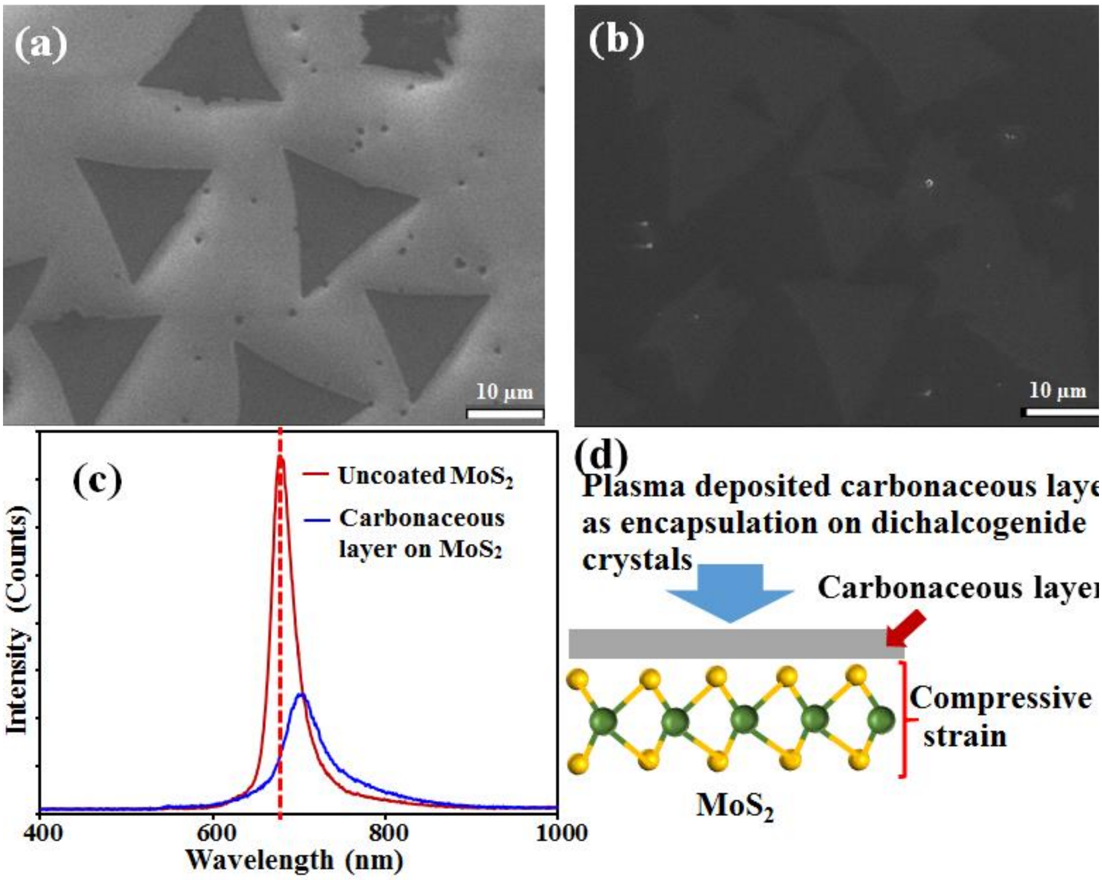

Figure 3-11 FE-SEM image of (a) as-synthesized and (b) carbonaceous film coated MoS_2 crystal. (c) Photoluminescence (PL) spectra of the uncoated and coated MoS_2 crystal. (d) Schematic of induced compressive strain on the MoS_2 crystal in presence of Encapsulation film.

The required values of strain to induce a shift from direct to indirect bandgaps for MoS_2 and WS_2 are 0.5% and 1% respectively [22]. Figure 3-11d shows a schematic diagram for the induced compressive strain in the MoS_2 crystal with the plasma deposited thin film on top. The thickness of the top encapsulated layer significantly affects the induced strain on the dichalcogenides layer, which was further investigated for the triangular WS_2 crystals.

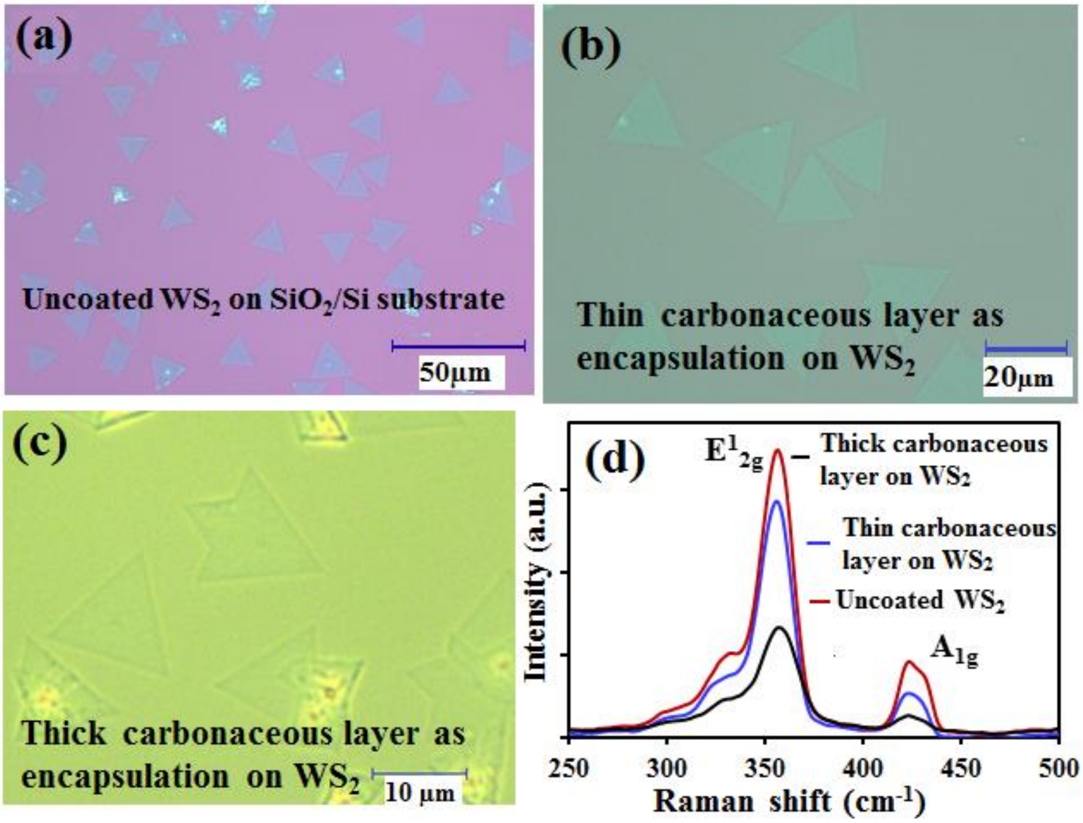

Figure 3-12 Opitcal miscroscope image of (a) CVD synthsized triangular WS$_2$ crystals on SiO$_2$/Si substrate, (b) and (c) MW-SWP deposited carbonaceous film on the CVD synthesized WS$_2$ crystals with different thickness. (d) Raman spectra of the WS$_2$ crystal before and after encapsulation.

Figure 3-12a shows optical microscope image of CVD synthesized triangular WS$_2$ crystals on SiO$_2$/Si substrate. Figure 3-12b shows optical microscope image of WS$_2$ crystals on the SiO$_2$/Si substrate after coating a thin carbonaceous film (~15 nm). Similarly, Figure 3-12c shows an optical microscope image of WS$_2$ sample with a thicker coated layer (~30 nm). The difference in coating thickness can be also identified with variation in contrast of the optical images. The WS$_2$ crystals remain unaffected after the room temperature deposited encapsulation layer as observed from the optical microscopy images. Further, Raman spectroscopy analysis was carried out to investigate the structural properties. Figure 3-12d shows the Raman spectra of the WS$_2$ crystals before and after coating the encapsulation layer. The as-synthesized WS$_2$ crystals on SiO$_2$/Si substrate shows characteristic Raman shift at ~356 and ~423 cm^{-1}. Although, the Raman shift does not show any considerable change from the original sample, the intensity of Raman peak shows reduction with increasing thickness of encapsulation layer. The structure and the chemical nature of the WS_2 crystals is virtually unaffected by carbonaceous coating as the Raman vibration modes are at the same frequency for as synthesized as well as coated samples.

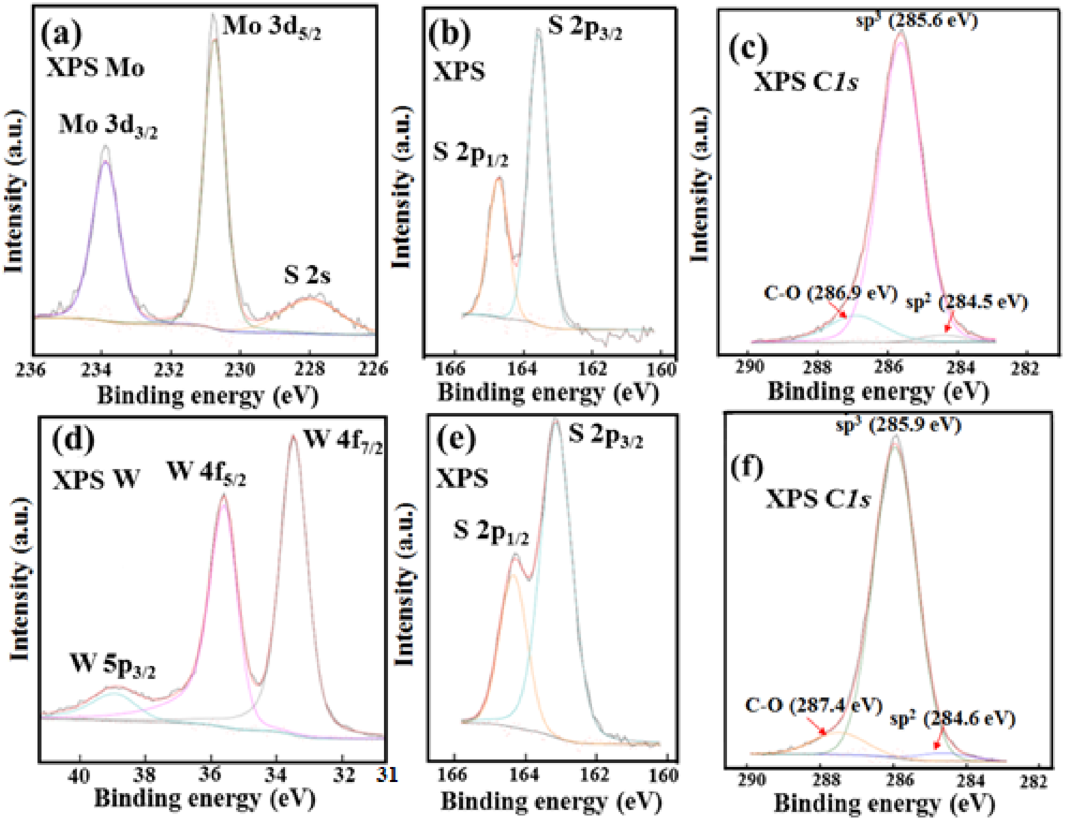

Figure 3-13 Deconvoluted XPS core-level spectra of (a) Mo3d, (b) S2p, (c) C1s for the encapsulated MoS_2 sample and (d)W4f, (e) S2p, (f) C1s for the encapsulated WS_2 sample.

XPS analysis was performed to investigate the elemental composition and bonding nature of the dichalcogenide crystals. Figure 3-13a shows Mo3d peak of fresh MoS_2 crystals with peak center at 233.88 and 230.74 eV, corresponding to the Mo $3d_{3/2}$ and Mo $3d_{5/2}$. The small wide peak at lower binding energy (227.95 eV) corresponds to S 2s peak. Figure 3-13b shows deconvoluted XPS core-level spectra of S2p with peak-centers at 164.7 and 163.8 eV corresponding to the S $2p_{1/2}$ and S $2p_{3/2}$, respectively. Figure 3-13c shows deconvoluted C1s XPS spectra with a strong peak at 285.6 eV corresponding to

sp^3 hybridization as also observed from IR analysis, with small peaks for sp^2 hybridized (284.5 eV) and C-O (296.9) related carbon atoms. Similarly, the XPS spectra of the fresh and encapsulated WS_2 samples was explored. Figure 3-13d shows deconvoluted XPS spectra of molybdenum 4f peak, confirming the chemical doublet $W4f_{7/2}$ (33.5 eV) and $W4f_{5/2}$ (35.6 eV) along with the $W5p_{3/2}$ (39.3 eV) peak. Similarly, Figure 3-13e shows deconvoluted XPS spectra of S2p peak for the synthesized WS_2 layers with peaks at ~ 164.4 and ~ 163.2 eV, corresponding to $S2p_{1/2}$ and $S2p_{3/2.}$ Figure 3-13f shows deconvoluted C1s XPS spectra with a strong peak at 285.6 eV for encapsulated WS_2 sample, which is almost identical with the encapsulated MoS_2 sample. The room temperature plasma deposited carbonaceous layer does not influence the dichalcogenide crystal structure without significant chemical modifications. The expectation is that the carbonaceous layer on the top of dichalcogenide crystals can act as excellent encapsulation layer and prevent degradation.

The encapsulation behavior of WS_2 crystals with the plasma deposited carbonaceous film was investigated by accelerated heating test in atmospheric conditions. Figure 3-14a shows FE-SEM image of a pristine triangular WS_2 crystals after heating in atmosphere at 200 °C for 1 hours. White traces and their branched structures appear thought-out the crystals, signifying the heat-induced degradation of the MX_2 layer under atmospheric conditions. Figure 3-14b shows FE-SEM image of the encapsulated WS_2 crystals after the same accelerated heating test. The triangular WS_2 crystals remain intact, however, it is difficult to identify any kind of traces as observed for the uncoated sample due to the presence of the encapsulation layer. PL analysis was carried out to investigate the change in strain and encapsulation effect of the WS_2 crystals before and after the heating of the samples. Figure 3-14c shows PL spectra of the uncoated and encapsulated WS_2 samples. A sharp PL peak at 655 nm (1.89 eV) is obtained for the pristine WS_2 triangular layer. Coating the encapsulated layer significant difference in PL peak is observed as obtained for the MoS_2 crystal. Coating a thin encapsulation layer (~15 nm) on the WS_2 crystals, decrease in PL intensity and red shift (shifted to 662 nm corresponding to 1.87 eV) is observed (Figure 3-14c).

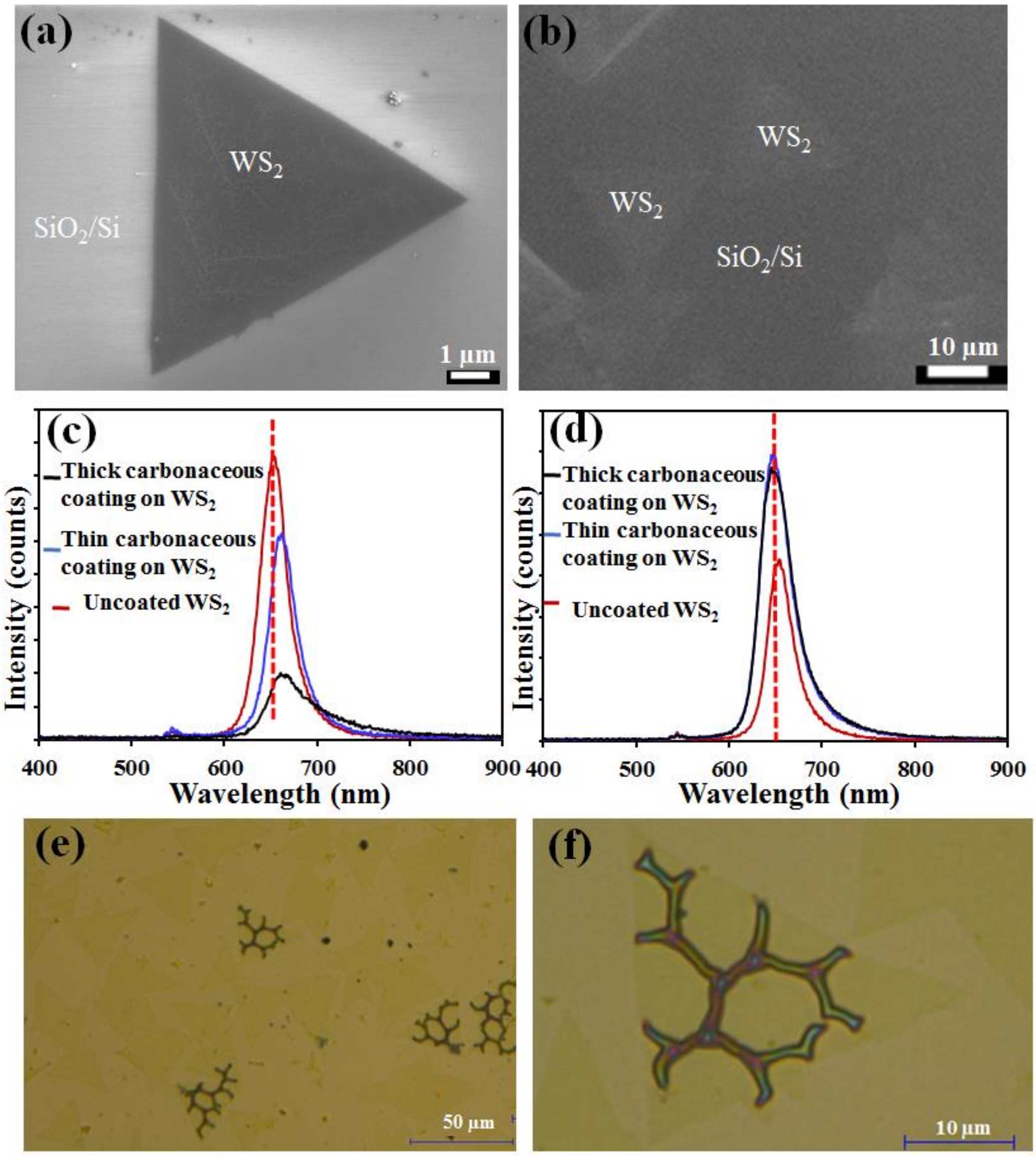

Figure 3-14 FE-SEM images of triangular WS_2 crystals (a) with and (b) without coating a carbonaceous film after heating in atmosphere at 200 °C for 1 hours. PL spectra for (c) before and (d) after heating of the WS_2 crystals with different thickness of encapsulation layers in comparison with uncoated sample. (d) Optical microscope images of the (e) encapsulated WS_2 sample after heating in atmosphere at 250 °C and (f) cracks formation in a WS_2 crystals after the heating.

By increasing the thickness of the encapsulation layer (~30 nm), a significant decrease in PL peak with the similar red shift was observed. The reduction in PL intensity and red shift can be explained by the induced strain effect as also observed for the MoS_2 crystal. Then, PL analysis is performed for the coated and uncoated WS_2 samples after heating at 200 °C in atmospheric condition (Figure 3-14d). After the heating process, both the encapsulated WS_2 samples show similar intensity PL peak with a peak position at 650 nm (1.90 eV). The PL peak of the uncoated WS_2 crystals was reduced due to the degradation under atmospheric heating as observed from the SEM analysis. Interestingly, the PL peak position of the coated sample slightly blue shifted (~5 nm) and significantly differed prior to the heating (~12 nm). This also indicates the change in induced strain in the encapsulated WS_2 sample after the heating process. The local temperature on WS_2 is much higher than those on the insulating carbonaceous layer and SiO_2/Si substrate, which can lead to a strong thermal expansion of the WS_2 layer. The thermal expansion of encapsulated WS_2 crystals can modulate the induced strain [23]. Then, the coated samples were further tested by heating at a higher temperature (250 °C) in atmospheric condition. Figure 3-14e shows the optical image of the carbonaceous coated WS_2 sample after the heating experiment. The crack formation in some of the WS_2 crystals after the heating process was noticed. Figure 3-14d shows a higher magnified view of the coated WS_2 crystals with clearly visible cracks. The cracks appeared in the WS_2 crystals, which propagate in hexagonal patterns, with nearly 120° angles. This signifies localized heat induced defect formation in the individual encapsulated WS_2 crystals. Significantly, the appearance of the cracks was seen only in few WS_2 crystals, where all other crystals remain unaffected. The reason behind this anomaly can be attributed to the difference in defect level of individual crystals and variation in induced strain with thermal expansion. This demonstrates an encapsulation technique of the dichalcogenide crystals by room temperature plasma deposited carbonaceous film. Again, the induced strain, on the dichalcogenide crystals with the encapsulated layer, changes with heat treatment, paving a way to modulate the induced strain.

The effect of encapsulation layer on electrical and optical properties of MoS_2 was studied by Schottky junction fabrication. Figure 3-15a shows the schematic diagram of the Au/MoS_2/Au device with the carbonaceous layer. The distance between two Au electrodes was approximately 200 µm covering MoS_2 layer in between as shown in the optical microscope image (Figure 3-15b). *J-V* characteristics of the device was measured with (white light, ~100 mW/cm^2) and without light illumination conditions.

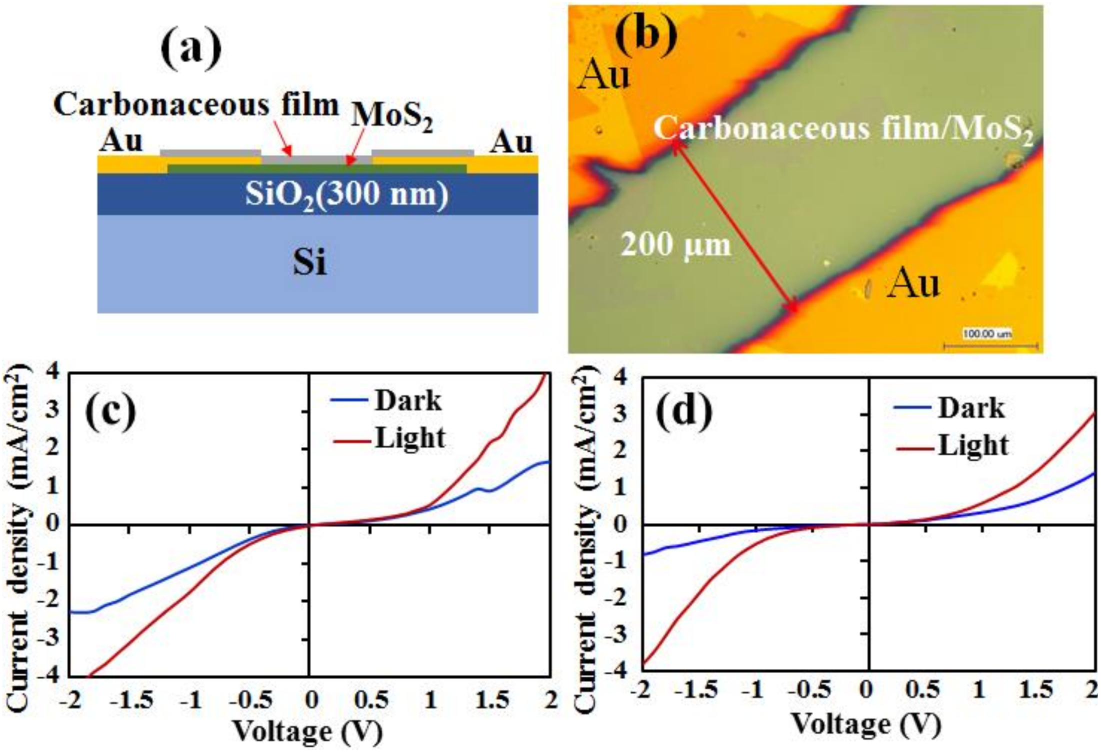

Figure 3-15 (a) Schematic diagram and (b) optical microscope image of Au/MoS_2/Au device with encapsulating carbonaceous layer. Current-voltage (*J-V*) characteristics of (c) as-fabricated and (d) after annealing at 200°C for 1hr. Au/MoS_2/Au device under dark and light illumination.

Figure 3-15c shows *J-V* characteristic under dark and light conditions of the as-fabricated device with plasma deposited encapsulated layer. Nonlinear Schottky junction behavior was obtained for the semiconducting MoS_2 layer and Au metal electrode, where the encapsulated layer did not show much influence on junction behavior. With illumination of light we observed significant photo-response for Schottky junction with photo-exciton in the MoS_2 layer. Then, the device was annealed at 200 °C under atmospheric condition for 1 hr. as discussed above. Figure 3-15d shows *J-V* characteristic of the same device after annealing. The Schottky junction behavior and photo-responsivity was unchanged and no hysteresis was observed with the annealing in presence of the encapsulating layer. Thus, the effectiveness of carbonaceous encapsulating layer on electrical and photo-responsive properties of MoS_2 layer was confirmed.

3.3 Conclusion

In conclusion, it is demonstrated in detail, the degradation process of TMDCs upon long term exposure to ambient conditions and protective methods viz., dry coating with Teflon layer by thermal deposition as well as deposition of a carbonaceous film at room temperature on MoS_2 and WS_2 crystals by the SW-MWP CVD technique as an encapsulation layer. The encapsulation process is dry, rapid and nondestructive, which can be carried out at room temperature for large area substrate. PL analysis confirmed that the carbonaceous encapsulation layer induced a compressive strain in the dichalcogenide crystals. The encapsulated samples remained intact as observed by the optical microscopy, SEM and PL analysis in an accelerated degradation test by heating in humid and ambient conditions. The change in induced strain was also observed for the encapsulated dichalcogenides crystals after the heating process considering the effect of thermal expansion. Further, double Schottky junction fabricated using thermal CVD synthesized MoS_2 under the encapsulation was studied for the effect of high temperature annealing. The effectiveness of encapsulation layer was realized by stable electro and photo responsive properties of the device under high temperature. The rapid and dry coating technique at room temperature can be extended to various other 2D materials as MW-SWP process allows damage free encapsulation.

As in the encapsulation studies showed a foreign material can be directly deposited to reduce environmental degradation, heterostructure devices were designed by depositing a foreign semiconductor on top of MoS_2 layer. The junction properties and photoresponsive behavior were investigated for the fabricated heterostructure devices. The combination of materials with MoS_2 layers and their device properties were investigated considering the present limitation of Si based devices. It is well-known that the main limitation of Si based photodiode is low responsivity at shorter wavelength (<500 nm) due to surface recombination, and almost no photoresponsivity beyond 1100 nm wavelength. In this prospect, Ge based device for infrared (IR) photodiode and wide bandgap semiconductor for ultraviolet photodiode have widely investigated for practical applications. In this context, I have investigated the possibility of fabricating MoS_2 based heterostructure device with the combination of low bandgap (Ge) and wide bandgap (CuI) semiconductors. Again, considering the layered structure of Ge and CuI materials similar with MoS_2 layer, a thin interface can be created to develop high and fast photoresponsive devices.

3.4 References

[1] Y. Rong, K. He, M. Pacios, A. W. Robertson, H. Bhaskaran, and J. H. Warner, "Controlled preferential oxidation of grain boundaries in monolayer tungsten disulfide for direct optical imaging," *ACS Nano*, vol. 9, no. 4, pp. 3695–3703, 2015.

[2] T. H. Ly *et al.*, "Observing grain boundaries in CVD-grown monolayer transition metal dichalcogenides," *ACS Nano*, vol. 8, no. 11, pp. 11401–11408, 2014.

[3] J. Gao, B. Li, J. Tan, P. Chow, T. M. Lu, and N. Koratkar, "Aging of Transition Metal Dichalcogenide Monolayers," *ACS Nano*, vol. 10, no. 2, pp. 2628–2635, 2016.

[4] Z. He *et al.*, "Revealing Defect-State Photoluminescence in Monolayer WS_2 by Cryogenic Laser Processing," *ACS Nano*, vol. 10, no. 6, pp. 5847–5855, Jun. 2016.

[5] G. Mirabelli *et al.*, "Air sensitivity of MoS_2, $MoSe_2$, $MoTe_2$, HfS_2, and $HfSe_2$," *J. Appl. Phys.*, vol. 120, no. 12, p. 125102, Sep. 2016.

[6] Y. Rong *et al.*, "Controlling sulphur precursor addition for large single crystal domains of WS_2," *Nanoscale*, vol. 6, no. 20, pp. 12096–12103, 2014.

[7] I. Bilgin *et al.*, "Chemical Vapor Deposition Synthesized Atomically Thin Molybdenum Disulfide with Optoelectronic-Grade Crystalline Quality," *ACS Nano*, vol. 9, no. 9, pp. 8822–8832, Sep. 2015.

[8] A. M. Van Der Zande *et al.*, "Grains and grain boundaries in highly crystalline monolayer molybdenum disulphide," *Nat. Mater.*, vol. 12, no. 6, pp. 554–561, 2013.

[9] H. Zhou *et al.*, "Thickness-dependent patterning of MoS_2 sheets with well-oriented triangular pits by heating in air," *Nano Res.*, vol. 6, no. 10, pp. 703–711, 2013.

[10] S. Helveg *et al.*, "Atomic-Scale Structure of Single-Layer MoS_2 Nanoclusters," *Phys. Rev. Lett.*, vol. 84, no. 5, pp. 951–954, Jan. 2000.

[11] R. Addou *et al.*, "Impurities and Electronic Property Variations of Natural MoS_2 Crystal Surfaces," *ACS Nano*, vol. 9, no. 9, pp. 9124–9133, Sep. 2015.

[12] S. Ahn *et al.*, "Prevention of Transition Metal Dichalcogenide Photodegradation

by Encapsulation with h-BN Layers," *ACS Nano*, vol. 10, no. 9, pp. 8973–8979, Sep. 2016.

[13] C. S. Woodhead *et al.*, "Increasing the light extraction and longevity of TMDC monolayers using liquid formed micro-lenses," *2D Mater.*, vol. 4, no. 1, p. 015032, Dec. 2016.

[14] D. Mahalu, M. Peisach, W. Jaegermann, A. Wold, and R. Tenne, "Controlled photocorrosion of tungsten diselenide: influence of molecular oxygen," *J. Phys. Chem.*, vol. 94, no. 21, pp. 8012–8013, Oct. 1990.

[15] Y. Liu *et al.*, "Thermal Oxidation of WSe_2 Nanosheets Adhered on SiO_2/Si Substrates," *Nano Lett.*, vol. 15, no. 8, pp. 4979–4984, Aug. 2015.

[16] J. D. Wood *et al.*, "Effective passivation of exfoliated black phosphorus transistors against ambient degradation," *Nano Lett.*, vol. 14, no. 12, pp. 6964–6970, 2014.

[17] D. R. Cote *et al.*, "Plasma-assisted chemical vapor deposition of dielectric thin films for ULSI semiconductor circuits," *IBM J. Res. Dev.*, vol. 43, no. 1.2, pp. 5–38, Jan. 1999.

[18] S. Ueno, M. Yomogida, M. Suzuki, Y. Konishi, and K. Azuma, "Highly Reliable Encapsulation Films for OLEDs Composed of SiNx and SiOxCy Prepared Using SWP-CVD," *ECS Trans.*, vol. 50, no. 41, pp. 57–64, Apr. 2013.

[19] G. Kalita *et al.*, "Fluorine incorporated amorphous carbon thin films prepared by Surface Wave Microwave Plasma CVD," *Diam. Relat. Mater.*, vol. 17, no. 7–10, pp. 1697–1701, Jul. 2008.

[20] L. Holland and S. M. Ojha, "Deposition of hard and insulating carbonaceous films on an r.f. target in a butane plasma," *Thin Solid Films*, vol. 38, no. 2, pp. L17–L19, Oct. 1976.

[21] J. Xiao *et al.*, "Facile synthesis of hydrogenated carbon nanospheres with a graphite-like ordered carbon structure," *Nanoscale*, vol. 5, no. 22, p. 11306, Oct. 2013.

[22] M. L. Tsai *et al.*, "Monolayer MoS_2 heterojunction solar cells," *ACS Nano*, vol. 8, no. 8, pp. 8317–8322, 2014.

[23] C. Hu, X. Zeng, J. Cui, H. Chen, and J. Lu, "Size Effects of Raman and Photoluminescence Spectra of CdS Nanobelts," *J. Phys. Chem. C*, vol. 117, no. 40, pp. 20998–21005, Oct. 2013.

CHAPTER 4

4. Photovoltaic action with broadband photoresponsivity in germanium-MoS_2 ultrathin heterojunction

4.1 Introduction

The encapsulation of MoS_2 to prevent atmospheric degradation has been compiled in previous chapter. It was confirmed that covering the exposed surface of these TMDCs with stable materials provide effective encapsulation. In this prospect the deposition of foreign material on top of MoS_2 surface to form a heterojunction was investigated which would also act as barrier between MoS_2 and atmospheric exposure. In this prospect, I explored the possibility of MoS_2 and Ge heterostructure, where Ge is used as top layer to study photoelectric properties. Previous studies showed that the heterojunction of two dimensional (2D) and bulk semiconductors has promising prospects in next generation photonic and nanoelectronic device applications [1]-[9]. 2D materials with particular electronic band structure and charge transport characteristics also show great potential in combination with bulk semiconductors like germanium (Ge), silicon (Si) and compound semiconductors [9]-[13]. Semiconductors with particular bandgap, such as Ge and Si are ahead of other materials for use in various electronic device applications [14], [15]. Ge is widely used in optoelectronic devices, which is due to its large absorption coefficient at near-Infrared (IR) and ease of its fabrication [16]-[18]. For practical applications various broadband infrared (IR) photodetectors, with various configurations based upon Ge have been developed [18]–[22]. The use of broadband photodetectors with photosensitivity to ultraviolet (UV), visible and near infrared (IR) is crucial for technologies such as multicolor imaging, optical communication, and day/night-time surveillance [23]–[27]. Such Photodetectors, without any external power supply, are important which can be easily integrated into portable and flexible devices [27]. There is a great need in the current development, of a self-powered broadband photodetector having fast response speed, high photoresponsivity and non-degradable device performance [23], [24]. In this prospect, atomically thin transition metal dichalcogenides (TMDCs) can be combined with Ge, for exploring newer possibilities in the field of optoelectronic devices.

Graphene, Si and other semiconductor materials **have** been integrated with monolayer TMDCs for their unique properties of the heterojunction [28]–[30].

Photovoltaic device applications have been demonstrated by depositing monolayer MoS_2 on p-type Si wafer [31], [32]. In a recently, germanene (atomic layer of Ge) combined atomically with plane MoS_2 layer to obtain a super lattice structure [33], [34]. Effect of ultrathin Ge film deposition on MoS_2 layer were studied which were synthesized by chemical vapor deposition (CVD). Previous studies have effectively demonstrated an efficient broadband (350-1650 nm) photodetector upon integration of graphene with Ge [35]. Fabricated graphene-Ge Schottky junction diode were validated for high-performance photodetector applications [36]. Similarly, a Schottky junction device with photoresponsivity in the visible light by integrating MoS_2 layer with graphene [30], [36]. Lin *et. al.* has fabricated Ge-monolayer MoS_2 heterostructure by CVD method and demonstrated the charge transfer process [37]. The optoelectronic properties of Ge and TMDCs heterostructures have not been explored previously, this can be an interesting prospect for photo-responsive device applications. In contrast to previous reports, my study examines the possibility of fabricating a CVD synthesized MoS_2 and Ge ultrathin film heterojunction device. The photovoltaic action with wide wavelength photoresponsivity in the fabricated heterostructure has been demonstrated, which signifies the prospect of developing self-powered broadband photodetectors.

4.2 Experimental

By thermal chemical vapor deposition (CVD) method MoS_2 layer was synthesize on SiO_2/Si substrate by controlling the growth parameters as explained below. Thermal CVD system with quartz tube was used for synthesis, with a mixture of Argon (Ar) and hydrogen (H_2) gas at atmospheric pressure. The substrate was cleaned using acetone and followed by isopropyl alcohol (IPA) for 15 min each by sonication prior to the thermal CVD growth. Quartz tube of length 90 cm and diameter of 4.5 cm were used for the experiment. Sulfur powder (1 gm) in a ceramic boat were inserted inside this tube. The tube was placed in a low-temperature furnace (LTF) and heated to 180 °C. The substrate and MoO_3 (10 mg) was kept for growth on a ceramic boat in the high-temperature furnace (HTF), where MoS_2 was synthesized at 750 °C. The experiment was performed using Ar and H_2 gas mixture (97:3) at 100 standard cubic centimeters per minute (sccm). Ge thin film was deposited by thermal evaporation technique on the CVD synthesized MoS_2 layers. For this study, High purity Ge (99.99%) purchased from Nilaco Corporation, Japan. Under a high vacuum condition (7×10^{-4} Pa), 50 mg of Ge was heated to its-melting temperature (~938 °C) on a tungsten boat. On the top of the tungsten boat, substrate holder with $MoS_2/SiO_2/Si$ sample was positioned, for the Ge deposition. To expose only a portion of MoS_2 layer sample, a shadow mask was placed above. Metal electrodes of Au and Al were deposited by thermal evaporation on Ge and MoS_2 layers, respectively. The device size used for the *J*-*V* characterization was approximately 0.09 cm^2.

4.3 Characterization

Basic characterization of CVD synthesized MoS_2 as well as Ge was performed by Optical, FE-SEM, AFM, Raman and XPS spectroscopy. Current density-voltage (*J*-*V*) characteristic measurements were carried out at room temperature using two probes system and a Keithley 2401 SourceMeter. Quantum efficiency (QE) measurement was done using a SM-250 hyper monochromatic light system. The transient photoresponse characteristics were measured using a xenon lamp unit (SM-25, Bunkoukeiki Co. Ltd., Japan) with a monochromator.

4.4 Results and Discussion

Figure 4-1a and b show optical microscope image of MoS_2 layers synthesized on SiO_2/Si substrate by the CVD technique. Triangular shaped MoS_2 crystals of millimeter scale area and continuous layer were obtained under the specific growth condition. The optical image shows the large-area having good quality MoS_2 film with fewer surface impurities. The formation of heterostructure was investigated by thermally evaporating a Ge film on the CVD synthesized MoS_2 layer. Figure 4-1c shows optical image of uniformly deposited Ge film on the MoS_2 layer. During the evaporation of Ge, the substrate temperature reached to approximately 120 ºC.

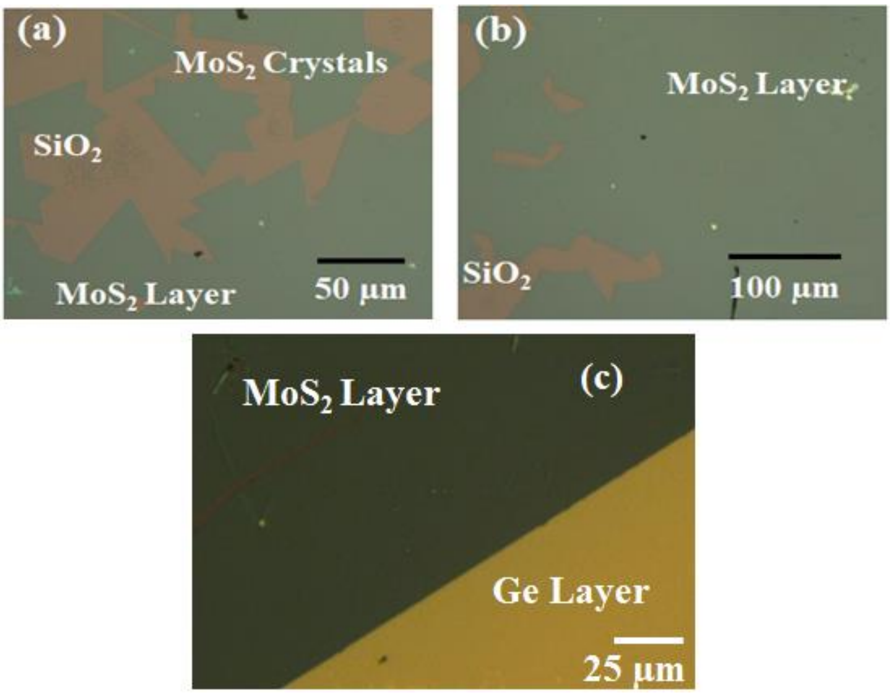

Figure 4-1**:** Optical microscope images of (a) triangular MoS_2 crystals, (b) continuous layer and (c) Optical microscope image of continuous Ge-MoS_2 heterostructure

Due to the high surface uniformity and smoothness of the base MoS_2 layer, the deposited Ge forms a continuous film rather than forming clusters.

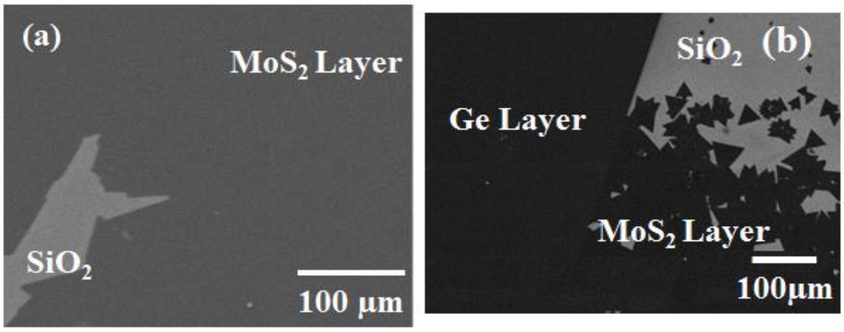

Figure 4-2 (a) SEM images of as-synthesized uniform MoS_2 layer and (b) SEM image of the Ge-MoS_2 interface on SiO_2/Si substrate

Further, SEM image was analyzed to confirm the uniformity and continuity of the layer as shown in Figure 4-2a. By using the enhanced CVD process, a continuous film of MoS_2 as large as 4 cm^2 can be synthesized. Similarly, Figure 4-2b shows SEM image of the deposited Ge film on the MoS_2 layer. The interface of MoS_2 and Ge on SiO_2/Si substrate can be seen clearly with a large triangular MoS_2 crystals at the edge of the film.

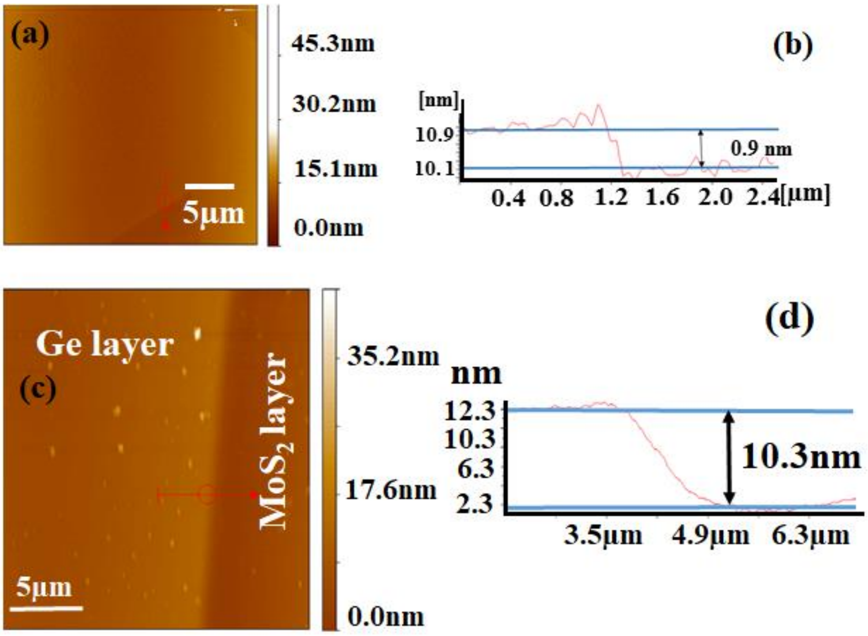

Figure 4-3 (a) AFM image for the MoS_2 layer, (b) Line profile showing a thickness of MoS_2 layer on SiO_2/Si substrate, (c) AFM image of Ge-MoS_2 interface and (d) Line profile showing a thickness of Ge film as 10.3 nm

AFM analysis was performed at the edge of the MoS_2 layer and SiO_2/Si substrate as shown in the Figure 4-4a and Figure 4-3b. An estimated thickness of 0.9 nm was found for MoS_2 layer. It was found that the root mean square (RMS) value of the height variations of the synthesized MoS_2 layer on SiO_2/Si substrate was approximately 0.58 nm [38]. The thickness of Ge film was measured by AFM which and was found to be nearly 10.3 nm as shown in Figure 4-3c and line profile Figure 4-3-d. A Van der Waals heterostructure of the Ge layer was thus obtained on CVD synthesized MoS_2 monolayer for examining its broadband photoresponsive device application.

Figure 4-4a shows Raman spectra for the as-synthesized MoS_2 film on SiO_2/Si substrate. The E_{2g} peak for in-plane vibrations of Mo and S atoms and A_{1g} peak for out of plane vibrations of S atoms are obtained at 383.5 cm^{-1} and 404.5 cm^{-1}, respectively. The full width half maximum (FWHM) of the A_{1g} peak is slightly greater than that of the E^1_{2g}

peak. The frequency difference of 21 cm^{-1} was found for the characteristic Raman peaks in the MoS_2 film [39].

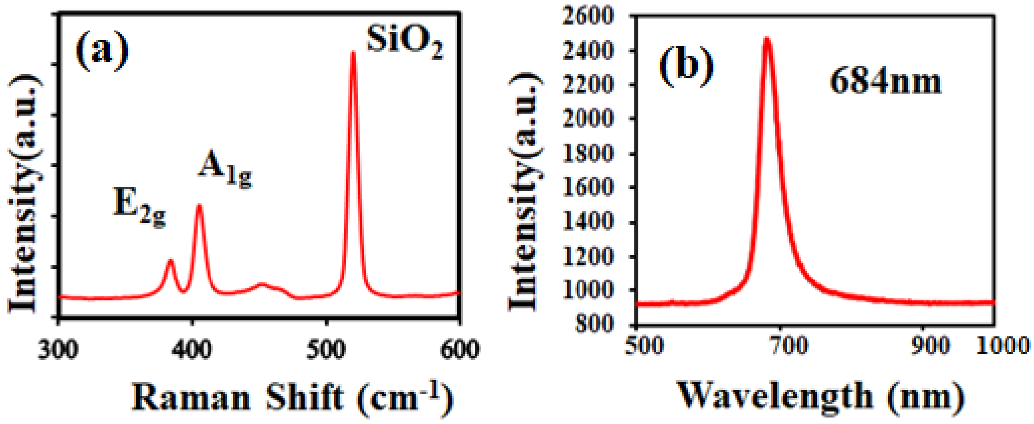

Figure 4-4 (a) Raman spectra with characteristic in-plane Mo-S vibrational mode E^{1}_{2g} (383.5 cm^{-1}) and out of plan vibration mode A_{1g} (404.5) of S atoms and (b) PL spectra with the peak position at 684 nm, corresponding to 1.81 eV

Figure 4-4-Figure 4-3b shows a typical PL spectrum of the as-synthesized MoS_2 layer, displaying a sharp peak with its center at 684 nm (which is equivalent to 1.81 eV) with a Full width at half maximum (FWHM) of 41nm, indicating characteristic of high optical quality CVD grown MoS_2 [40]. The intensity of the peak, position and FWHM for a monolayer MoS_2 are similar with previously reported values [41], [42].

The Ge/MoS_2 heterostructure was further studied with XPS analysis enabling to ascertain the chemical structures. Figure 4-5a shows survey spectrum for as-synthesized MoS_2 and Ge/MoS_2 heterostructure. Along with Ge and MoS_2 related peaks, C and O peaks were also observed for both samples, probable explanation for its appearance can be from the SiO_2/Si substrate or due to chemisorption. Figure 4-5-b shows XPS Mo3d spectra for the CVD synthesized MoS_2 layer prior to deposition of Ge film and after deposition of a Ge film. The Mo3d peak was detected from heterostructure surface, this is due to the ultrathin Ge film. The Mo3d doublet peaks for $3d_{5/2}$ and $3d_{3/2}$ for both Mo and S did not change after deposition of the Ge, indicating strongly the chemical and structural stability of the MoS_2 layers [43]. XPS spectra of sulfur for both as-synthesized and heterostructure is represented in Figure 4-5- c. Figure 4-5-d shows XPS spectra for deposited Ge film on MoS_2 layer. The peak-center at 30 eV corresponds to intrinsic Ge, with $3d_{5/2}$ and $3d_{3/2}$

chemical bonding states. However, a protuberance at higher binding energy (~32 eV) can be observed, this corresponding to chemisorption of oxygen by the Ge surface. From XPS analysis confirmed the formation of a thin heterostructure of the CVD synthesized MoS_2 layer and thermally deposited ultrathin Ge film.

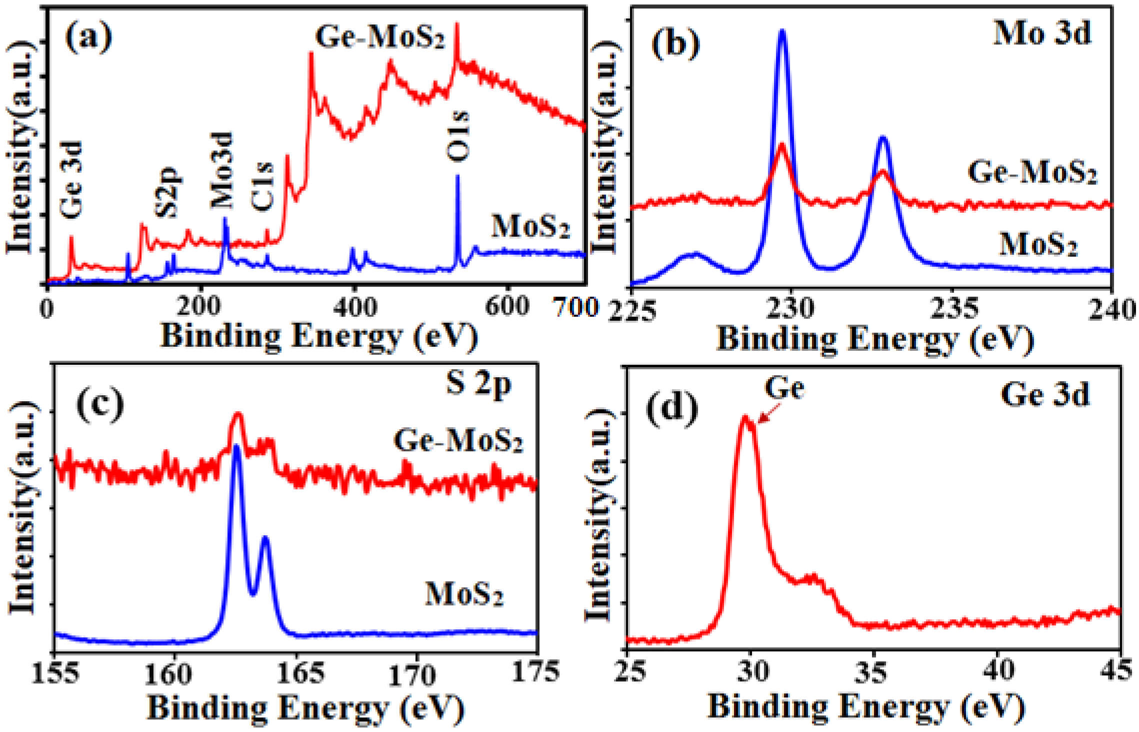

Figure 4-5 XPS (a) Survey spectra (b) Mo3d ($3d_{5/2}$ ~230 eV and $3d_{3/2}$ ~233 eV) (c) S2p ($2p_{3/2}$~162 eV $2p_{1/2}$~164 eV) for as-synthesized MoS_2 and Ge-MoS_2 heterostructure (d) Ge3d peak for Ge-MoS_2 heterostructure (Ge peak-center ~30 eV).

Raman study was performed at the interface of this heterostructure as shown in Figure 4-6a. Raman peaks were observed corresponding to MoS_2 layer and SiO_2/Si substrate with an additional peak attributing to the Ge-Ge bonding at around 300 cm^{-1}. Figure 4-6-b shows comparison between normalized Raman spectra for deposited Ge on SiO_2/Si and MoS_2 layer. For the both pristine Ge and Ge-MoS_2 heterostructure a sharp peak at 293.8 cm^{-1} can be seen.

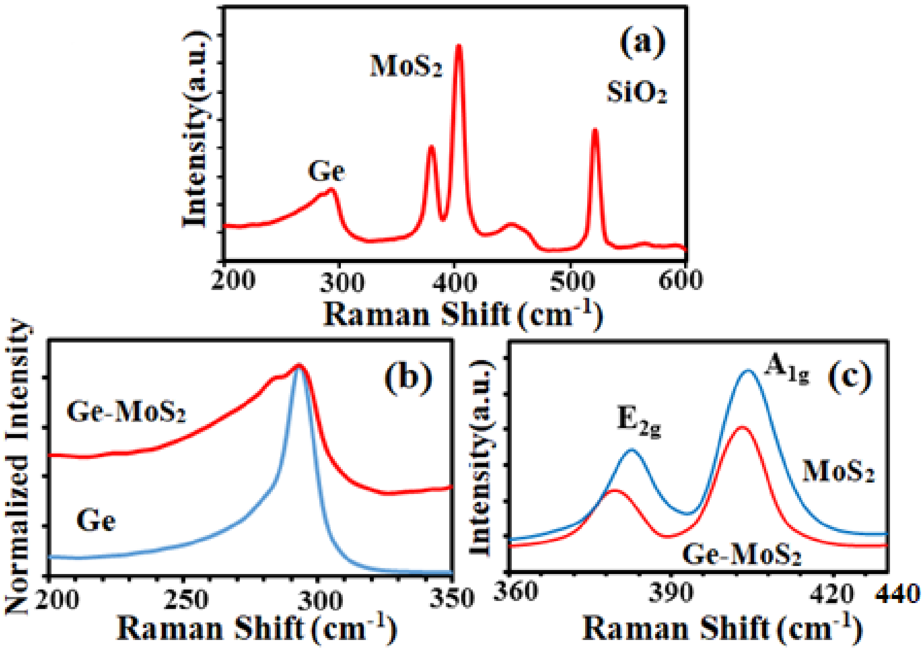

Figure 4-6 (a) Raman Spectra for Ge-MoS_2 heterostructure with peaks for Ge, MoS_2, and SiO_2/Si respectively (b) Normalized Raman spectra for Ge film with and without MoS_2 layer (c) Raman spectra of as-synthesized and Ge deposited MoS_2 layer.

A small shoulder-peak was seen for the Ge peak of Ge/MoS_2 heterostructure sample. Again, comparing the MoS_2 peaks for the as-synthesized and heterostructure sample (Figure 4-6c), I observed a blue shift for both E_{2g} (shift of 3 cm^{-1}) and A_{1g} peaks. Shift in Raman spectra occurs due to charge transfer interaction in the Ge-MoS_2 interface [37].

Charge transfer has been widely investigated and is an important phenomenon for heterostructures of the layered materials. Electron can transfer from n-type MoS_2 layer with higher electron density to the Ge layers causes blue shift in E_{2g} peak [44], [45].

Figure 4-7a shows a schematic of the fabricated Ge-MoS_2 heterostructure device with deposited metal electrodes. *J-V* characteristics of the fabricated Au/Ge/MoS_2/Al device

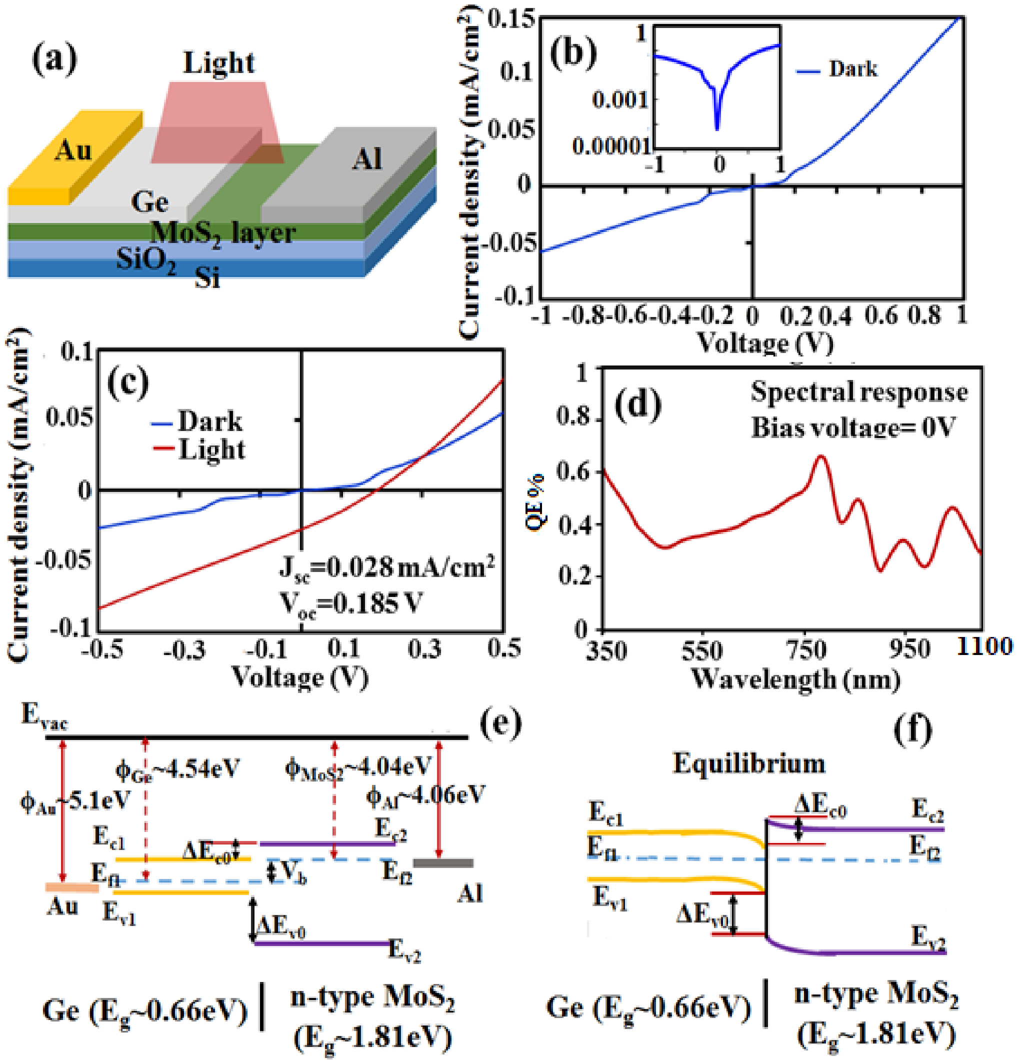

Figure 4-7 (a) Schematics of the fabricated Ge-MoS_2 heterostructure device (b) *J-V* characteristics without light illumination (inset shows log plot of *J-V*) (c) *J-V* characteristics without (blue) and with (red) light illumination showing a photovoltaic action (d) QE spectra for the heterostructure device. Energy band-diagram (e) with work function of active and electrode layers (f) equilibrium for the Ge-MoS_2 heterojunction.

was studied to confirm formation of a heterostructure diode. The *J-V* characteristic (without the light illumination) of the fabricated device is shown in Figure 4-7b (Inset shows log plot). Figure 4-7c shows *J-V* characteristics device under dark or in absence of illumination (blue) and under light illumination (red). A diode like rectification was observed for the Ge-MoS_2 ultrathin device. At present the device shows low rectification ratio (<10) with high leakage current. The shunt resistance also seems to be low from the *J-V* curve. The low shunt resistance may be endorsed to imperfectly optimized steps for the active layer deposition and metallization process. Hence, the fabrication of Ge-MoS_2 heterojunction structure as well as the metal electrodes plays an important role and needs to be investigated to fabricate superior device performance. Subsequently, photoresponsivity and a photovoltaic action were observed with the illumination of light. The heterojunction device showed a photovoltaic action with open circuit voltage (V_{oc}) of 0.185 V and short circuit current density (J_{sc}) of 0.028 mA/cm^2 as shown in Figure 4-7c. The low J_{sc} can be attributed to several factors, such as un-optimized layer thickness, non-ideal device characteristics, influence of contact electrodes and semi-transparent Au electrode. Figure 4-7d shows the QE for the fabricated device at zero bias voltage. The photoresponsivity was obtained for a broad wavelength (350~1100 nm) owing to the narrow band gap of the Ge. Interestingly, saturation of the QE was not observed at a higher wavelength (~1100 nm), indicating the possibility for further high wavelength (>1100 nm) application. The device *J-V* characteristic was measured once after 2-3 days and later at one-week intervals in atmospheric conditions. The photovoltaic action was distinct in every measurement with slight deviation in short circuit current. After one week there was no significant degradation in device characteristics. The photovoltaic action and photoresponse are consistent for all the fabricated devices (four different devices were fabricated), however the V_{oc} and J_{sc} can be affected by the active layer (Ge-MoS_2) thickness and metal electrodes. The broadband photosensitivity and a photovoltaic action can be explained with its efficient carrier dissociation and separation at the ultrathin Ge and MoS_2 layer heterojunction interface. Figure 4-7e shows an energy band diagram for the Ge and MoS_2 layers included are the work function of metal electrodes. Again, the interfacial charge transfer at the Ge-MoS_2 heterojunction can be significant to create a suitable build-in-field as observed from spectroscopic analysis [37]. The built-in voltage for the Ge-MoS_2 heterojunction was calculated from work function of MoS_2 and Ge under vacuum ($V_b=\phi_{Ge}-\phi_{MoS2}$), which was found to be 0.44eV.

Figure 4-7f shows the energy band diagram of the Ge-MoS_2 heterojunction under equilibrium. The charge transfer and carrier diffusion at the interface would lead to formation of a depletion layer, due to which efficient exciton dissociation can occur with the build-in-field. The electron and hole transport to the respective electrodes with exciton dissociation at the interface showed a photovoltaic action.

Further, the transient photoresponse characteristics of the Ge-MoS_2 heterojunction device in UV, visible and near-IR light at different bias voltage were investigated. Figure 4-7a-b shows the transient photoresponse at 0, -0.5 and -1.0 V for the device as summarized in table 1. Similarly, Figure 4-7c-d shows the transient photoresponse at 0, -0.5 and -1.0 V for illumination of white light (550 nm). The photoresponse at zero bias is 16.66 mA/W which increases to 164.5 mA/W at a reverse bias voltage of -1.0 V. The photoresponsivity increases with an applied bias voltage, then that of the photovoltaic mode. Figure 4-7e-f shows the transient photoresponse at 0, -0.5 and -1.0 V for illumination of near-IR light (1000 nm).

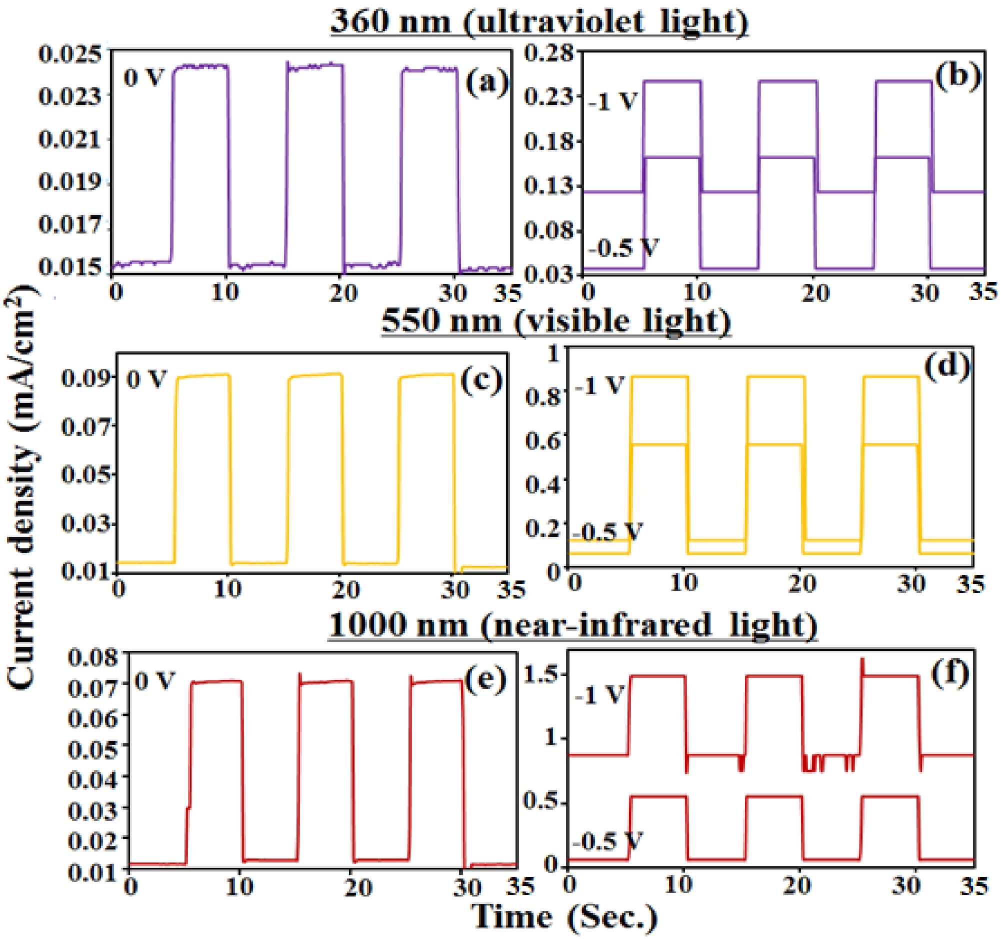

Figure 4-8 Transient photoresponse at (a) 0 bias voltage and (b) at -0.5 and -1 bias voltage under illumination of 360 nm light. (c) Transient photoresponse at 0 bias voltage and (d) at -0.5 and -1 bias voltage under illumination of 550 nm light. (e) Transient photoresponse at 0 bias voltage and (f) at -0.5 and -1 bias voltage under illumination of 1000 nm light.

The photoresponse at zero bias (photovoltaic mode) is 16.3 mA/W which increases to 168.5 mA/W at a reverse bias voltage of -1.0 V. It can be observed that the photoresponsivity is higher for visible and near-IR wavelength, due to better absorption of light in visible to near-IR wavelength and less recombination loss. The obtained results suggest that the developed Ge-MoS_2 devices can be significant for broadband photoresponsive devices.

Table 4-1**:** Photoresponse values of the Ge-MoS_2 heterojunction device at different applied voltage for UV, visible and near-IR lights.

Voltage (V)	***Photoresponse (mA/W)***		
	360 nm	*550 nm*	*1000 nm*
0	3.6	16.66	16.3
-0.5	49.6	107.5	133.2
-1.0	52	164.5	168.5

The device performance is comparable to other graphene and TMDCs based photodetectors and there is significant scope to further enhance the device performance [24]-[27], [35], [36]. The MoS_2 and Ge ultrathin heterostructure with broadband photoresponsivity provides an opportunity to develop next generation self-powered photodetectors for communication and other various applications.

4.5 Conclusion

In conclusion, in this chapter, the fabrication of a Ge/MoS_2 heterostructure and observed photoresponsivity for wide wavelength range (350-1100 nm) with a photovoltaic action is demonstrated. Formation of a thin interface with thermally evaporated Ge film on MoS_2 layers was confirmed by Raman and XPS studies. XPS analysis also confirmed intrinsic Ge chemical state, where MoS_2 layers remains unaffected. Raman study showed a blue shift of MoS_2 peaks for the heterostructure, indicating a charge transfer interaction between Ge and MoS_2. The fabricated heterojunction showed diode like rectifying *J-V* characteristics under dark and light illumination conditions. Photovoltaic action with V_{oc} and J_{sc} of 0.185 mV and 0.028 mA/cm^2, respectively was observed signifying the possibility of application as a broadband self-powered photodetector. The photoresponsivity for UV (360 nm), visible (550 nm) and near-IR (1000 nm) was obtained as 3.6, 16.66 and 16.3 mA/W for photovoltaic mode. Higher photoresponsivity was obtained with increase in applied bias voltage, than that of the photovoltaic mode. The highly smooth atomic surface of MoS_2 layer created an ultrathin heterojunction with the thin Ge film for efficient charge dissociation and separation. The demonstrated ultrathin Ge-MoS_2 heterostructure device showed the possibility of developing photo-sensing devices for various applications. After studying the properties of Ge/MoS_2 broadband photoresponsive device, I tried the possibility of depositing CuI layer as a p-type wide bandgap semiconductor, which can be suitable for the counterpart n-type MoS_2 for heterojunction device.

4.6 References

[1] T. F. Young Joon Hong, “Controlled van der Waals Heteroepitaxy of InAs Nanowires on Carbon Honeycomb Lattices,” *ACS Nano*, vol. 5, no. 9, pp. 7576–7584, 2011.

[2] D. Ruzmetov *et al.*, “Vertical 2D/3D Semiconductor Heterostructures Based on Epitaxial Molybdenum Disulfide and Gallium Nitride,” *ACS Nano*, vol. 10, no. 3, pp. 3580–3588, 2016.

[3] M. I. Bakti Utama *et al.*, “Recent developments and future directions in the growth of nanostructures by van der Waals epitaxy,” *Nanoscale*, vol. 5, no. 9, p. 3570, 2013.

[4] A. Yamada, K. P. Ho, T. Akaogi, T. Maruyama, and K. Akimoto, “Layered compound substrates for GaN growth,” *J. Cryst. Growth*, vol. 201, pp. 332–335, 1999.

[5] P. K. Mohseni *et al.*, “In_xGa_{1-x}as nanowire growth on graphene: Van der waals epitaxy induced phase segregation,” *Nano Lett.*, vol. 13, no. 3, pp. 1153–1161, 2013.

[6] S. Chuang *et al.*, “Near-ideal electrical properties of InAs/WSe_2 van der Waals heterojunction diodes,” *Appl. Phys. Lett.*, vol. 102, no. 24, p. 242101, 2013.

[7] E. Wisotzki, A. Klein, and W. Jaegermann, “Quasi van der Waals epitaxy of ZnSe on the layered chalcogenides InSe and GaSe,” *Thin Solid Films*, vol. 380, no. 1–2, pp. 263–265, 2000.

[8] P. K. Mohseni *et al.*, “Monolithic III-V nanowire solar cells on graphene via direct van der Waals epitaxy,” *Adv. Mater.*, vol. 26, no. 22, pp. 3755–3760, 2014.

[9] X. Duan *et al.*, “Lateral epitaxial growth of two-dimensional layered semiconductor heterojunctions,” *Nat. Nanotechnol.*, vol. 9, no. 12, pp. 1024–1030, 2014.

[10] G. Gao *et al.*, “Artificially stacked atomic layers: Toward new van der waals solids,” *Nano Lett.*, vol. 12, no. 7, pp. 3518–3525, 2012.

[11] H. Fang *et al.*, “Strong interlayer coupling in van der Waals heterostructures built

from single-layer chalcogenides," *Proc. Natl. Acad. Sci.*, vol. 111, no. 17, pp. 6198–6202, 2014.

[12] Y. Liang *et al.*, "Strongly bound excitons in gapless two-dimensional structures," *Phys. Rev. B - Condens. Matter Mater. Phys.*, vol. 90, no. 11, pp. 2–7, 2014.

[13] M. P. Levendorf *et al.*, "Graphene and boron nitride lateral heterostructures for atomically thin circuitry," *Nature*, vol. 488, no. 7413, pp. 627–632, 2012.

[14] J. Dabrowski and H. J. Muessig, *Silicon Surfaces and Formation of Interfaces: Basic Science in the Industrial World*. Singapore: World Scientific Pub. Co., 2000.

[15] R. H. Kingston, "Review of germanium surface phenomena," *J. Appl. Phys.*, vol. 27, no. 2, pp. 101–114, 1956.

[16] L. Tang *et al.*, "Nanometre-scale germanium photodetector enhanced by a near-infrared dipole antenna," *Nat. Photonics*, vol. 2, no. 4, pp. 226–229, 2008.

[17] L. Cao, J. S. Park, P. Fan, B. Clemens, and M. L. Brongersma, "Resonant germanium nanoantenna photodetectors," *Nano Lett.*, vol. 10, no. 4, pp. 1229–1233, 2010.

[18] L. Colace *et al.*, "Metal-semiconductor-metal near-infrared light detector based on epitaxial Ge/Si," *Appl. Phys. Lett.*, vol. 72, no. 24, pp. 3175–3177, 1998.

[19] C. Yan, N. Singh, H. Cai, C. L. Gan, and P. S. Lee, "Network-enhanced photoresponse time of Ge nanowire photodetectors," *ACS Appl. Mater. Interfaces*, vol. 2, no. 7, pp. 1794–1797, 2010.

[20] L. Vivien *et al.*, "42 GHz pin Germanium photodetector integrated in a silicon-on-insulator waveguide," *Opt. Express*, vol. 17, no. 8, p. 6252, 2009.

[21] D. Feng *et al.*, "High-speed Ge photodetector monolithically integrated with large cross-section silicon-on-insulator waveguide," *Appl. Phys. Lett.*, vol. 95, no. 26, pp. 1–4, 2009.

[22] S. Sahni, X. Luo, J. Liu, Y. Xie, and E. Yablonovitch, "Junction field-effect-transistor-based germanium photodetector on silicon-on-insulator," *Opt. Lett.*, vol. 33, no. 10, p. 1138, 2008.

[23] F. Bai *et al.*, "A High-Performance Self-Powered Photodetector Based on Monolayer MoS_2 /Perovskite Heterostructures," *Adv. Mater. Interfaces*, vol. 5, no. 6, p. 1701275, Mar. 2018.

[24] S. Yang *et al.*, "Self-Driven Photodetector and Ambipolar Transistor in Atomically Thin GaTe-MoS_2 p–n vdW Heterostructure."

[25] L. Peng, L. Hu, and X. Fang, "Energy Harvesting for Nanostructured Self-Powered Photodetectors," *Adv. Funct. Mater.*, vol. 24, no. 18, pp. 2591–2610, May 2014.

[26] R. Cong *et al.*, "Ultrahigh, Ultrafast, and Self-Powered Visible-Near-Infrared

Optical Position-Sensitive Detector Based on a CVD-Prepared Vertically Standing Few-Layer MoS_2/Si Heterojunction," *Adv. Sci.*, vol. 5, no. 2, p. 1700502, Feb. 2018.

[27] X. Luo *et al.*, "Ultrasensitive flexible broadband photodetectors achieving pA scale dark current," *npj Flex. Electron.*, vol. 1, no. 1, p. 6, Dec. 2017.

[28] P. Vabbina *et al.*, "Highly Sensitive Wide Bandwidth Photodetector Based on Internal Photoemission in CVD Grown p-Type MoS_2/Graphene Schottky Junction," *ACS Appl. Mater. Interfaces*, vol. 7, no. 28, pp. 15206–15213, 2015.

[29] H. Coy Diaz, J. Avila, C. Chen, R. Addou, M. C. Asensio, and M. Batzill, "Direct observation of interlayer hybridization and dirac relativistic carriers in Graphene/MoS_2 van der waals heterostructures," *Nano Lett.*, vol. 15, no. 2, pp. 1135–1140, 2015.

[30] K. Roy *et al.*, "Graphene-MoS_2 hybrid structures for multifunctional photoresponsive memory devices," *Nat. Nanotechnol.*, vol. 8, no. 11, pp. 826–830, 2013.

[31] M. L. Tsai *et al.*, "Monolayer MoS_2 heterojunction solar cells," *ACS Nano*, vol. 8, no. 8, pp. 8317–8322, 2014.

[32] S. Khadka *et al.*, "As-grown two-dimensional MoS_2 based photodetectors with naturally formed contacts," *Appl. Phys. Lett.*, vol. 110, no. 26, 2017.

[33] L. Zhang *et al.*, "Structural and Electronic Properties of Germanene on MoS_2," *Phys. Rev. Lett.*, vol. 116, no. 25, pp. 1–6, 2016.

[34] X. Li, S. Wu, S. Zhou, and Z. Zhu, "Structural and electronic properties of germanene/MoS_2 monolayer and silicene/MoS_2 monolayer superlattices," *Nanoscale Res. Lett.*, vol. 9, no. 1, p. 110, 2014.

[35] F. Yang *et al.*, "Ultrathin Broadband Germanium–Graphene Hybrid Photodetector with High Performance," 2017.

[36] H. Tian *et al.*, "Novel field-effect schottky barrier transistors based on graphene-MoS_2 heterojunctions," *Sci. Rep.*, vol. 4, pp. 1–9, 2014.

[37] Y.-C. Lin *et al.*, "Charge transfer in crystalline germanium/monolayer MoS_2 heterostructures prepared by chemical vapor deposition," *Nanoscale*, vol. 8, no. 44, pp. 18675–18681, 2016.

[38] D. J. Trainer *et al.*, "Inter-Layer Coupling Induced Valence Band Edge Shift in Mono- to Few-Layer MoS_2," *Sci. Rep.*, vol. 7, no. August 2016, pp. 1–11, 2017.

[39] M. Thripuranthaka, R. V. Kashid, C. Sekhar Rout, and D. J. Late, "Temperature dependent Raman spectroscopy of chemically derived few layer MoS_2 and WS_2 nanosheets," *Appl. Phys. Lett.*, vol. 104, no. 8, 2014.

[40] B. Zhenga, and Y.Chen, “Controllable Growth of Monolayer MoS_2 and $MoSe_2$ Crystals Using Three-temperature-zone Furnace" *IOP Conf. Series: Materials Science and Engineering*, 274, p. 012085, 2017, doi; 10.1088/1757-899X/274/1/012085

[41] K. F. Mak, C. Lee, J. Hone, J. Shan, and T. F. Heinz, “Atomically thin MoS_2: A new direct-gap semiconductor,” *Phys. Rev. Lett.*, vol. 105, no. 13, p. 136805, 2010.

[42] S. M. Shinde *et al.*, “Stacking-controllable interlayer coupling and symmetric configuration of multilayered MoS_2,” *NPG Asia Mater.*, vol. 10, no. 2, p. e468, Feb. 2018.

[43] S. McDonnell, R. Addou, C. Buie, R. M. Wallace, and C. L. Hinkle, “Defect-Dominated Doping And Contact Resistance in MoS_2,” *ACS Nano*, vol. 8, no. 3, pp. 2880–2888, 2014.

[44] M.-H. Doan *et al.*, “Charge Transport in MoS_2/WSe_2 van der Waals Heterostructure with Tunable Inversion Layer,” 2017.

[45] M.-Y. Li *et al.*, “Epitaxial growth of a monolayer WSe_2-MoS_2 lateral p-n junction with an atomically sharp interface,” *Science (80-.).*, vol. 349, no. 6247, pp. 524–528, Jul. 2015.

CHAPTER 5

5. Observing charge transfer interaction in CuI and MoS_2 heterojunction for photoresponsive device application

5.1 Introduction

In this chapter, the investigation of CuI/MoS_2 heterostructure has been compiled. Contrary to previous chapter on Ge/MoS_2 heterojunction, the feasibility of a heterojunction device of MoS_2 layer with a high bandgap semiconductor was investigated. In this prospect, CuI was selected due to its p-type conductivity, whereas the counterpart MoS_2 layer is an n-type semiconductor. It is also relevant to keep in mind that γ-CuI is a layered structure materials that can be suitable for high quality heterostructure interface formation. Hence, formation of γ-CuI layer by two different methods 1) solid iodization process and 2) thermally evaporation process on CVD synthesized MoS_2 were explored. Previous studies have shown that TMDCs based layered materials can be used for fabrication of Schottky and p-n junctions showing ultrahigh photosensitivity for photodiodes and solar cell applications [1]–[8]. Integration of the TMDCs layers with 3D bulk semiconductor (such as silicon, gallium nitride, etc.) has been also explored to create a 2D/3D active heterojunction device [9]–[14]. The MoS_2-silicon heterojunction is the most explored system for fabrication of efficient photo-sensors and solar cells [12]–[14]. The 2D TMDCs can be readily integrated to fabricate a heterostructure without constrains of lattice matching due to the dangling bond free lattice and strong Van der Waals interaction. Another important aspect in such heterostructure is the ultrafast charge transfer interaction process at the interfaces, which enable to develop high photoresponsive and efficient optoelectronic devices [15].

The charge transfer interaction in two different TMDCs layered materials such as MoS_2-WSe_2 heterojunction has been investigated [16]. The stack of MoS_2 and WSe_2 monolayer forms a p-n junction, creating a built-in electric field across the interface thereby facilitating efficient electron-hole separation and transfer [15], [16]. The charge transfer interaction in TMDCs layered materials with wide band gap semiconductors has also significant importance considering the possibility of developing transparent van-der-Waals heterojunction devices. The integration of the TMDCs layered materials with gallium nitride and silicon carbide semiconductors has been investigated for optoelectronic device applications [13], [17]. However, most of the oxide and nitride based wide band gap semiconductors are normally n-type, where the counterpart TMDCs layers are normally p-type. The γ-copper iodide (γ-CuI) with p-type conductivity is one of the notable halide wide band gap (~3.1 eV) semiconductor with two dimensional layered structures and can be significant to integrate with n-type TMDCs layer semiconductors [18]–[21]. γ-CuI with excellent hole-transporting property have great prospect in high efficiency solar cells, photo-sensors and other device applications [21], [22]. The charge transfer interaction and formation of effective junction potential of p-type γ-CuI and n-type TMDCs layers are still to be explored for fabrication of efficient optoelectronic device components. In the prospect, I explore the possibility of fabricating CuI/MoS_2 based heterojunction and their interface properties for developing a photoresponsive device. Significant quenching of PL peak for the MoS_2 layer in CuI/MoS_2 heterostructure was observed attributing to the spontaneous separation of charge carriers at the interface. Significantly, excellent photoresponsivity was obtained for the CuI/MoS_2 heterojunction device with illumination of white light, signifying the possibility of application photodiode and solar cells. This can be attributed to the effective exciton dissociation and charge separation at the interface of layered γ-CuI (111) and MoS_2 heterostructures due to presence of a strong build in field. In what follows, we demonstrate the fabrication process of γ-CuI cubic crystal structure along the (111) plane on MoS_2 layers and their interface properties to develop a photoresponsive device.

5.2 Experimental details

5.2.1 CVD Synthesis of MoS_2 layer

MoS_2 layer was synthesized by CVD on SiO_2/Si and Al_2O_3 (sapphire) substrates and used for CuI layer deposition. Modified assembly of small inner tube was used in conjunction with regular quartz tube and with two furnace system. The substrates were cleaned using IPA and acetone each for 10 minutes with sonication to remove the surface impurities. Subsequently, the substrate was dried using argon gas flow to avoid atmospheric contamination. Sulfur was kept in one end of the inner small tube under LTF at 200 °C and MoO_3 powder was kept in ceramic boat covered (face-down) with cleaned SiO_2/Si substrate, at the other end of the small inner tube under HTF heated to 750 °C. In the optimized condition HTF was started first to attain the temperature of 600 °C, at this point the LTF heating was started. As the LTF reached 200 °C, the HTF also reached to evaporation temperature of 750 °C. It is observed that the evaporation of sulfur and MoO_3 powder need be synchronized to get uniform layer of MoS_2 on the target substrate. Growth time was kept at 40 minutes after which, first LTF was cooled down to avoid any secondary sulfur deposition on substrate surface and then HTF was cooled to room temperature.

Table 5-1 Experimental parameters of MoS_2 layers synthesis on the target substrates

Experiment	Amount of MoO_3 (mg)	Amount of Sulfur (mg)	Growth Temp. (°C)	Carrier Gas (sccm)	Growth time (min)	Growth Substrate
MoS_2	10	100	750	Ar : H_2 (97:3)	40	SiO_2/Si and Al_2O_3

5.2.2 CuI deposition on MoS_2 layers

Two different approaches were explored for the deposition of CuI on MoS_2 layers. In one approach, first Cu film was deposited on MoS_2 substrate using thermal evaporator. Subsequently, the Cu film on MoS_2 layer was treated with I vapor in atmospheric condition and room temperature in a sealed box as sown in Figure 5-1. In another approach, CuI powder (Wako Pure Chemical Industries Ltd. Purity-95%) was directly deposited using high vacuum thermal evaporator at a chamber pressure of $6x10^{-4}$ Pa.

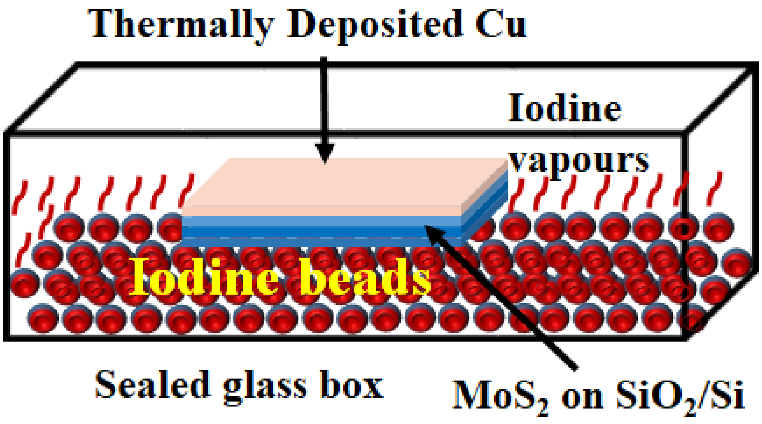

Figure 5-1 Solid phase reaction chamber for Cu film with I vapor on MoS_2 layer ($Cu/MoS_2/SiO_2/Si$). Vapor from I beads in the sealed box react with metallic Cu film at room temperature and pressure to form CuI.

5.2.3 Device fabrication process

The heterostructure fabricated using CVD synthesized MoS_2 on Al_2O_3 substrate was used for device fabrication to neglect any effect of silicon wafer. In one part of the masked MoS_2 layer, a CuI layer was thermally evaporated. The fabricated device structure is shown in Figure 5-9a. Gold (Au) and aluminum (Al) electrodes were deposited subsequently on CuI and MoS_2 respectively, using high vacuum thermal evaporator. The currents density-voltage (*J-V*) characteristic of the device was investigated using two probe systems at room temperature.

Table 5-2 Experimental parameters of Cu and CuI deposition on MoS_2 layers

Experiment	**Precursor Amount (mg)**	**Pressure (Pa)**	**Melting temp.(°C)**	**Current (amp)**	**Deposition time (min)**	**Growth Substrate**
Cu deposition	500	$7x10^{-4}$	1085	40	3	$MoS_2/SiO_2/Si$
CuI	1000	$7x10^{-4}$	606	40	2	$MoS_2/SiO_2/Si$ and Al_2O_3

5.2.4 Characterization of materials and devices

The synthesized materials were analyzed by SEM, Raman spectroscopy, AFM, XPS, UV-Vis absorption spectroscopy, XRD and PL analysis. XRD study of the samples were carried out by Rigaku RINT-2100. *J-V* characteristics of the CuI/MoS_2 heterojunction device were carried out at room temperature using a two-probe system and Keithley 2401 SourceMeter.

5.3 Results and discussion

5.3.1 SEM

SEM image in Figure 5-2a shows the triangular MoS_2 crystals, merging to form a continuous film. Figure 5-2b shows SEM image at the intersection of MoS_2 and CuI films. Formation of a continuous CuI film was obtained on the MoS_2 layers. The particles size is around 50-100 nm as determined from the SEM micrograph. The surface morphology of the CuI film on the deposition process, where, the solid phase iodization of Cu thin film showed much higher surface roughness. Figure 5-2c shows SEM image of the

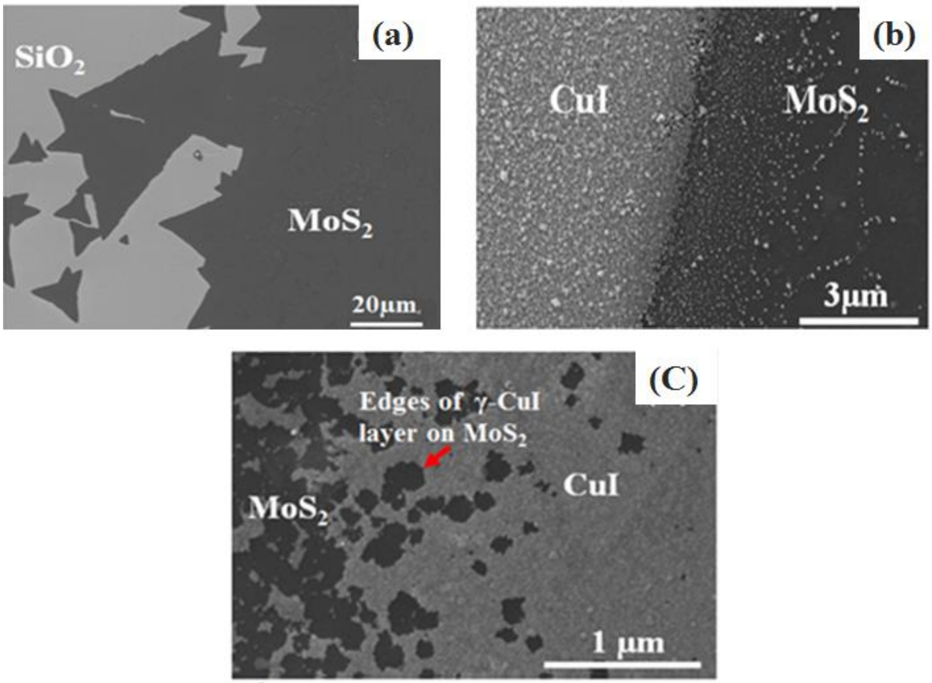

Figure 5-2(a) SEM image of triangular MoS_2 crystals, merging to form a continuous film.(b) SEM image at the intersection of MoS_2 layer and CuI film.(c)SEM image of the thermally evaporated CuI film on MoS_2.

deposited CuI film on MoS_2, presenting a different surface morphology compared to solid phase iodization process with relatively smoother surface. Interesting feature of hexagonal shape edge structures are visible from the SEM image, which is also main feature of MoS_2 and other layered materials.

5.3.2 AFM

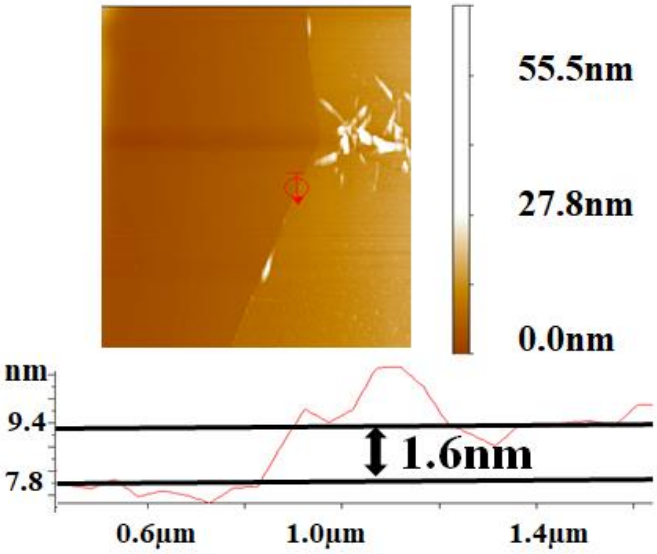

Figure 5-3 AFM image and thickness profile for the synthesized MoS_2 layers on SiO_2/Si substrate.

The number of MoS_2 layers can be confirmed by an AFM analysis. AFM image analysis of the synthesized MoS_2 on SiO_2/Si substrate as presented in Figure 5-3, the measured thickness i.e. 1.6 nm corresponds more than single layer MoS_2.

5.3.3 Raman spectroscopy

The number of MoS_2 layers can be confirmed by Raman analysis. Figure 5-4a Characteristic Raman frequencies for layered MoS_2 were observed at 385.6 cm^{-1} for E_{2g} and 406.6 cm^{-1} for A_{1g} respectively. The Raman spectra in Figure 5-4a shows the difference between E_{2g} and A_{1g} to be 21 cm^{-1}. Figure 5-4b shows the Raman spectra of the MoS_2 layers before and after the deposition of CuI film. A Raman spectrum of the heterostructure shows no change in peak position with that of as-synthesized MoS_2. This signifies the stain induced by the CuI film on the MoS_2 layers is not significant.

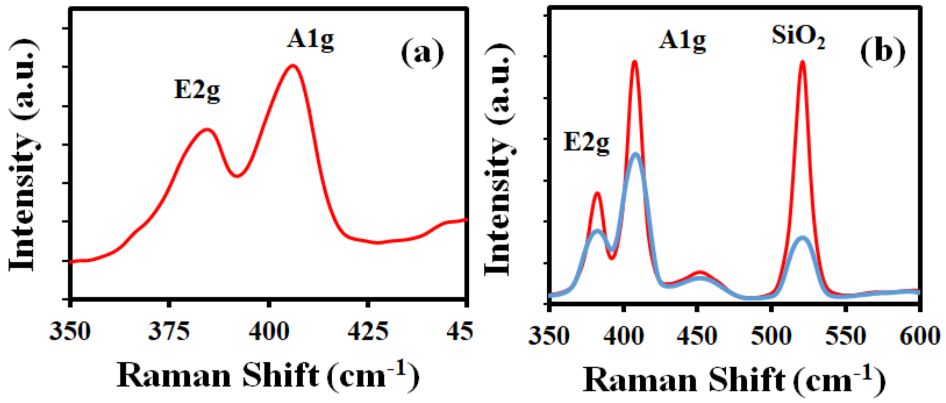

Figure 5-4(a) Raman spectra with frequencies for layered MoS_2 layers at 385.6 cm^{-1} for E_{2g} and 406.6 cm^{-1} for A_{1g} respectively (b) Raman spectra of the MoS_2 layers before and after the deposition of CuI film.

5.3.4 UV-Vis absorption spectroscopy

Figure 5-5a shows the UV-Vis absorption spectra for the CuI film on a glass substrate. It shows absorption in the ultraviolet wavelength with an absorption edge at 420 nm. In the inset of the Figure 5-5a shows the photograph of the metallic Cu film, confirming the complete change to a visible light transparent film after the iodization process. This confirmed the formation of truly visible light transparent CuI by iodization of deposited Cu film. The bandgap was calculated from the Tauc plot of the absorption spectra for the CuI film as shown in Figure 5-5b. The bandgap was found to be 3.0 eV for synthesized sample which is almost equal to theoretical value of 3.1 eV [18].

The UV-Vis spectra for directly deposited CuI on glass showed absorption in UV wavelength as shown in Figure 5-5c. Small bastion peak around 410 nm and sharp increase in absorption in the UV region is observed. Figure 5-5d shows a Tauc plot for the absorption spectra. Inset of Figure 5-5d shows the transparent CuI deposited on glass substrate. The optical bandgap of deposited CuI was found to be 2.98 eV as calculated from the Tauc plot. Small change in absorption spectra and optical band for the directly deposited film is observed due to difference in morphological and crystalline structure.

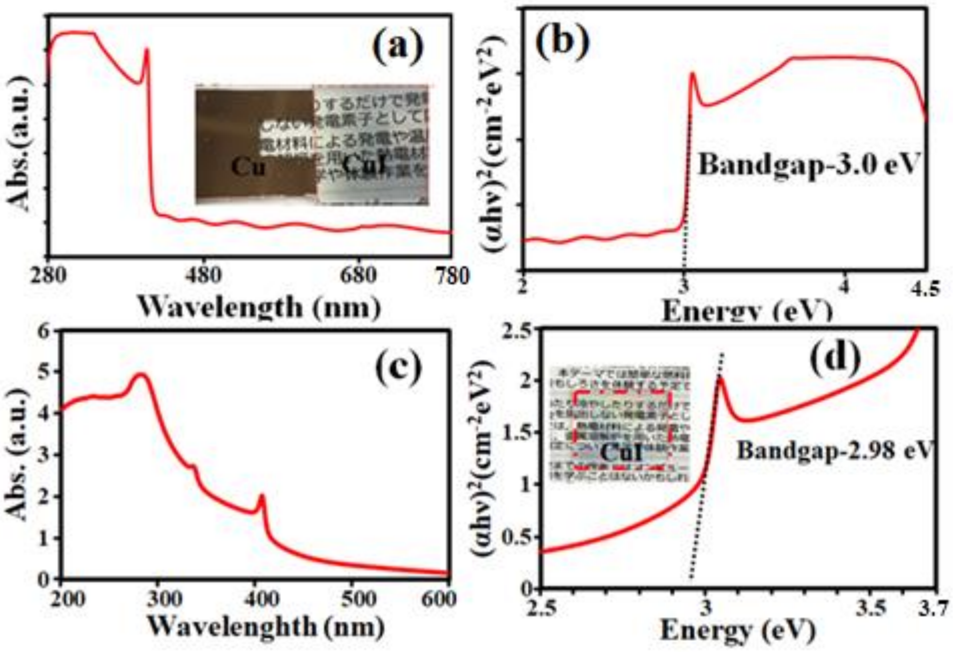

Figure 5-5 (a) UV-Vis absorption spectra for CuI on the glass substrate. (b) Touc plot confirming an optical band gap of 3.0 eV (c) UV-Vis absorption spectra for CuI on the glass substrate. (d) Tauc plot confirming an optical band gap of 2.98eV.

5.3.5 XRD

Figure 5-7a shows an XRD spectra of the CuI film synthesized by the solid phase iodization process. The solid iodination films have a preferential (220) plane and the (111) with sharp peaks, revealing the crystalline cubic structure of γ-CuI. Normally, CuI shows zinc blende cubic *structure* below 390 °C (γ-CuI*)* and a wurtzite structure (β-CuI) between 390 and 440 °C. Figure 5-7b shows the XRD diffraction pattern of thermally evaporated CuI film on glass substrate. The thermally evaporated CuI film shows more dominated peak for the (111) plane, in compare to the solid phase iodization process. Besides the sharp and intense peak at 26° for (111),small peaks were observed at 42.8°, 50.6° and 53°, corresponding to (220), (311), and (222) plane, respectively [19].

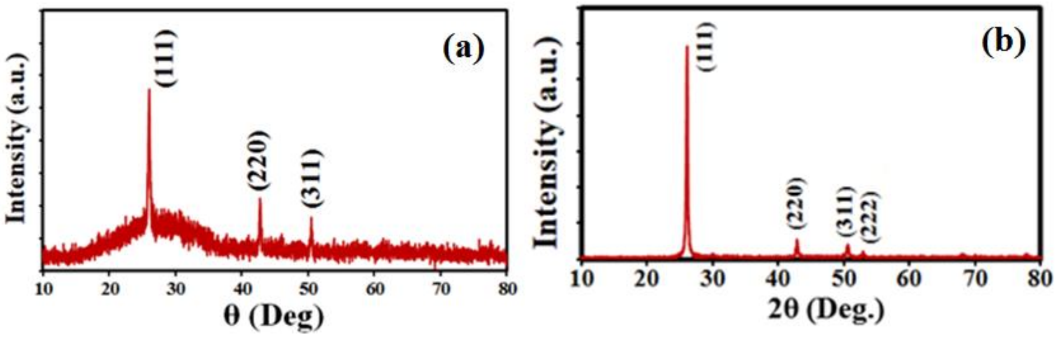

Figure 5-7 (a) X-Ray Diffraction (XRD) spectra of CuI film. (b) XRD diffraction pattern of thermally evaporated CuI film on glass substrate.

5.3.6 XPS

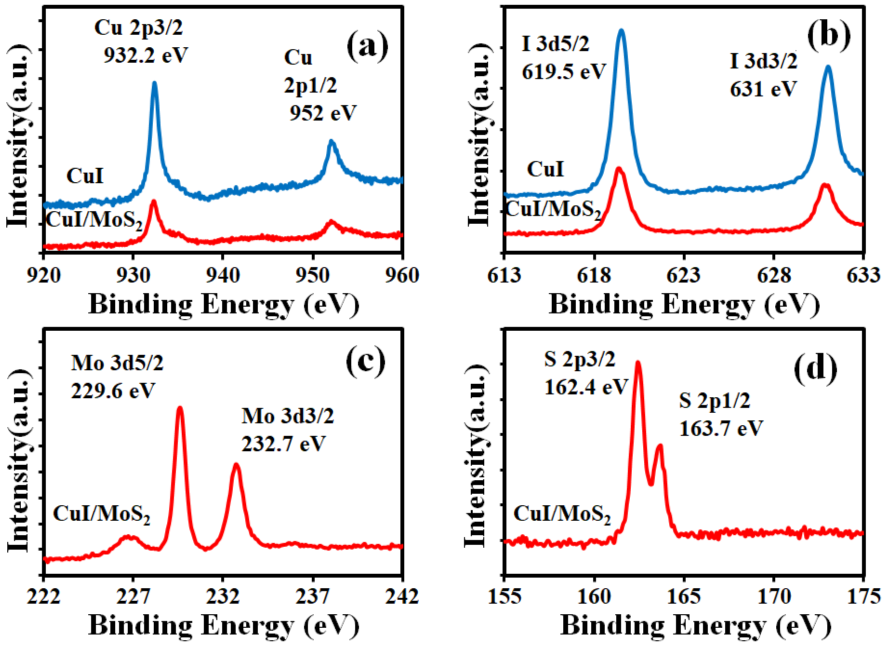

Figure 5-6 XPS spectra for (a) Cu(2p$^{3/2}$~932.2 eV and 2p$^{1/2}$~952 eV)(b) I(3d$^{5/2}$~619.5 eV and 631 eV for 3d$^{3/2}$) of the CuI film obtained by solid phase iodization process on glass and MoS_2 layers. XPS spectra for (c) Mo (Mo 3d$^{5/2}$~229.6 eV and 3d$^{3/2}$~323.7 eV) and (d) S (2p$^{3/2}$~162.4 eV and 2p$^{1/2}$~163.7 eV) of the MoS_2 layer.

The chemical composition and stability of synthesized heterostructure was analyzed by XPS characterization. Figure 5-6a-d shows the XPS spectra for Cu and I, respectively. The composition of CuI layer was investigated on carrying out the solid phase iodization process on glass and$MoS_2/SiO_2/Si$ substrates. Chemical analysis data confirms the stable heterostructure formation without shift in binding energy of either Cu or I. The XPS peaks for both CuI and CuI/MoS_2 was observed at 932.2 eV for $2p^{3/2}$ transition and 952 eV for $2p^{1/2}$ transition as well as 619.5 eV for $3d^{5/2}$ and 631 eV for $3d^{3/2}$ transition in Cu and I, respectively. Similarly, MoS_2 XPS peaks for Molybdenum (Mo) and Sulfur (S) were analyzed at the edge of the deposited CuI film. The $Mo3d^{5/2}$ and $Mo3d^{3/2}$ peaks were observed at 229.6 and 323.7 eV, respectively. The spectra for $S2p^{3/2}$ and $S2p^{1/2}$ corresponding to binding energies of 162.4 and 163.7 eV, respectively were observed. The overall chemical structure was found to be significantly stable with apparently no change in chemical structure of CuI as well as MoS_2. The chemical structure of MoS_2 was preserved even after CuI deposition, which in turn confirms the effectiveness of the process and heterostructure.

5.3.7 PL spectroscopy

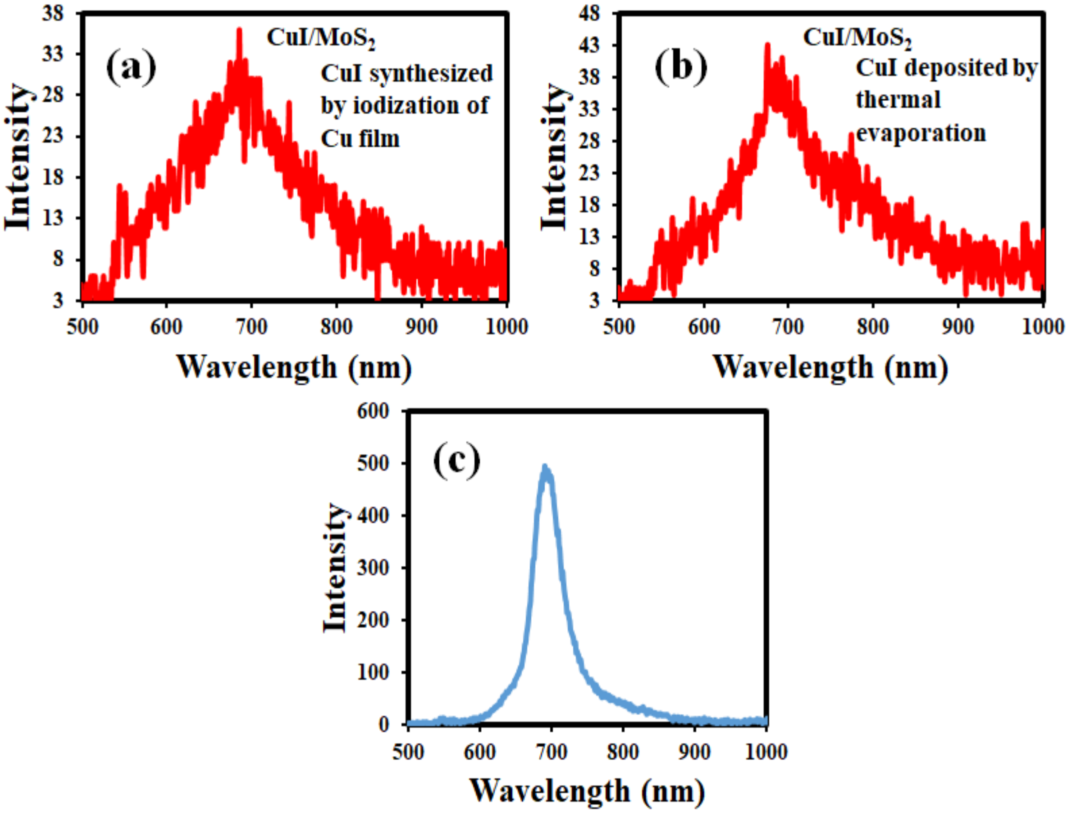

Figure 5-8 PL spectra of MoS_2 layers after the deposition of the CuI layer by the two different approaches (a) the solid phase iodization and (b) thermal evaporation. (c) PL peak for as synthesized MoS_2 layer.

Figure 5-8c shows a typical PL spectrum of the as-synthesized MoS_2 layer, exhibiting a sharp peak with peak-center at 684 nm (equivalent to 1.81 eV) and Full width at half maximum (FWHM) of 42 nm. This confirms the synthesis of good optical quality MoS_2 layer. This samples were further used for deposition of a Cu thin film by high-vacuum thermal evaporation process.

Figure 5-8a~b shows the PL spectra of MoS_2 layers after the deposition of the CuI layer by the two different approaches a) the solid phase iodization and b) thermal evaporation. The PL studies show apparent PL quenching for the CuI/MoS_2 heterostructure independent of the CuI deposition methods. The observed PL quenching effect in the heterostructure can be attributed to the spontaneous separation of charge carriers at the interface, suggesting the charge transfer interaction. Reduction of PL peak intensity is significant, which shows effective charge separation at the CuI/MoS_2 junction interface. This observation makes us think about the possible interaction of the two materials to fabricate efficient photoresponsive devices.

5.3.8 Fabrication and characterization of photoresponsive device

Figure 5-9a shows schematic diagram for fabricated heterojunction device with a device structure of Au/γ-CuI/MoS_2/Al. The device was fabricated with the thermally evaporated γ-CuI film, which shows highly (111) orientation crystalline structure. The device was characterized by *J-V* measurements under dark and light illumination. Figure 5-9b shows a *J-V* curve for an applied bias voltage range of -5V to +5V in dark condition. A non-linear *J-V* characteristics was observed, however a proper diode characteristics was not obtained due to large reverse saturation current. Further, *J-V* measurement was done under the illumination of white light (300-1100 nm) simulated radiation with intensity 100 mW/cm^2. A photocurrent was observed with light illumination as shown in Figure 5-9c. The current significantly enhanced in the forward and reverse direction with light illumination. From the *J-V* characteristic a photoresponsivity of 0.27 A/W is obtained at a bias voltage of 5V for the γ-CuI/MoS_2 heterojunction device. The photoresponsivity is equivalent or better than many of the commercial photodiodes. The excellent photoresponse in the device can be attributed to efficient exciton dissociation and separation at the γ-CuI/MoS_2 heterojunction interface. It should be also noted that the device was fabricated on an Al_2O_3 substrate, free from silicon wafer, attributing the

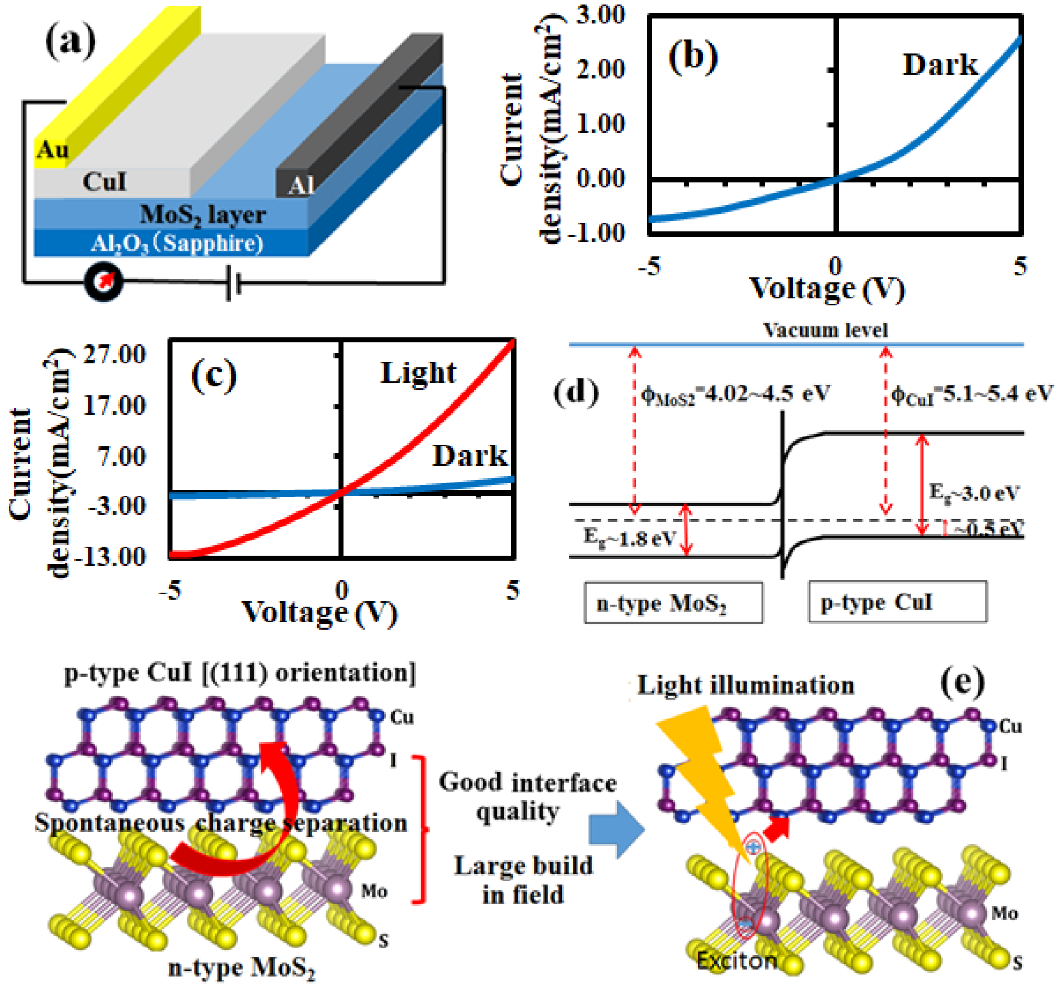

Figure 5-9 **(**a) schematic diagram for fabricated heterojunction device with a device structure of Au/γ-CuI/MoS$_2$/Al.(b) *J-V* characteristics under dark condition, (c) *J-V* characteristics under dark and white light illumination, presenting significant photoresponsivity. (d) Probable energy band diagram for the γ-CuI/MoS$_2$ heterojunction photovoltaic device. (e) Cross-section stick-and-ball crystal structures of cubic γ-CuI along (111) plane on MoS$_2$ layers, γ-CuI (111) enables formation of effective heterojunction interface for exciton dissociation and separation.

possibility of device fabrication on various substrates. Figure 5-9d shows the energy band diagram for the heterostructure at equilibrium condition. The band gap of the MoS$_2$ and CuI is considered as measured by the PL and optical absorption studies, respectively. Considering the previous reports, the work function of MoS$_2$ layer can be around 4.02~4.5eV, whereas for CuI it is around 5.1~5.4eV, attributing to presence of a large build in field (V_{bi}) of around 0.6~1.08eV [22], [23].

Effective exciton dissociation and charge transfer can occur in a γ-CuI/MoS_2 heterojunction interface, considering the large build in potential. Figure 5-9e shows the schematic for atomic model and charge transfer interaction in the γ-CuI/MoS_2 heterojunction interface. It is found that the thermally evaporated γ-CuI layer is preferably oriented along (111), thus formation of a cubic crystal structure of γ-CuI along the (111) plane on the MoS_2 layers is obtained. It will enable formation of much better interface between the two layered materials and as a result good photoresponsive characteristic is observed. Our find shows that the γ-CuI along (111) plane on MoS_2 layers forms excellent heterojunction interface for an atomic layer based photo-responsive device.

5.4 Conclusions

In conclusion, I have demonstrated the charge transfer interaction for the wide band gap CuI and CVD synthesized MoS_2 layers forming a photoresponsive heterojunction. CuI film was deposited on MoS_2 layer by solid phase iodization and thermal evaporation processes for the heterojunction fabrication. The thermally evaporated CuI film shows a main diffraction peak for (111) plane, confirming the formation of γ-CuI cubic crystal structure along the (111) plane on the MoS_2 layers. PL quenching effect was observed for the γ-CuI/MoS_2 the heterostructure, which can be attributed to the spontaneous separation of charge carriers at the interface, suggesting the charge transfer interaction. A photoresponsivity of 0.27 A/W with illumination of white light was obtained at a bias voltage of 5V for the γ-CuI/MoS_2 heterojunction device. The excellent photoresponsivity in the fabricated heterojunction is due to formation of effective interface between the two layered structure materials for efficient exciton dissociation and charge separation. It is shows that the interface quality can be controlled and optimized with crystalline structure of γ-CuI on MoS_2 layers for fabrication of atomic layer heterostructure optoelectronic device components, such as solar cells, photodetectors and other optoelectronic devices.

5.5 References

[1] C. H. Lee *et al.*, "Atomically thin p-n junctions with van der Waals heterointerfaces," *Nat. Nanotechnol.*, vol. 9, no. 9, pp. 676–681, 2014.

[2] M. L. Tsai *et al.*, "Monolayer MoS_2 heterojunction solar cells," *ACS Nano*, vol. 8, no. 8, pp. 8317–8322, 2014.

[3] M. S. Choi *et al.*, "Lateral MoS $_2$ p–n Junction Formed by Chemical Doping for Use in High-Performance Optoelectronics," *ACS Nano*, vol. 8, no. 9, pp. 9332–9340, Sep. 2014.

[4] H.-M. Li *et al.*, "Ultimate thin vertical p–n junction composed of two-dimensional layered molybdenum disulfide," *Nat. Commun.*, vol. 6, no. 1, p. 6564, Dec. 2015.

[5] M. Farmanbar and G. Brocks, "Controlling the Schottky barrier at MoS_2 metal contacts by inserting a BN monolayer," Jan. 2015.

[6] N. Kaushik *et al.*, "Schottky barrier heights for Au and Pd contacts to MoS_2," *Appl. Phys. Lett.*, vol. 105, no. 11, p. 113505, Sep. 2014.

[7] O. Lopez-Sanchez, E. Alarcon Llado, V. Koman, A. Fontcuberta I Morral, A. Radenovic, and A. Kis, "Light generation and harvesting in a van der waals heterostructure," *ACS Nano*, vol. 8, no. 3, pp. 3042–3048, 2014.

[8] M. M. Furchi, A. Pospischil, F. Libisch, J. Burgdörfer, and T. Mueller, "Photovoltaic Effect in an Electrically Tunable van der Waals Heterojunction," *Nano Lett.*, vol. 14, no. 8, pp. 4785–4791, Aug. 2014.

[9] S. Qiao *et al.*, "A vertically layered MoS_2/Si heterojunction for an ultrahigh and ultrafast photoresponse photodetector," *J. Mater. Chem. C*, vol. 6, no. 13, pp. 3233–3239, Mar. 2018.

[10] L. Wang *et al.*, "MoS_2/Si Heterojunction with Vertically Standing Layered Structure for Ultrafast, High-Detectivity, Self-Driven Visible-Near Infrared Photodetectors," *Adv. Funct. Mater.*, vol. 25, no. 19, pp. 2910–2919, May 2015.

[11] S. Krishnamoorthy *et al.*, "High current density 2D/3D MoS_2/GaN Esaki tunnel diodes," *Appl. Phys. Lett.*, vol. 109, no. 18, p. 183505, Oct. 2016.

[12] K. Zhang *et al.*, "Large scale 2D/3D hybrids based on gallium nitride and transition metal dichalcogenides," *Nanoscale*, vol. 10, no. 1, pp. 336–341, Dec. 2018.

[13] D. Ruzmetov *et al.*, "Van der Waals interfaces in epitaxial vertical metal/2D/3D semiconductor heterojunctions of monolayer MoS_2 and GaN," *2D Mater.*, vol. 5, no. 4, p. 045016, Aug. 2018.

[14] Y. Zhang *et al.*, "In Situ Fabrication of Vertical Multilayered MoS_2/Si Homotype Heterojunction for High-Speed Visible-Near-Infrared Photodetectors," *Small*, vol. 12, no. 8, pp. 1062–1071, Feb. 2016.

[15] R. Cheng *et al.*, "Electroluminescence and photocurrent generation from atomically sharp WSe_2/MoS_2 heterojunction p-n diodes," *Nano Lett.*, vol. 14, no. 10, pp. 5590–5597, 2014.

[16] B. Peng *et al.*, "Ultrafast charge transfer in MoS_2/WSe_2 p–n Heterojunction," *2D Mater.*, vol. 3, no. 2, p. 025020, May 2016.

[17] X. Guo, X. Tong, Y. Wang, C. Chen, G. Jin, and X.-Y. Guo, "High photoelectrocatalytic performance of a MoS_2–SiC hybrid structure for hydrogen evolution reaction," *J. Mater. Chem. A*, vol. 1, no. 15, p. 4657, Mar. 2013.

[18] N. Yamada, R. Ino, and Y. Ninomiya, "Truly Transparent p-Type γ-CuI Thin Films with High Hole Mobility," *Chem. Mater.*, vol. 28, no. 14, pp. 4971–4981, Jul. 2016.

[19] C. Yang, M. Kneiβ, M. Lorenz, and M. Grundmann, "Room-temperature synthesized copper iodide thin film as degenerate p-type transparent conductor with a boosted figure of merit.," *Proc. Natl. Acad. Sci. U. S. A.*, vol. 113, no. 46, pp. 12929–12933, Nov. 2016.

[20] N. Yamada, R. Ino, H. Tomura, Y. Kondo, and Y. Ninomiya, "High-Mobility Transparent p-Type CuI Semiconducting Layers Fabricated on Flexible Plastic Sheets: Toward Flexible Transparent Electronics," *Adv. Electron. Mater.*, vol. 3, no. 12, p. 1700298, Dec. 2017.

[21] W. Sun *et al.*, "Solution-Processed Copper Iodide as an Inexpensive and Effective Anode Buffer Layer for Polymer Solar Cells," *J. Phys. Chem. C*, vol. 118, no. 30, pp. 16806–16812, Jul. 2014.

[22] S. Yoon, H. Kim, E.-Y. Shin, Y.-Y. Noh, B. Park, and I. Hwang, "Thickness dependence of a CuI hole transport layer on initial photostability and photovoltaic performance of organic solar cells," *Phys. status solidi*, vol. 213, no. 9, pp. 2431–2437, Sep. 2016.

[23] S. Y. Lee *et al.*, "Large Work Function Modulation of Monolayer MoS_2 by Ambient Gases," *ACS Nano*, vol. 10, no. 6, pp. 6100–6107, Jun. 2016.

CHAPTER 6

6. Conclusions and future prospects

6.1 Conclusions

TMDCs such as MoS_2 and WS_2, have great attention due to their bandgap which are suitable for optoelectronics and nano-electronics applications. In this research work, high quality of MoS_2 crystals, ribbons, layers as well as WS_2 crystals were synthesized using modified APCVD technique. Various experimental parameters of the developed CVD process were optimized to synthesize MoS_2 and WS_2 layered structure.

Chapter 1 describes the **general introduction** of 2D-TMDCs in background of graphene and the characterization techniques used for the synthesized MoS_2 and WS_2 layers in brief.

In Chapter 2 the detailed method for **CVD synthesis** of unique ribbon structures with diffusion controlled growth process along with synthesis of crystals and continuous film has been explained. This chapter has been dedicated for characterization of these ribbons and their edge structure. This ribbons have catalytic and electrochemical application, whereas for optoelectronic device fabrication high PL crystals or films are utilized due to stability factor.

The degradation process of the TMDCs with long term atmospheric exposure **and the encapsulation** process has been compiled in **chapter 3**. The study provided the insight into the process of degradation and it has been revealed that crystallographic orientation is followed during the degradation. Also, effective encapsulation with Teflon as well as carbonaceous layer was proposed for protection from environmental degradation. Even after heating at high temperature, the encapsulation layer stayed intact and the structural integrity of the crystals was maintained. This study provided basis for possible fabrication of heterostructure device by depositing a foreign material on MoS_2. Thereby, exploiting the electronic properties of MoS_2 layer for heterostructure device by depositing a foreign semiconductor on top surface.

The application of MoS_2 for optoelectronics has been compiled in Chapter 4 and chapter 5. The heterostructure between MoS_2 and Ge was successfully fabricated and photovoltaic and photoresponsive devices was studied in detail. The layered structures were fabricated with relatively simple technique. This combination was particularly interesting for applications in self-powered photo detectors. Also, the p-n heterojunction between layered CuI and MoS_2 shows promising results. Significant photoresponse was observed under the illumination of white light. The overall effective heterostructures between the MoS_2 and other layered materials were realized in this thesis.

Chapter 6 summarizes the whole thesis and mention here as well as the future prospect of this study.

Above-mentioned new findings will open up a new door to the synthesis of the high quality 2D mono- and hetero-structured materials and were published in international journals that is enough worth for PhD thesis.

6.2 Future prospects

6.2.1 Prospective of CVD synthesis

In the view of mentioned synthesis methods in the thesis, it would be interesting to find the solution in terms of synthesizing of high edge density crystals or ribbons for catalytic applications. The ribbon synthesis process can be further explored to achieve very narrow ribbon structure in the order of nanometers. Although, the CVD growth on non-conducting surfaces such as quartz, sapphire and SiO_2/Si has already been achieved in this work, it would be stimulating to study the growth mechanism of MoS_2 and WS_2 on crystalline substrates such as gallium nitride (GaN), silicon (Si) as well as silicon carbide (SiC). The growth of MoS_2 layer on graphene, graphite and other carbon structures as well as boron and nitrogen containing materials (such as hexagonal boron nitride) also has great significance for catalytic, sensors and optoelectronic applications.

6.2.2 Prospective of degradation and edge reactivity

It will be very interesting to explore the edge reactivity of CVD synthesized chalcogenides, which can provide opportunity to fabricate highly sensitive sensors. The edge dependent catalytic reactivity is also great importance for energy storage devices, such as electrode materials for oxygen reduction reaction (ORR) and hydrogen evaluation reaction (HER). The degradation of monolayer TMDCs can be a beneficial rather than a hurdle to fabricate electronic devices. In modern day life, the semiconductor junk material is creating big environmental issues. Hence, the TMDCs layer can be seen as biodegradable semiconductor with outstanding electronic properties. It is expected that TMDCs can be critical materials with combination of other materials for wide range of applications.

6.2.2 Prospective of device fabrication

Here, I realized that photoresponsive devices can be fabricated by depositing a foreign semiconductor layer on the top of MoS_2 layer. In this concept, strain effect, metallization process and stability are main issues which needs to be studied in detail. Further, valley dependent electronic properties for formation of excitons and trions can be investigated using the propped layered heterostructures, which can be exciting prospects. Further, designing of TMDCs layer based biodegradable devices can be key aspect for future applications.

6.3 List of research achievements

(A) Publications in international journals

- Synthesis of MoS_2 ribbons and their branched structures by chemical vapor deposition in sulfur-enriched environment; **Rakesh D. Mahyavanshi**, Golap Kalita, Kamal P.Sharma, Masuharu Kondo, Takeshita Dewa, Toshio Kawahara, Masaki Tanemura ***Applied Surface Science,*** vol. 409, pp. 396-402 (July 2017) (Elsevier Journal I.F.=4.439)
- Encapsulation of transition metal dichalcogenides crystals with room temperature plasma deposited carbonaceous films; **Rakesh D. Mahyavanshi**, Golap Kalita, Rupesh Singh, Masaharu Kondo, Takehisa Dewa, Toshio Kawahara, Masayoshi Umeno, Masaki Tanemura, ***RSC Advances***, vol. 7, pp. 41136-41143, (August 2017) (Royal Society of Chemistry Journal I.F.=2.936)
- Photovoltaic Action With Broadband Photoresponsivity in Germanium- MoS_2 Ultrathin Heterojunction; **Rakesh D. Mahyavanshi**, Golap Kalita, Ajinkya Ranade, Pradeep Desai, Masaharu Kondo, Takehisa Dewa, Masaki Tanemura, ***IEEE Transactions on Electron Devices***, vol 65, issue 10, pp. 4434-4440 (August 2018) (IEEE Journal I.F.=2.62)
- Observing charge transfer interaction in CuI and MoS_2 heterojunction for photoresponsive device application; **Rakesh D. Mahyavanshi**, Ajinkya Ranade, Pradeep Desai, Masaki Tanemura, Golap Kalita, ***ACS Applied Electronic Materials***, November 2018 (Under review).

(B) Other publications

- Influence of oxygen on nitrogen-doped carbon nanofiber growth directly on nichrome foil Riteshkumar Vishwakarma, **Rakesh D Mahyavanshi,** Golap Kalita, Masaki Tanemura *et al*. ***Nanotechnology*** **27 (2016) 365602.**
- CuNi binary alloy catalyst for growth of nitrogen-doped graphene by low pressure chemical vapor deposition Remi Papon, **Rakesh D Mahyavanshi,** Golap Kalita, Masaki Tanemura *et al*. ***Phys. Status Solidi RRL*** **10, No. 10, 749–752 (2016).**
- Temperature dependent diode and photovoltaic characteristics of graphene-GaN heterojunction Golap Kalita**, Rakesh Mahyavanshi,** Masaki Tanemura *et al*. ***Appl. Phys. Lett.*** **111, 013504 (2017).**
- Influence of copper foil polycrystalline structure on graphene anisotropic etching Kamal P. Sharma, **Rakesh D. Mahyavanshi**, Golap Kalita, Masaki Tanemura ***Appl. Surf. Sci.*****, 393, 428-433(2017).**
- Photovoltaic action in graphene-Ga_2O_3 heterojunction with deep-ultraviolet irradiation Golap Kalita, **Rakesh D. Mahyavanshi,** Pradeep Desai, Ajinkya K. Ranade, Masaharu Kondo, Takehisa Dewa, Masaki Tanemura, ***Physica Status Solidi (RRL) – Rapid Research Letters*****, Volume 12, Issue 8 August 2018 1800198.**

(C) Conference presentation

- Synthesis of MoS_2 ribbons and their branched structures by chemical vapor deposition in sulfur enriched environment; **Rakesh D. Mahyavanshi**, Golap Kalita, Masaki Tanemura, The 64th JSAP Spring Meeting, 2017 March 14 – 17, 2017 Yokohama, Japan (Oral presentation).

- Synthesis of Monolayer Molybdenum Disulfide Ribbons in Sulfur Enriched Chemical Vapor Deposition Process; **Rakesh D. Mahyavanshi**, Golap Kalita, Masaki Tanemura, IUMRS-ICAM 2017, The 15th International Conference on Advanced Materials, August 27 - September 1, 2017, Kyoto University, Kyoto, Japan (Oral presentation).

- Formation of regular degradation patterns in chemical vapor deposited tungsten disulfide crystals under ambient condition; **Rakesh D. Mahyavanshi**, Golap kalita, Masaki Tanemura, The 78th JSAP Autumn Meeting, 2017 September 5 – 8, 2017 Fukuoka, Japan (Poster presentation).

- Fabrication of germanium-MoS_2 heterostructure for broadband photoresponsive device application; **Rakesh D. Mahyavanshi**, Golap kalita, Masaki Tanemura, The 79th JSAP Autumn Meeting, 2018 September 18 – 21, 2018 Nagoya, Japan (Oral presentation).

- Charge transfer interaction in CuI and 2D-MoS_2 layer p-n heterojunction; **Rakesh D. Mahyavanshi**, Golap kalita, Masaki Tanemura, 31st International Microprocesses and Nanotechnology Conference, 2018 November 13-16, 2018 Sapporo, Japan (Oral presentation).